

HARVARD UNIVERSITY
Graduate School of Arts and Sciences



DISSERTATION ACCEPTANCE CERTIFICATE

The undersigned, appointed by the

Harvard John A. Paulson School of Engineering and Applied Sciences
have examined a dissertation entitled:

“Mechanics of Biologically Inspired Structures and Flexible Mechanical Metamaterials”

presented by: Matheus C. Fernandes

Signature Katia Bertoldi
Typed name: Professor K. Bertoldi

Signature [Handwritten Signature]
Typed name: Professor J. Weaver

Signature Chris H. Rycroft
Typed name: Professor C. Rycroft

June 7, 2021

Mechanics of Biologically Inspired Structures and Flexible Mechanical Metamaterials

A DISSERTATION PRESENTED

BY

MATHEUS C. FERNANDES

TO

THE SCHOOL OF ENGINEERING AND APPLIED SCIENCES

IN PARTIAL FULFILLMENT OF THE REQUIREMENTS

FOR THE DEGREE OF

DOCTOR OF PHILOSOPHY

IN THE SUBJECT OF

APPLIED MATHEMATICS

HARVARD UNIVERSITY

CAMBRIDGE, MASSACHUSETTS

JUNE 2021

©2021 – MATHEUS C. FERNANDES
ALL RIGHTS RESERVED.

Mechanics of Biologically Inspired Structures and Flexible Mechanical Metamaterials

In this dissertation, I focus on exploring biologically inspired structures and the mechanics of flexible porous metamaterials by utilizing both experimental and computational methods.

For the biologically inspired structures portion of this dissertation, namely chapters 2 and 3, I focus on the architectural details of the glassy skeletal system from the hexactinellid sponge, *Euplectella aspergillum*. In chapter 2, I show that this sponge's meso-scale skeletal system, consisting of a square-grid-like lattice architecture overlaid with a double set of crossed diagonal bracings, exhibits the highest buckling resistance for a given amount of material when compared to related lattice structures. These findings are further confirmed through an evolutionary optimization algorithm, through which I demonstrate that the sponge-inspired lattice geometry occurs near the design space's optimum material distribution.

At another level of structural hierarchy, in chapter 3 I show that its complex maze-like organization of helical ridges that surround its main skeletal tube, not only provide additional mechanical reinforcement, but perhaps more significantly, deliver a critical hydrodynamic benefit by effectively suppressing von Kármán vortex shedding and reducing fluctuations in lift forcing over a wide range of biologically relevant flow regimes. By comparing the disordered sponge ridge geometry to other more symmetrical strake-based vortex suppression systems commonly employed in engineering contexts ranging from antennas to underwater gas and oil pipelines, I find that the unique maze-like ridge organization of the sponge can completely suppress vortex shedding rather

than delaying the shedding to a more downstream location. These findings highlight the sponge ridge design's potential benefit in engineering applications.

Lastly, in chapter 4, I utilize similar experimental and computational methods to study the response of porous mechanical metamaterials with well-defined periodicity for their ability to exhibit complex behavior as a result of their non-linear deformation. Although it is well known that buckling-induced planar transformations occur in 2D porous metamaterials, here I explore the emergence of 3D morphologies triggered by mechanical instabilities in an elastomeric block with tilted cylindrical holes. I demonstrate that the 3D deformation of these structures can be leveraged to tune surface properties including friction and light reflection, thus providing a new experimental platform for investigating deformation-dependent dynamics for tribological and optical applications.

Contents

1	INTRODUCTION	1
1.1	Biomimetics and Structural Engineering	2
1.2	Glass Sponges	5
1.3	Mechanical Metamaterials	8
1.4	Dissertation Structure and Overview	9
2	MECHANICALLY ROBUST LATTICES INSPIRED BY DEEP-SEA GLASS SPONGES	12
2.1	Abstract	13
2.2	Introduction	13
2.3	Design Considerations	15
2.4	Experimental and Numerical Results	16
2.5	Optimization Results	20
2.6	Discussion	21
2.7	Conclusion	23
3	MECHANICAL AND HYDRODYNAMIC ANALYSES OF HELICAL STRAKES IN THE SKELETONS OF GLASS SPONGES	27
3.1	Abstract	28
3.2	Introduction	28
3.3	Skeletal Geometry	30
3.4	Model Generation	33
3.5	Structural Analyses	38
3.6	Hydrodynamic analyses	43
3.7	Conclusion	52
4	SURFACE TEXTURE MODULATION VIA BUCKLING IN POROUS INCLINED MECHANICAL METAMATERIALS	54
4.1	Abstract	55
4.2	Introduction	55
5	ADDITIONAL WORK	71
5.1	Band Gaps in Acoustic Networks	72
5.2	Heart Valve	73
5.3	Tunable Materials	74
5.4	Brittle Star Arm Kinematics	75
5.5	Beetle Structural Color	76
5.6	Soft Membrane Design via Machine Learning	78
5.7	Soft Robot Sensor Using Machine Learning	79

6	CONCLUSIONS	80
6.1	Outlook	83
6.2	Personal Remarks	84
APPENDIX A SUPPLEMENTARY INFORMATION: MECHANICALLY ROBUST LATTICES INSPIRED BY DEEP-SEA GLASS SPONGES		85
A.1	Structure of the Hexactinellid sponge <i>Euplectella aspergillum</i>	86
A.2	Our four lattice designs	89
A.3	Experimental Setup	99
A.4	Finite Element (FE) Analysis	102
A.5	Optimization Analysis	118
APPENDIX B SUPPLEMENTARY INFORMATION: MECHANICAL AND HYDRODYNAMIC ANALYSES OF HELICAL STRAKES IN THE SKELETONS OF GLASS SPONGES		123
B.1	Porosity Definitions	124
B.2	Hydrodynamic CFD Model Details	126
B.3	Additional Information	134
APPENDIX C SUPPLEMENTARY INFORMATION: SURFACE TEXTURE MODULATION VIA BUCKLING IN POROUS INCLINED MECHANICAL METAMATERIALS		137
C.1	Geometry	138
C.2	Fabrication	140
C.3	Experiments	141
C.4	Numerical Simulations	146
C.5	Additional Results	149
REFERENCES		164
LIST OF PUBLICATIONS/PATENTS		165

Listing of figures

1.1	Microscope images of a burr seed, and a ‘velours and crochet’ (VELCRO ©). Inspired by the micro-structure of burr seeds as seen in (a) (Image Source) , velours and crochet technology use microscopic hooks and loops to attach two surfaces together as seen in (b) (Image Source) . ^[1]	2
1.2	Honeycomb structure and applications. (a) Shows picture of honeycomb created by worker bees out of beeswax (Image Source) . (b) Picture of a cross-section outer shell airplane wing (fuel tank removed) illustrating use of honeycomb as part of its structure (Image Source) . (c) Ceramic substrate illustrating the implementation of honeycomb structures (Image Source) (smaller image shows where substrate is placed within catalytic converter. (Image Source))	3
1.3	Structures of bones and trusses of cellular metals. (a) Hollow humerus bone from a Cape vulture’s (<i>Gyps coprotheres</i>) distal end. The structure is stiffened by V-shaped internal struts in a three-dimensional configuration (Image Source) . ^[1,2] (b) CAD image of the truss core structure. The multifunctional cellular metals have a structure similar to that of the bone of birds (Image Source) . ^[2,3]	4
1.4	<i>Euplectella aspergillum</i> skeletal structure. Photographic image of a cleaned sponge specimen showing the full skeletal structure along with a dried pair of shrimps (faded orange region in middle left region of sponge). A side note: when living, the sponge also contains a pair of live shrimps that often permanently inhabit the sponge once they grow too big to leave it. These occupants have earned the sponge the status of a symbol of eternal love in Japan, where it is typically given as a wedding present. ^[4,5]	5
1.5	Mechanical metamaterials. This figure shows a select few different types of mechanical metamaterials. (a) Shows a multi-stable mechanical metamaterial that has been partially compressed.(Image Source) (b) Shows a programmable mechanical metamaterial that is being actuated with hands.(Image Source) (c) Shows a select number of building blocks used to create origami-inspired metamaterials.(Image Source)	8
2.1	Representative skeletal system of the hexactinellid sponge <i>Euplectella aspergillum</i>. (a-c) Progressively magnified views of the sponge’s skeletal system. (d) Composite overlay of the idealized truss model (green and blue lines) and the sponge’s underlying skeletal structure. (e) Schematic of our sponge-inspired lattice with rectangular cross-section (<i>Design A</i>) comprising non-diagonal elements with length L and thickness $T_{A,nd}$ and diagonal elements with thickness $T_{A,d}$ located at a distance S from the nodes. Scale bars: (a) 4 cm; (b) 2 cm; (c) 2.5 mm.	14

2.2	Experimental and numerical results.	(a)-(d) Schematics of the different lattice geometries (<i>Design A-D</i>) considered in this study. (e) Mechanical deformation snapshots of the different 3D-printed models at 0% applied strain (top row) and 6% applied strain (bottom row). Scale bar: 3 cm. (f) Numerical (dashed lines) and experimental (solid lines) stress-strain curves for $n = 3$ independently tested samples of each design. Curves in this plot are color coded according to (a)-(d). All designs are characterized by the same total volume and mass ratio allocation between non-diagonals and diagonal elements.	17
2.3	Numerical results describing structural response to varying loading angle.	(a) Evolution of the structural stiffness for infinite size periodic lattice designs as a function of loading angle θ . (b) Critical buckling modes for <i>Design A-D</i> at $\theta = 0^\circ$. (c) Evolution of the effective buckling stress for the different lattice designs as a function of loading angle θ . Results are obtained by simulating a super-cell with 10 by 10 unit and periodic boundary conditions. (d) Evolution of the effective buckling stress as a function of the loading angle θ for finite (non-periodic) lattice structures comprising 10 by 10 unit cells. In each plot, the line color corresponds to the designs by color in (b). All designs are characterized by the same total volume and mass ratio allocation between non-diagonal and diagonal elements.	19
2.4	Optimization results and experimental validation.	(a) Optimal value of critical buckling load for varying number of diagonals. The color of each point represents the optimal mass ratio λ . (b) numerical (dashed lines) and experimental (solid lines) stress-strain curves for $n = 3$ independently tested samples of <i>Design A</i> and the optimal design. (c) Experimental snapshots of the optimal design at 0% applied strain (top figure) and 6% applied strain (bottom figure). Scale bar: 3 cm.	22
2.5	Numerical and experimental results of slender structures undergoing 3-point bending tests.	(a) Experimental snapshots of the four lattices comprising 11×2 square cells when loaded in 3-point bending at $\delta_{appl}/L = 0.45$. Scale bar: 3 cm. (b) Evolution of $n = 3$ experimentally obtained samples (continuous lines) and numerically (dashed lines) recorded reaction forces for the four designs as a function of the applied displacement.	25

3.1 Skeletal features of *Euplectella aspergillum*. (a) Photograph of a cleaned and dried siliceous skeleton of *E. aspergillum*, clearly depicting its tapered tubular form, its highly regular diagonally reinforced checkerboard-like square lattice structure, and its complex network of external ridges. (b) Unrolled ridge diagram illustrating the location of ridge elements in relation to the checkerboard-like lattice system. Filled squares denote the presence, and white squares denote the absence of ridge elements. Red squares denote clockwise ridge elements, blue squares denote counter-clockwise ridge elements, and purple squares denote corner elements (which do not count toward the number of either clockwise or counter-clockwise elements). (c) Bar plot showing the mean occupancy fraction for ridge elements (n=10 from figure B.7). Data presented are averages, and error bars represent +/- one standard deviation. The purple bar shows the total ridge occupancy fraction, which includes all clockwise (red bar), counter-clockwise (blue bar), and corner elements. (d) Plot adapted from Weaver et al.^[6], which illustrates that the combination of a decreasing volume per unit area for the underlying diagonally reinforced square lattice (orange) with an increasing ridge height (green) along the length of the tapered tube, results in a relatively consistent total material volume of silica per unit area throughout the entire skeletal system (black dotted line). For the orange and green data, the solid lines denote averages and the shaded regions denote +/- one standard deviation for n=10 specimens. 31

3.2 Workflow for the generation of sponge structural models. (a) Schematics showing the underlying diagonally reinforced square unit-cell geometry, which was tiled to produce the tubular lattice shown in (b). (c) Schematics showing the different ridge elements used to construct the complete skeletal model. Each component is color-coded in the left map, indicating its location. The dotted lines in each of the four 3D models correspond to the main ridge supporting elements, the brightly colored dots denote nodes of fusion between the struts, and the black arrows denote the direction of ridge elongation. To construct the complete ridge system for each tested sponge geometry (as shown in (d)), each of these four elements could be either translated, rotated, or mirrored (with the exception of the *Bidirectional* design which requires an additional crossing element). 33

3.3 Fully constructed skeletal models for structural and hydrodynamic analyses. Schematics showing (a) the baseline cylinder (containing no ridges), (b) the *Unidirectional* ridge design, (c) the *Bidirectional* ridge design, and (d) one representative example of the *Sponge* ridge design. For each ridge geometry, we also considered four variations of the inner tube (left to right): a solid (nonporous) tube, a low-porosity tube (matching the porosity of the living sponge), a high-porosity tube (matching the porosity of only the skeleton), and that of only the load-bearing skeletal elements of a sponge. CFD simulations were conducted on the first three tube geometries (solid, low-porosity, and high-porosity geometries) and FE simulations were conducted on the last geometry (load-bearing skeletal elements). 36

3.4	Hydrodynamic model generation workflow.	(a) Schematics showing one of the ten sponge ridge diagrams that provided a road map for the construction of a complete ridge network (b). The apex of the triangular ridges (blue) cross diagonally through the squares in (a) and their flat sides contact the underlying cylinder (gray) at the geometric centers (denoted by red dots) of the octagonal openings shown in figure 3.2(a). (c) Schematics showing a cross-sectional view of the non-porous cylindrical core (gray) with the labeled radius encompassing the ridge height R_r . (d) Schematics showing the cylinder thickness parameters, with R_o and R_i denoting the outer and inner radii, respectively. For (c) and (d), the vertical black dotted lines denote the model's neutral axis. (e) Schematics showing the complete non-porous baseline ridge geometry, which was generated from the map shown in (a). High (f) and low (g) magnification views, showing the geometries of the octagonal holes (red) for the small pores containing a side length of $S_o \approx 0.16L$, which approximates the porosity of a living sponge. High (h) and low (i) magnification views, showing the geometries of the octagonal holes (red) for the large pores containing a side length of $S_o \approx 0.4L$, which approximates the porosity of only the sponge's glassy skeletal system.	37
3.5	Structural Analysis.	(a) Schematics illustrating boundary conditions considered in the FE simulations. For all considered loading conditions, the displacement at the bottom was held fixed, namely $u_x = u_y = u_z = 0$, and a displacement δ_{appl} (indicated with arrows) was applied. (b)-(c) Bar plots showing normalized stiffness $RF/(\delta_{appl}LE_{mat})$ and normalized critical buckling force $F_{cr}/(L^2E_{mat})$ with different colors corresponding to each loading condition. The models considered were the ten mapped <i>Sponge</i> geometries (see figure B.7), the <i>Unidirectional</i> and <i>Bidirectional</i> geometries, the <i>Ridge-Free</i> design, and the <i>Reallocated Ridge Mass</i> design, from left to right respectively. For the the <i>Reallocated Ridge Mass</i> design, we employed the <i>Ridge-Free</i> design, but reallocated the volume from the ridges into the cylinder elements, thus making each element thicker and more robust.	40
3.6	Hydrodynamic results for non-porous cylindrical geometries.	(a) Plot showing transient lift coefficient C_l for the different non-porous geometries. (b) Magnified view of transient lift coefficients, showing the initial shedding behavior for different non-porous geometries. (c) Plot showing power spectral density (PSD) as a function of Strouhal number for different ridge-containing geometries. The vertical dashed black line shows the empirical Strouhal number for a smooth cylinder using a $Re = 5500$ flow regime. Note that the last 20 seconds of the transient data (when the flow reaches a periodic state) were used to compute the PSD. (d) Plot showing transient drag coefficient C_d for the different ridge-containing geometries. The horizontal black dashed line corresponds to empirical drag coefficient data for a smooth cylinder using $Re = 5500$ flow regime. (e) Vorticity fields illustrating shedding for the different non-porous geometries.	42
3.7	PSD for additional sponge geometries.	PSD plot comparing the different considered structures to additional sponge ridge designs obtained from real sponge samples (see figure B.7). Results are presented for $Re = 5,500$	43

3.8	Hydrodynamic results for cylindrical geometries exhibiting biologically relevant (small) porosities inspired by the anatomy of living specimens.	(a) Plot showing transient lift coefficient C_l for the different porous geometries. (b) Magnified view of transient lift coefficients, showing the initial shedding behavior for different non-porous geometries. (c) Plot showing power spectral density (PSD) as a function of Strouhal number for different ridge-containing geometries. Note that the last 20 seconds of the transient data (when the flow reaches a periodic state) were used to compute the PSD. (d) Plot showing transient drag coefficient C_d for the different ridge-containing geometries. (e) Vorticity fields illustrating shedding for the different different non-porous geometries.	44
3.9	Hydrodynamics results for $Re = 15,000$ and $Re = 60,000$ low-porosity cylinder baseline and sponge.	(a) Plot showing transient lift coefficient C_l as a function of time at $Re = 15,000$. (b) PSD plot showing density with frequency converted to Strouhal number. Note that the last 10 seconds of the transient data were used to compute the PSD at $Re = 15,000$. (c) Plot showing transient drag coefficient C_d as a function of time at $Re = 15,000$. (d) Plot showing transient lift coefficient C_l as a function of time at $Re = 60,000$. (e) PSD plot showing density with frequency converted to Strouhal number at $Re = 60,000$. Note that the last 5 seconds of the transient data were used to compute the PSD. (f) Plot showing transient drag coefficient C_d as a function of time at $Re = 60,000$	45
3.10	Hydrodynamic results for cylindrical geometries exhibiting biologically relevant (large) porosities reflecting the skeletal anatomy of specimens.	(a) Plot showing transient lift coefficient C_l for the different porous geometries. (b) Magnified view of transient lift coefficients, showing the initial shedding behavior for different non-porous geometries. (c) Plot showing power spectral density (PSD) as a function of Strouhal number for different ridge-containing geometries. Note that the last 20 seconds of the transient data (when the flow reaches a periodic state) were used to compute the PSD. (d) Plot showing transient drag coefficient C_d for the different ridge-containing geometries. (e) Vorticity fields illustrating shedding for the different different non-porous geometries.	46
3.11	Quantification of flow rate through the different investigated geometries.	(a) Bar plot showing time-averaged flow rate through the wall of the low-porosity tubular structures for $Re = 5,500$. (b) Bar plot showing time-averaged flow rate through the wall of the high-porosity tubular structure for $Re = 5,500$. (c) Bar plot showing time-averaged flow rate through the wall of the low-porosity tubular structure for $Re = 15,000$. (d) Bar plot showing time-averaged flow rate through the wall of the low-porosity tubular structure for $Re = 60,000$	48
4.1	Conceptual visualization and buckling-induced geometric transformations in our inclined metamaterial.	(a) Shown in light green, this structure is derived from conceptually slicing a block (shown in gray), containing a square array of cylindrical holes, at an angle θ . (b)-(c) pre- and post-buckling photos of the metamaterial at (b) $\Delta V/V_0 = 0$ and at (c) $\Delta V/V_0 = -1$ configurations for samples with $\theta = 0^\circ$ (left) and $\theta = 45^\circ$ (right). Both top and side views are shown. Additional information on this figure can be found in Supplementary Video 1.	58

4.2	<p>Experimental characterization of out-of-plane metamaterial buckling. (a) Pressure-volume relationship for the four different θ's considered ($\theta=0^\circ, 15^\circ, 30^\circ, 45^\circ$). Each sample was tested independently three times and the results from each test are reported as separate lines. (b) Normalized out-of-plane deformation measurements of the samples, obtained from 3D surface scans. The inset specifies the four regions (denoted by white boxes) used for measuring δ. Additional information on this figure can be found in Supplementary Video 2.</p>	60
4.3	<p>Buckling-induced tunable light reflection. (a) Photograph of the experimental setup outlining the sample location, light source, and pattern collection screen. (b) Evolution of the measured directional reflectance R_Ω (normalized by $\max(R_\Omega)$) as a function of $\Delta V/V_0$ for samples with $\theta = 0^\circ$ and $\theta = 45^\circ$. (c) Snapshots obtained during the deflation process for the $\theta = 0^\circ$ (left column) and $\theta = 45^\circ$ (right column) samples at $\Delta V/V_0 = 0$ (top row) and $\Delta V/V_0 = -1$ (bottom row). (d) Ray tracing simulations showing the directionality of light reflection for $\theta = 0^\circ$ (left column) and $\theta = 45^\circ$ (right column) samples at $\Delta V/V_0 = 0$ (top row) and $\Delta V/V_0 = -1$ (bottom row). For reference, the initial periodic reflected light pattern is due to small surface depressions in the non-evacuated structure. Additional information on this figure can be found in Supplementary Video 3.</p>	62
4.4	<p>Frictional measurements for our inclined metamaterial. (a) Photographs showing the bottom surface at the $\Delta V/V_0 = 0$ (top row) and $\Delta V/V_0 = -1$ (bottom row) states of samples with (from left to right): (i) $\theta = 45^\circ$ and no acrylic features; (ii) $\theta = 45^\circ$ and acrylic spheres; (iii) $\theta = 0^\circ$ and acrylic spheres; (iv) $\theta = 45^\circ$ and acrylic plates. (b) Photographs qualitatively showing the effect of the buckling-induced morphology on the tilting angle for which the sample began to slide, ϕ_{cr}. (c) Coefficient of friction for the different samples as a function of $\Delta V/V_0$. See figures C.8 to C.10 for additional information and results. Additional information on this figure can be found in Supplementary Video 4.</p>	64
4.5	<p>Design elements and performance of our soft robotic crawler. (a) Photograph showing the bottom of the soft robotic crawler. (b) Displacement of the center of mass of the first module of the crawler, u, normalized by the initial length of the crawler, L_{robot}, (blue line) and source pressure, P_{source}, (magenta line) versus time during a cycle. The center of mass provides information on the average displacement of the first module of the robot, which is obtained by averaging the displacement of both edge points for each frame. (c) Experimental snapshots of our soft crawler at $t = (i) 0, (ii) 1.5, (iii) 9.5, (iv) 11$ and (v) 20 s. The distance traveled during one full motion cycle (between T_0 and T_1) is indicated by the locations of the two red dotted lines. Additional information on this figure can be found in Supplementary Video 5.</p>	67

4.6	Out-of-plane buckling behaviors for different hole patterns. Post-buckling finite element results for three hole arrangements with $\theta = 45^\circ$ at $\Delta V/V_0 = -1$. For the triangular, rhombitrihexagonal, and trihexagonal holes arrays (the undeformed geometry is shown in the insets), we illustrate the normalized out-of-plane displacement, u_z/R_h . (b) Normalized out-of-plane deformation measurements obtained from Finite Element simulations at $\Delta V/V_0 = -1$ for the triangular, rhombitrihexagonal, and trihexagonal geometries, and the square arrangement from figure 4.1. Additional information on this figure can be found in Supplementary Video 6.	70
A.1	Historical illustration (left) and modern photograph (right) illustrating the flexible and rigid growth stages that occur during skeletal maturation in several hexactinellid sponges in the genus <i>Euplectella</i> . Left image adapted from Schulze ^[7]	88
A.2	Unit cell for Design A. Schematics of the unit cell for <i>Design A</i> (the sponge-inspired lattice). On the left, we indicate the geometric parameters of this design considering a circular cross-section, while on the right, we show the geometric parameters of this design considering a rectangular cross-section.	90
A.3	Unit cell for Design B. Schematics of the unit cell for <i>Design B</i> (an alternating open and closed cell structure resembling the sponge and employing a single set of diagonal bracings). On the left we indicate the geometric parameters of this design considering a circular cross-section, while on the right we show the geometric parameters of this design considering a rectangular cross-section.	94
A.4	Unit cell for Design C. Schematics of the unit cell for <i>Design C</i> (all cells filled with diagonal bracings, as is typically found in infrastructure applications). On the left we indicate the geometric parameters of this design considering a circular cross-section, while on the right we show the geometric parameters of this design considering a rectangular cross-section.	96
A.5	Unit cell for Design D. Schematics of the unit cell for <i>Design D</i> (square lattice with no diagonal reinforcement). On the left we indicate the geometric parameters of this design considering a circular cross-section, while on the right we show the geometric parameters of this design considering a rectangular cross-section.	98
A.6	RVE used for the different designs. Schematics of the RVEs used for <i>Design A-D</i> . Periodic boundary conditions are applied on the nodes that intersect with the red dashed line.	104
A.7	Global versus local instabilities. In each contour plot, we report the critical strain as a function of θ and the size of the super cell. For each of the simulations, periodic boundary conditions are applied along the outer perimeter of the $M \times M$ structure. This plot conveys that for <i>Designs A-C</i> the prominent buckling mode is the local mode, whereas for <i>Design D</i> , the prominent mode is a global mode. Choosing a sufficiently large M allows <i>Design D</i> to converge to a finite value for each θ	105
A.8	Critical strain for Design D at three selected loading angles. As the number of minimum RVEs M considered increases, the value for the critical buckling strain asymptotically approaches a constant.	105

- A.9 Mechanical response for different loading conditions.** For all cases presented in this figure, we consider a structure with 11×2 cells (5.5 RVEs) and hinged boundary conditions applied to cells *with* diagonal reinforcements. (a) In this case, a point deflection δ is applied to the top center of the structure while the bottom outside corners have constrained deflections, but unconstrained rotation. The normalized reaction force is plotted as a function of the δ for the four considered designs. Moreover, on the right we show numerical snapshots of the four designs for $\delta/L = 0.45$. The colors in these pictures provide a measure of the normalized von Mises stress. (b) In this case a distributed load is applied across the top of the structure while the bottom outside corners have constrained displacements, but unconstrained rotation. The normalized total reaction force is plotted as a function of the deflection for the four considered designs. On the right we show numerical snapshots of the four designs for $\delta/L = 0.6$, where δ is the vertical deflection of the top mid-point from the undeformed configuration. The colors in these pictures provide a measure of the normalized von Mises stress. 108
- A.10 Mechanical response for different loading conditions.** For all cases presented in this figure, we consider a structure with 11×2 cells (5.5 RVEs) and hinged boundary conditions applied to cells *without* diagonal reinforcements. (a) In this case, a point deflection δ is applied to the top center of the structure while the bottom outside corners have constrained deflections, but unconstrained rotation. The normalized reaction force is plotted as a function of the δ for the four considered designs. Moreover, on the right we show numerical snapshots of the four designs for $\delta/L = 0.45$. The colors in these pictures provide a measure of the normalized von Mises stress. (b) In this case a distributed load is applied across the top of the structure while the bottom outside corners have constrained displacements, but unconstrained rotation. The normalized total reaction force is plotted as a function of the deflection for the four considered designs. On the right we show numerical snapshots of the four designs for $\delta/L = 0.6$, where δ is the vertical deflection of the top mid-point from the undeformed configuration. The colors in these pictures provide a measure of the normalized von Mises stress. 109
- A.11 Mechanical response for different loading conditions.** For all cases presented in this figure, we consider a long slender realization of each design consisting of 11×2 cells (5.5 RVEs). (a) In this case, a point deflection δ is applied to the bottom right of the structure while the left edge of the structure is fixed. The normalized total reaction force is plotted as a function of the deflection for the four considered designs. Moreover, on the right we show numerical snapshots of the four designs for $\delta/L = 1.9$. The colors in these pictures provide a measure of the normalized von Mises stress. (b) In this case a distributed load is applied across the top of the structure while the left edge of the structure is fixed. The normalized total reaction force is plotted as a function of the deflection for the four considered designs. On the right we show numerical snapshots of the four designs for $\delta/L = 2.3$, where δ is the vertical deflection of the top right edge-point from the undeformed configuration. The colors in these pictures provide a measure of the normalized von Mises stress. . 110

A.12 Mechanical response for different loading conditions.	For all cases presented in this figure, we consider a long slender realization of each design consisting of 11×2 cells (5.5 RVEs). (a) In this case a deflection δ is applied to the right edge of the structure while the left edge of the structure is fixed. The normalized total reaction force is plotted as a function of the applied deflection for the four considered designs. Moreover, on the right we show numerical snapshots of the four designs for $\delta/L = 0.4$. The colors in these pictures provide a measure of the normalized von Mises stress. (b) In this case a distributed load is applied across each level of the structure while the left edge of the structure is fixed. The normalized total reaction force is plotted as a function of the deflection for the four considered designs. On the right we show numerical snapshots of the four designs for $\delta/L = 0.22$, where δ is the horizontal deflection of the right mid-point from the undeformed configuration. The colors in these pictures provide a measure of the normalized von Mises stress.	111
A.13 Comparison between experimental and numerical results.	This figure shows experimental snapshots of the experimental specimens at an applied 8% compressive strain overlaid with a cutout of the representative deformation predicted by our FE analyses. The close agreement between the experiments and simulations suggests that the FE simulations are accurately capturing the physical deformation of the specimens.	112
A.14 Effect of diagonal spacing and mass ratio on the response of <i>Design A</i> with rectangular cross-section.	(a) Evolution of the critical strain as function of the spacing between diagonals. (b) Evolution of structural stiffness as a function of the mass ratio $\lambda = V_{nd}/V_d$. (c) Evolution of critical strain as a function of the mass ratio λ . For each of the plots, the gray dashed vertical line indicates the parameter of <i>Design A</i> . These results demonstrate that <i>Design A</i> , the sponge design, is very close to the optimal one, when considering each parameter individually. All designs are characterized by the same total volume.	112
A.15 Effect of diagonal spacing and mass ratio on the response of <i>Design A</i> with circular cross-section.	(a) Evolution of critical strain as function of the spacing between diagonals. (b) Evolution of structural stiffness as a function of the mass ratio $\lambda = V_{nd}/V_d$. (c) Evolution of critical strain as a function of the mass ratio λ . For each of the plots, the gray dashed vertical line indicates the parameter of <i>Design A</i> . These results demonstrate that the shape of the cross-section does not have a significant role, as these results are similar to those presented in figure A.14 for a lattice with rectangular cross-section. All designs are characterized by the same total volume.	113
A.16 Response of <i>Design A-D</i> with circular cross-section.	(a) Evolution of the structural stiffness as a function of loading angle θ for lattices of infinite size. (b) Evolution of the effective buckling stress for the different lattice designs as a function of loading angle θ . Results are obtained by simulating a super-cell with 10 by 10 units and periodic boundary conditions. (c) Numerically predicted stress-strain curves for the 4 considered lattices when compressed with $\theta = 0$. For all plots, the color of the line corresponds to the respective design color depicted on the bottom.	113

A.17 Critical modes of *Design A-D* at $\theta = 0^\circ$ and $\theta = 45^\circ$. These critical buckling modes were calculated using a 10 by 10 super-cell and the snapshots shown here are the center 2x2 cells of the full 10x10 model. *Designs A-B* in this figure exhibit a similar deformation pattern when loaded at 0° or 45° . However, for *Design C-D*, different buckling patterns are triggered when loaded at 0° and 45° 114

A.18 Modes of finite size structure comprised of 3x3 unit cells. This figure shows the critical buckling modes obtained for finite geometries for *Design A-D* loaded in uniaxial compression. The top row corresponds to a structure angled at 0° , as in the experiments. The second row corresponds to the same structure however rotated by 45° and cut to maintain the same size as the row above. Each column in this figure corresponds to a different design. For each of the geometries, a slightly thicker frame is constructed to localize most of deformation away from the edges of the structure. These results convey that the diagonally reinforced geometries are not susceptible to edge effects when using at least 3 unit cells, whereas the non-diagonally reinforced structure is more susceptible to edge effects. 114

A.19 Modes of finite size structure comprised of 10x10 unit cells. This figure shows the critical buckling modes obtained for finite geometries of *Design A-D* loaded in uniaxial compression. The top row corresponds to a structure angled at 0° , as considered in the experiments. The second row corresponds to the same structure however rotated by 45° and cut to maintain the same size as the row above. Each column in this figure corresponds to a different design. For each of the geometries, a slightly wider frame is constructed to minimize edge effects. 115

A.20 Effect of sample size on critical stress. Evolution of the effective buckling stress as a function of the loading angle θ for finite-size lattice structures comprising M by M unit cells, where M ranges from (a) 1 to (j) 10. The shaded parts in (a) - (j) represent the lowest six buckling modes range. All plots provide a clear indication on the superior performance of *Design A* when comparing to *Designs C-D*, when $M > 2$ 116

A.21 Effect of joint stiffness analysis on critical stress. To evaluate the influence of the joints on the effective buckling stress of *Designs A-D* we conduct FE analysis on a period unit cell with modified stiffness on elements near the joints. In particular, we set the material stiffness to E_{box} for the elements within a box of edge length $L_{box} = 0.02L$ (see inset schematic in (a)). (a) Evolution of the normalized effective critical stress for varying the joint stiffness ratio E_{box}/E . (b) Schematic of *Design A-D* unit cells with the location of the joints highlighted by red dots. 117

A.22 Stress Analysis. Numerical snapshots extracted from non-linear FE analysis (with first mode imposed imperfection) at an imposed strain $\varepsilon = 0.001$. (a) The color indicates the normalized von Mises stress σ_{vm} with the maximum value for each structure indicated above each figure. (b) The color indicates the normalized maximum principle stress σ_{mp} with the maximum value for each structure indicated above each figure. 117

A.23 Effect of disorder on critical stress. To evaluate the influence of disorder on the effective buckling stress of <i>Design A</i> , we conduct FE analysis on a period unit cell on which we vary the mass allocated between diagonals going in different directions. For all analysis presented, the total volume allocated between diagonals and non-diagonals remains constant, namely $\lambda = \sqrt{2}$. V_a/V_b defines the ratio between the volume allocated to the two families of diagonals (with $V_a + V_b = V_{nd}/\sqrt{2}$). (a) Evolution of the effective buckling stress as a function of V_a/V_b for $\theta = 0$. We find that for $0.25 < V_a/V_b < 0.75$ disorder has a minor effect on the effective buckling stress. (b) Schematics of selected unit cell with different diagonal volume allocations V_a/V_b	118
A.24 Effect of disorder on critical stress. To evaluate the influence of disorder on the effective buckling stress of <i>Design A</i> we conduct FE simulations on a periodic unit cell in which we vary the location and orientation of individual diagonals, while maintaining periodicity of the structure. For all analysis presented, the total volume of the diagonals remains constant and equal to $V_{nd}/\sqrt{2}$. (a) Schematic illustrating the spacing S_a and S_b , defining the position of each diagonal. (b) Schematics of unit cell with varying S_a and S_b (with $S_a, S_b \in [0, 2L]$). (c) Effective buckling stress for 2,500 unit cell simulations, in which we perturb the sponge strut spacings S_a and S_b using a Gaussian \mathcal{N} with mean $\mu = 0$, standard deviation $\sigma = 0.3$ and magnitude ψ , namely, $S_a/L = 1 - 1/(\sqrt{2} + 2) + \psi\mathcal{N}(0, 0.3)$ and $S_b/L = 1 + 1/(\sqrt{2} + 2) + \psi\mathcal{N}(0, 0.3)$. The red markers indicate the mean for each considered ψ containing $n = 50$ simulations per discrete value of ψ . We find that the applied perturbation does not alter the mean effective critical stress and that the variation of $\bar{\sigma}_{cr}$ is bounded between $0.6 \times 10^{-2}\mu$ and $1.0 \times 10^{-2}\mu$	118
A.25 Schematic. Schematics highlighting the geometric parameters considered in our optimization analysis.	120
A.26 Evolution of the objective function and design parameters during CMA-ES iterations. This figure shows the evolution of (a) the cost function, (b) the normalized mass ratio λ , and (c) the normalized diagonal separation S_1 over the course of each iteration of the optimization analysis for a lattice with $N = 2$. The solid line represents the mean value for the evolutionary optimization iteration (with population size $n = 30$ samples per iteration) and the shaded bounds represent the standard deviation from the mean. In this figure, it is apparent that the optimal value for λ is quickly identified by the algorithm.	121
A.27 Optimization analysis for infinite periodic structures. (a) Optimal value of critical buckling stress for varying number of diagonals. The color of each point represents the optimal mass ratio λ . (b) Optimal deformed geometries for designs including one to four diagonals. The color in each structure represents the magnitude of the displacement.	122
B.1 Schematic of central cylinder of a living sponge (lower porosity). The figure on the left shows the calculation for the area of the voids and the figure on the right shows the total area.	125

B.2 Schematic of central cylinder of a deceased sponge (higher porosity). The figure on the left shows the calculation for the area of the voids and the figure on the right shows the total area.	126
B.3 CFD domain illustration for solid models simulations. Illustration showing (a) sideways and (b) top view of the considered CFD domain. This illustration shows respective boundary conditions and is drawn to scale.	129
B.4 CFD domain illustration for porous models simulations. Illustration showing (a) sideways and (b) top view of the considered CFD domain. This illustration shows respective boundary conditions and is drawn to scale.	130
B.5 Empirical data for CFD Validation. Established empirical data for flow past a bluff cylinder. (a) Shows measurements for drag coefficient as a function of Reynolds number ^[8] with blue region indicating the measurements for $Re \approx 5,500$ and (b) shows measurements for Strouhal number as a function of Reynolds number ^[9] with blue region also indicating measurements for $Re \approx 5,500$. (c) Shows the simulation results for the drag coefficient over time and (d) for the PSD spectrum as function of Strouhal number. For both (c) and (d) the simulation results are shown in blue and the empirical data comparison in black dashed lines.	132
B.6 CFD meshing technique. Image obtained from <i>Ansys</i> [®] showing the meshing technique employed for the CFD model. Top row shows the mesh employed for the non-porous models and bottom row shows the mesh for the porous models.	133
B.7 Sponge Photos and Interpreted Designs. (a)-(j) shows pictures of sponge (top) and its corresponding interpreted design (bottom) . (a)-(j) correspond to Designs 1-10, respectively.	134
B.8 Structural Buckling Locations. FE model predictions of the locations of failures for each of the considered designs for various boundary conditions. Circles denote the location of the deformation. For the bending case, one direction was chosen and shown in the diagram. If circle is missing for a particular structure it is indicative of a global deformation for that particular structure under that particular loading condition.	135
B.9 Structural Buckling Deformations. This plot shows the buckling modes for the sponge, unidirectional and bidirectional ridge geometries. (a) Highlights the buckling mode for the geometries under uniaxial compression loading. Additional modes for more sponges are outlined in figure B.8. (b) Highlights the buckling modes for the geometries under cantilever bending loading. (c) Highlights the buckling modes for the geometries under torsion. These boundary conditions follow the loading described in main paper.	135
B.10 Lift coefficient changes as result of rotated geometry. This figure shows the time series of the lift coefficient for geometries in their original configuration with respect to the flow (blue line) and rotated 180° with respect to the flow (green line). Results are shown for (a) <i>Bidirectional</i> and (b) <i>Sponge</i> designs. Black dashed line shows the $y = 0$ axis of symmetry. Here we see that when we rotate the geometry by 180° the average lift is approximately flipped across the $y = 0$ axis line indicating that the non-symmetric ridge configuration breaks the flow symmetry and biases the lift to a particular direction.	136

C.1	Design elements of our inclined metamaterial. (a) Shows the inclined cut of our metamaterial from a square block of elastomeric matrix and its respective dimensions. On right is the exploded view of the assembly that includes the cut metamaterial and the films with its respective dimensions. (b) Shows the construction of the channel that are located along the top and bottom surfaces of the matamaterial. (c) Outlines the dimensions of the cut metamaterials in addition to the dimensions necessary to reconstruct the experimental sample.	139
C.2	Metamaterial fabrication. (a) The elastomer mixing cup and 3D-printed mold used for creating the sample. (b) Uncured elastomer is poured into the mold. (c) After allowing the elastomer to fully cure, the sample is removed from the mold. (d) Uncured elastomer is evenly poured on top of an acrylic sheet to create a thin film to be used as top and bottom sheets. (e) Two de-molded components are placed with channels face down on top of the cured thin sheet. (f) The thin sheets are glued to the samples using the same uncured silicone elastomer that was used for the other stages of the casting process. (g) The two structures are aligned, and (h) the two structures are glued together with the same elastomer. (i) A tube is punctured into the short edge and sealed with the same elastomer.	141
C.3	Volume Correction Plot for $\theta = 45^\circ$. This figure compares the pressure volume relationship between air and water as well as with air by correcting the compressibility effects using ideal gas law.	143
C.4	Out-of-plane displacement-3D reconstructions. (a) The elastomeric sample was coated with white spray chalk to give it a non-reflective surface. (b) A 3D scanner (Artec Space Spider) was used to obtain the full deformation profile of the structure. (c) 3D computer model of the structure after post-processing.	145
C.5	Buckling-induced surface geometries for different hole patterns. Finite Element results for five hole arrangements with $\theta = 0^\circ$ (top) and $\theta = 45^\circ$ (bottom) at $\Delta V/V_0 = 0$ and $\Delta V/V_0 = -1$, for square, triangular, hexagonal, rhombitrihexagonal, and trihexagonal arrays of holes. In the images, we show the normalized out-of-plane displacement, u_z/R_h	147
C.6	Deformation for samples with $\theta = 0^\circ, 15^\circ, 30^\circ$ and 45°. Photos of the metamaterial at $\Delta V/V_0 = 0$ (top) and at $\Delta V/V_0 = -1$ configurations for samples with $\theta = 0^\circ, 15^\circ, 30^\circ$ and 45° . Both top and side views are shown.	149
C.7	3D scans of the buckled samples. Top and side view of the scanned profile of samples with (a) $\theta = 0^\circ$ and (b) $\theta = 45^\circ$ at $\Delta V/V_0 = -1$	149
C.8	Sphere and plate placement. (a) Schematics showing the placement locations of the acrylic spheres on the bottom surface of $\theta = 0^\circ$ sample. In this configuration, the sample always has the same coefficient of friction independent of $\Delta V/V_0$. (b) Schematics showing the placement locations of the acrylic spheres on the bottom surface of $\theta = 45^\circ$ sample. In this configuration, the sample has low friction at $\Delta V/V_0 = 0$ and high friction at $\Delta V/V_0 = -1$. (c) Schematics showing the placement locations of the acrylic plates on the bottom surface of $\theta = 45^\circ$ sample. In this configuration, the sample has high friction at $\Delta V/V_0 = 0$ and low friction at $\Delta V/V_0 = -1$	150

C.9 Frictional properties of the metamaterial without acrylic features. (a) Photographs qualitatively showing the effect of the buckling-induced morphology on the tilting angle ϕ_{cr} for which samples with (a) $\theta = 0^\circ$ and (b) $\theta = 45^\circ$ and no acrylic feature attached to their bottom surface, began to slide. We find that for both samples, ϕ_{cr} is not affected by ΔV . (c) Coefficient of friction for the two samples as a function of $\Delta V/V_0$ 150

C.10 Deformation for samples with acrylic features attached to their surface. Photos at decreasing values of $\Delta V/V_0$ of the metamaterials with (i) $\theta = 45^\circ$ and acrylic plates; (ii) $\theta = 45^\circ$ and acrylic spheres; (iii) $\theta = 45^\circ$ and no acrylic features; (iv) $\theta = 0^\circ$ and acrylic spheres; (v) $\theta = 0^\circ$ and no acrylic features. 151

Listing of tables

A.1 3D Printed Model Caliper Sample Measurements. This table provides the caliper measurements averaged over $n = 3$ separate specimens for each design (values in black) as well as the expected values (bracketed values in red). All measurements reported were conducted prior to testing the samples. 101

A.2 Optimal 3×3 finite-sized structures. Geometric parameters defining the 3×3 structures with highest critical stress identified by CMA-ES for different numbers of diagonals. In each row we report the optimal parameter identified for a given number of diagonals N . For odd N , S_1 is constrained to 0, meaning it is not allowed to move from the non-diagonal elements junction. As the number of diagonals is increased λ decreases, indicating that the algorithm allocates more mass to the diagonal elements. 121

A.3 Optimal structures of infinite extent. Geometric parameters defining the infinite structures with highest critical stress identified by CMA-ES for different numbers of diagonals. Each column of the table corresponds to the optimal value of a parameter. Each row corresponds a determined N number of diagonals. For odd N , S_1 is constrained to 0, meaning it is not allowed to move from the non-diagonal elements junction. λ on average decreases as a function of N , which as expected, means the algorithm is allocating more volume to the diagonals as they are being spread too thin. The distribution of S as a function of N shows that the algorithm is attempting to evenly distribute the diagonal spacing, such that the length of the vertical elements without diagonal bracing is kept the shortest. 122

TO MY BEAUTIFUL AND LOVING WIFE ALAINA.

Acknowledgments

TO ALL OF THE INCREDIBLE PEOPLE WHOM ENABLED THE WORK PRESENTED IN THIS DISSERTATIONS.

These accomplishments would not have been possible without the guidance, support, and mentorship of a large number of people. I am forever grateful to all of those who have encouraged me throughout my career and it is my hope that in the next few paragraphs I can provide a small fraction of the recognition they deserve.

First and foremost, I would like to express my deep gratitude to my advisor, **Prof. Katia Bertoldi**, for continuously supporting me and providing me the flexibility and freedom to pursue my own projects with the ability to continuously focus on professional development. None of these projects would have been possible without her unwavering support, enthusiasm, and continuous encouragement.

I am equally grateful to my co-advisor, **Dr. James C. Weaver**, for always sharing his vast and diverse breadth of knowledge throughout the years. His constant support and our many conversations have not only been essential to the progress made in this dissertation but have also been a highlight of my graduate career.

I am also extremely thankful to my dissertation committee member **Prof. Chris Rycroft** for his suggestions and comments on my research throughout my PhD. Engagement with such great minds has not only helped me make progress on my research but also made me become a better scientist and engineer.

I want to thank all of my direct research collaborators – **Prof. Pai Wang, Sijie Sun, Prof. Vincent Tournat, Dr. Sophie C. Hofferberth, Lara Tomholt, Prof. Pedro J. del Nido, Prof. Martin Bechtold, Prof. Joanna Aizenberg, Prof. Robert J. Wood, Dr. Zian Jia, Prof. Mathias Kolle, Prof. Ling Li, Saurabh Mhatre, Dr. Antonio E. Forte, Prof. Bing Zhao, Prof. Olga Mesa, Patrick Cauchi-DuBois, Chiakara Inamura, Ted Sirota, Prof. Hossein Haj-Hariri, Prof. George Lauder, Emilia Zaria, Dr. Lishuai Jin, Dr. Paul Hanakata, Dr. Ahmad Zareei, Dr. Ida Pavlichenko, Prof. Andrew Gross, Prof. Joost Vlassak, Prof. Zhigang Suo, Prof. Michael Brenner, Dr. Nick Vasios, and Kevin Li** – for their hard work and for sharing their

talent.

During my graduate journey I was fortunate to have had the opportunity to receive a M.Eng.'15 in Engineering Sciences, a S.M.'20 in Computational Science and Engineering, and hopefully, a Ph.D.'21 in Applied Mathematics. Through this unconventional path I have had the privilege to collaborate with and be advised across various departments including the **Department of Earth and Planetary Sciences** and the **Institute for Applied Computational Science (IACS)**. I am grateful to all I have interacted with from both departments, but I want to especially thank my former masters advisor **Prof. James R. Rice** for his continued support and insightful discussions, and **Prof. Miaki Ishii** and **Prof. Pavlos Protopapas** for invaluable lessons.

Next, I want to thank the **Harvard Graduate School of Arts and Sciences** and the **Harvard Bok Center Learning Lab** for the opportunity to take part in the Harvard Horizons Symposium, which was a life changing experience. Particularly, I want to extend my sincere appreciation to **Prof. Shigehisa Kuriyama**, **Dean Sheila Thomas**, **Pamela Pollock**, **Marlon Kuzmick**, **Mara Sidmore**, **Dean Emma Dench**, and **Dean Xiao-Li Meng** for their guidance and support. I also want to thank my cohort fellows **Dr. Victoria Hwang**, **Dr. Shuang Frost**, **Dr. Jess Kanwal**, **Dr. Caitlin Nichols**, **Dr. Mateo Jarquin**, **Alex Shultz**, and **Daniel Walden** for their comradery and mutual support.

Furthermore, I want to thank the special community of the **Graduate Commons Program** who made Peabody Terrace my home away from home for many years. I am thankful for the lasting friendships with **Dr. Sonya Bhatia**, **Eric and Erika Fredrickson**, **Dr. Paul Tylkin**, **Dr. Amanda Sharick**, and **Lisa Valela**. I want to also thank Dudley House Faculty Deans and Peabody Terrace Resident Deans **Prof. James Hogel** and **Doreen Hogle** for their support and mentorship through all of the years.

A huge thank you to the **Harvard School of Engineering and Applied Sciences administrators and staff**, especially **John Girash**, **Ann Greaney-Williams**, and **Dean Fawaaz Habbal** whose hard work made being a graduate student much easier and more rewarding. Also, a huge thanks to the **Harvard Innovation Labs** staff for an incredible experience in the Venture Program, especially **Peter Gladstone** for his guidance in the consumer products section.

I further want to thank all of my colleagues in the Bertoldi group, namely, **Dr. Sahab Babae**, **LaShanda Banks**, **Dr. Elisa Boatti**, **Prof. Tal Cohen**, **Dr. Fionnuala Connolly**, **Catherine**

Ding, Dr. August Domel, Dr. Alexei Fomin, Dr. Antonio Elia Forte, Prof. Andrew Gross, Dr. Farhad Javid, Kausalya Mahadevan, Connor McCann, Eder Medina, Dr. Jochen Muller, Prof. Johannes T. B. Overvelde, Dr. Panos Pantidis, Prof. Ahmad Rafsanjani, Dr. Mehdi Torbati, Prof. Vincent Tournat, Stephanie Vincent, Yunfang Yang, Dr. Mohamed Zanaty, and Dr. Ahmad Zareei, for openly sharing their knowledge and providing support as well as insights into my research. I want to especially thank my exceptional office mates of Pierce 327, **Dr. Nick Vaisos, Dr. Gabriele Librandi, Bolei Deng, David Mélançon, Dr. Benjamin Gorissen, Dr. Thibaut Perol**, and **Prof. Colin Meyer**, for making my days so much fun and delightful.

I want to also thank my friends outside of the academic circle who have been incredibly supportive through every step of the way: **Dr. Florian Berlinger, Gustavo Bittencourt, Dr. Sören Brandt, Cole Diamond, Anthony Linderman, Dr. George C. Linderman, Dr. Wendy Linderman, Dr. Doug Brubaker, Dr. Mardochee Reveil, Garrett Bochicchio**. Furthermore, special thanks to my friend **Aaron Litvin** for proofreading this dissertation.

Above all, I want to thank my parents **Dula Fernandes, Lora Rand**, and **Almyr Fernandes** for their love, care, and constant support.

To all my other relatives, but especially my grandmother **Neyde Fernandes**, my aunt and godmother **Nea Ferreira**, my uncle and godfather **André Fernandes**, and my in-laws **John and Denise Schraufnagel** thank you for the encouragement.

Most importantly, I want to thank the love of my life **Alaina D. Fernandes**, who has been my source for all motivation and persistence. Alaina has kept me sane and has provided me with endless unconditional love that has inspired me to be my best self. She has supported me during the difficult times and celebrated with me during the good times. I feel blessed to have been able to share my life with her for the past 11+ years and counting.

Last but not least, thank you to my four-legged best friends **Crimson Bernoulli Fernandes** and **Clover Émilie Fernandes** for teaching me that true happiness in life is found when spending time with those one loves the most (and is also found in tasty treats).

I want to thank the financial support from **National Science Foundation Graduate Research Fellowship, Graduate Engineering Minority Consortium Fellowship, Corning Incorporated**, and the **Harvard Graduate School of Arts and Sciences Graduate Prize Fellowship** which have enabled me to pursue the research presented in this dissertation.

1

Introduction

“IT IS NOT THE STRONGEST OF THE SPECIES THAT SURVIVES, NOR THE MOST INTELLIGENT, BUT THE ONE MOST RESPONSIVE TO CHANGE.” – CHARLES DARWIN

1.1 Biomimetics and Structural Engineering

Nature has always served as a model for mimicking and as inspiration for humans in their desire to improve their lives. By adapting mechanisms and capabilities from nature, scientific approaches have helped humans understand related phenomena and associated principles in order to engineer novel devices and improve their capability.^[10] The ancient and inextricable tie between nature and engineering is clearly evident in the field of material science, starting with the use of stone, bones, antler, wood, and skin.^[1] Nearly since then, humans have made large advances in material science and engineering, many of which have occurred thanks to inspiration from nature and biology.

One of these advancements is evident in the development of the multi-billion-dollar velours and crochet (also known by its trademark VELCRO ©) as seen in figure 1.1. Its inventor, electrical engineer George de Mestral, worked *in-tandem* with nature and took inspiration from the structure of seed-bearing burr after being stuck with a plethora of burrs and having to remove them one by one.^[1,11] Another such example of *in-tandem* biological inspiration can be found in the honeycomb structure – inspired by the honeycomb from honey bees (figure 1.2(a)) – which is a

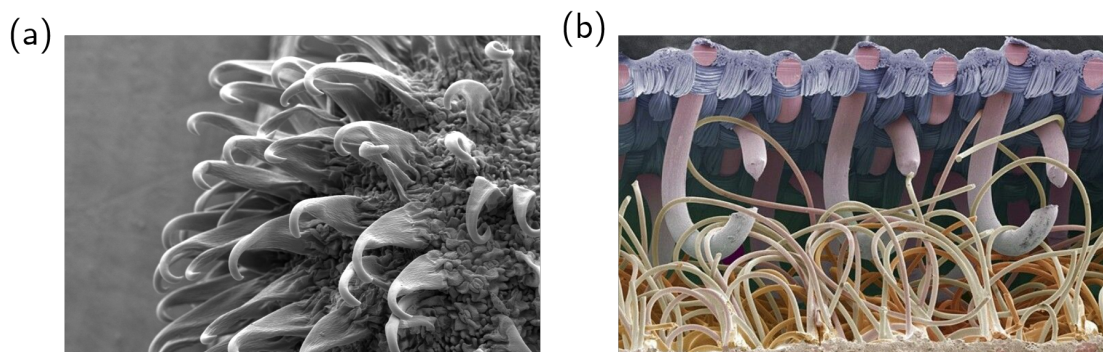


Figure 1.1: Microscope images of a burr seed, and a ‘velours and crochet’ (VELCRO ©). Inspired by the micro-structure of burr seeds as seen in (a) (Image Source), velours and crochet technology use microscopic hooks and loops to attach two surfaces together as seen in (b) (Image Source).^[1]



Figure 1.2: Honeycomb structure and applications. (a) Shows picture of honeycomb created by worker bees out of beeswax (Image Source). (b) Picture of a cross-section outer shell airplane wing (fuel tank removed) illustrating use of honeycomb as part of its structure (Image Source). (c) Ceramic substrate illustrating the implementation of honeycomb structures (Image Source) (smaller image shows where substrate is placed within catalytic converter. (Image Source))

hollow structure that minimizes the amount of material used while providing relatively high out-of-plane compression and shear properties.^[12] Man-made honeycomb structures are found in a variety of everyday applications^[13] ranging from the aluminum wings of an aircraft (figure 1.2(b)) to paper-based honeycomb cardboard boxes used as packaging materials. Furthermore, apart from its structural rigidity, honeycomb also serves as a key component in applications such as catalytic converters (typically found at the exhaust of internal combustion engines), where it provides a large surface area to catalyze harmful exhaust gases into less-toxic pollutants (figure 1.2(a)).^[14]

Likewise, many advancements in material science and structural mechanics occur *in-parallel* to nature and biology, where humans intuitively and mathematically find solutions to complex engineering problems for which the same solutions oftentimes can be found in natural settings. One such example is the structures found in birds which are optimized for weight while providing strength.^[15] The hollow bone of a vulture, for instance, is strengthened by V-shaped struts composed of layers connected by a tri-dimensional array of inclined struts, as seen in figure 1.3(a).^[1,15] This structure provides the stiffness required by minimizing the weight, since most of the mass is

displaced away from the neutral plane.^[1] Interestingly, researchers are developing very similar structures^[3], as shown in figure 1.3(b), where multi-functional periodic cellular metals, referred to as lattice materials, have a structure similar to that of the bone of birds and are developed using topological strategies aimed at reducing material usage and weight.^[3,16,17] Remarkably, this is a clear example of modern research finding solutions that have existed in biological systems for millions of years.

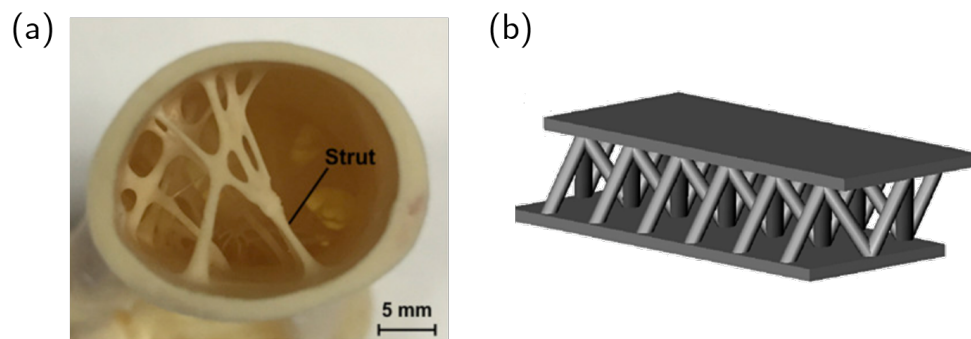


Figure 1.3: Structures of bones and trusses of cellular metals. (a) Hollow humerus bone from a Cape vulture's (*Gyps coprotheres*) distal end. The structure is stiffened by V-shaped internal struts in a three-dimensional configuration (Image Source).^[1,2] (b) CAD image of the truss core structure. The multifunctional cellular metals have a structure similar to that of the bone of birds (Image Source).^[2,3]

Additional examples of structural resistance can be found throughout the natural world, especially in the deepest parts of the ocean, where tough conditions can lead organisms to develop functional properties with interesting biomimetic potential.^[18] In the depths of the western Pacific Ocean, we find structural efficiency in a different fashion, particularly in the form of structural buckling resistance, where geometrical design plays a key role in the function of structural stability. The skeleton of a deep-sea glass sponge, *Euplectella aspergillum*, exhibits amazing hierarchical levels of structural and geometrical complexity^[6], each providing the essential components of structural design necessary for the conversion of the otherwise brittle constituent material (silica glass) into a sophisticated masterpiece of architectural evolution.^[19] This structure has been stud-

ied by scholars across multiple disciplines to expose some of the engineering lessons that have stood the test of time over millions of years.

In this dissertation I present my six years contributing to the advancement and development of structural material science by working both *in-tandem* and *in-parallel* with nature and biology, taking inspiration from glass sponges and porous mechanical metamaterial structures.

1.2 Glass Sponges



Figure 1.4: *Euplectella aspergillum* skeletal structure. Photographic image of a cleaned sponge specimen showing the full skeletal structure along with a dried pair of shrimps (faded orange region in middle left region of sponge). A side note: when living, the sponge also contains a pair of live shrimps that often permanently inhabit the sponge once they grow too big to leave it. These occupants have earned the sponge the status of a symbol of eternal love in Japan, where it is typically given as a wedding present.^[4,5]

In 1841, the English biologist Richard Owen marveled at the intricate skeleton of a new sea sponge species found near the Philippines.^[20] It resembled “a delicate cornucopia,” he wrote, one woven from “stiff, glistening, elastic threads, resembling the finest hairs of spun glass.”^[21] The skeleton is indeed made of glass, which the animal, *Euplectella aspergillum* — nicknamed “Venus’ flower basket,” — creates from raw materials extracted from the surrounding seawater. Hexactinellid glass sponges (the group to which Venus’ flower basket belongs) can be incredibly long-lived — some are thought to live many thousands of years, placing them among the longest-lived animals — and the thin glassy fibers that make up their skeletons can even possess the ability to channel light, in a manner similar to that seen in man-made fiber optics.^[4,5,19]

This intricate design of its glass skeleton is what inspired us to seek understanding of its functional significance. In chapter 2 of this dissertation, our work reveals that the skeleton is surprisingly strong considering the amount of material used in its construction. The skeleton’s strength derives from its peculiar lattice pattern, whose periodic architecture is neither intuitive nor simple. The glass beams that form the skeleton of the Venus’ flower basket, however, have a lot in common with trusses, the assemblages of beams used to stabilize bridges and skyscrapers. For well over a century, engineers’ preferred design for trusses has been a sturdy lattice consisting of a square grid with diagonals running in both directions for added support. The skeleton of the Venus’ flower basket, however, has pairs of diagonals running in both directions rather than the single diagonals crisscrossing a typical truss. These pairs are spaced apart so the grid looks like a checkerboard, with diagonals crossing every other square.^[6]

In our work, we fabricated and computer-simulated a lattice structure resembling the sponge and compared it with other lattice structures of the same weight, including standard engineering truss patterns. In experiments as well as simulations we saw that the bio-inspired lattice withstands

the greatest load – first from compression in one direction, and then in a three-point bending test – before yielding. In further simulations, we varied the number of diagonals as well as their spacing and thickness to find the lattice that could sustain the most compression. It turned out that the optimum, given the constraints, closely follows the sponge-inspired design.

Exhibiting a high strength-to-weight ratio is not all that Venus’ flower basket offers. The cylindrical lattice walls of its skeleton are just one of several levels of complexity in its structure. Zoom out from the diagonally reinforced structure and we see a macro-scale anatomy composed of yet another lattice formation, creating a series of right- and left-handed helical ridges, which are oriented perpendicular to the surface of the skeletal tube. Each unique design forms a maze-like organizational structure, one example of which can be seen in figure 1.4. These formations have been conjectured in previous studies^[6] to provide another layer of mechanical benefit to the sponge, as has been demonstrated for other reinforcing axial and helical rib-like elements found in tubular structures.^[22–24] In chapter 3 of this dissertation, we dive deep into the mechanics and functional significance of these unique ridge formations and explore not only their mechanical function, but also how this structure affects the fluid flow pattern around the sponge.

1.3 Mechanical Metamaterials

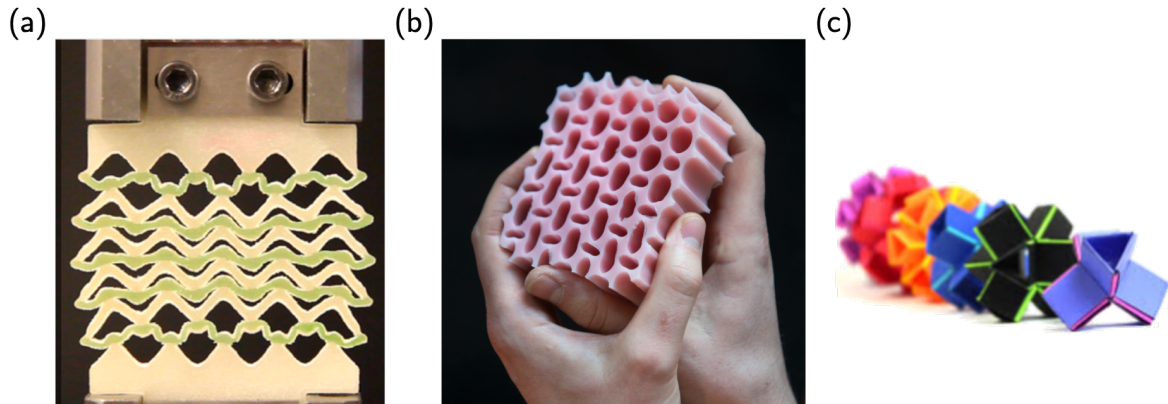


Figure 1.5: Mechanical metamaterials. This figure shows a select few different types of mechanical metamaterials. (a) Shows a multi-stable mechanical metamaterial that has been partially compressed.(Image Source) (b) Shows a programmable mechanical metamaterial that is being actuated with hands.(Image Source) (c) Shows a select number of building blocks used to create origami-inspired metamaterials.(Image Source)

Porous structural materials with well-defined periodicity are ubiquitous not only in nature but also in synthetic structures and devices. These types of materials have proven to offer various types of auxetic behavior, ranging from negative Poisson's ratio^[25–35] to high energy absorption^[29,36] and excellent acoustic damping^[37,38]. Mechanical metamaterials, which constitute a more recent branch of metamaterials^[39], borrow ideas from wave-based metamaterials to achieve shape morphing^[40–56], topological protections^[37,57–80], instabilities, and non-linear responses^[81–93] to obtain unexpected functionalities, as seen in figure 1.5.

The simplest example of such a metamaterial is a buckling-based square array of circular holes embedded in an elastomeric sheet^[39] (as illustrated in figure 1.5(b)), which can be decomposed into an array of rigid domains connected by beams. When the structure is uni-axially compressed, the buckling of the beam-like ligaments triggers a sudden transformation of the holes into a periodic pattern of alternating and mutually orthogonal ellipses. Thus, this type of metamaterial combines

the shape-morphing properties of the underlying mechanism of hinged squares with the mechanical functionality of the beam elements that connect them.

One crucial observation for the vast field of shape-morphing porous mechanical metamaterials is that their deformation has historically remained planar and characterized by 2D morphologies^[25–31]. However, in chapter 4, we introduce a new way to parameterize these structures to achieve a 3D deformation pattern induced on the surface of the planar structure. In this chapter, not only do we characterize this corrugation pattern, but we also utilize it to control light scattering and friction, while also creating a crawling robot.

1.4 Dissertation Structure and Overview

Chapters 2 to 4 form the core of this dissertation, and each chapter is based on a first-author article published in or submitted to a peer-reviewed journal. The core of the dissertation is subdivided into two themes: 1. working *in-tandem* with nature and biology (chapters 2 and 3); and 2. working *in-parallel* with nature and biology (chapter 4).

First, chapter 2 illustrates the power of seeking inspiration from nature to devise innovative solutions in a field that has remained, to a great extent, stagnant for hundreds of years. Diagonally reinforced lattice truss structures were first patented in the 1820's by Connecticut architect Ithiel Town^[94,95], who created covered bridges that utilized his technology for strength while remaining light-weight. Since then, few iterations were made to the original design, marginally improving its strength and functionality. This chapter explores design principles learned from the glass sponge *Euplectella aspergillum* to improve diagonally reinforced lattices by leveraging the use of rapid prototyping, such as 3D-printing, as well as finite element modeling. Here, we construct and

test various lattice designs, including those inspired by the sponge, for their ability to withstand structural buckling in various loading conditions. We demonstrate that by rearranging diagonal reinforcement elements within a periodic square lattice, as observed in the skeletal system of the sponge, we can create a structure capable of withstanding $\sim 25\%$ higher buckling loads over existing commonly used designs – all while using the same amount of material. Furthermore, by utilizing an evolutionary optimization algorithm, we show that our sponge-inspired truss structure is extremely close to the optimal configuration within the design space.

Chapter 3 expands the sponge analysis to another length scale by studying the macro-scale skeletal organization including its system of ridges that is overlaid on its truss design. Combining finite element analysis and computational fluid dynamics, we study the functional significance of its unique and regular ridge design. From these investigations, we discover that not only do these ridges provide additional mechanical reinforcement, but, more significantly, they provide a critical hydrodynamic benefit by effectively suppressing von Kármán vortex shedding and reducing fluctuations in lift forcing over a wide range of flow regimes. The significance of these biological results directly translates to engineering applications, where vortex-induced vibrations can excite structural resonances with the potential to lead a structure to catastrophic collapse or permanent damage. To explore this application, we compare the sponge-inspired ridge design to commonly employed helical strakes used to suppress shedding.

Finally, in chapter 4 we do not seek inspiration from biology, but instead follow a research path *in-parallel* with nature, by focusing on porous metamaterials with well-defined periodicity. These materials have proven to show a wide range of behaviors, from negative Poisson's ratio to high energy absorption and acoustic controls. However, existing studies have harnessed the power of these materials by simply using their 2D morphologies. In this chapter, we describe and quantify

the emergence of 3D morphologies triggered by mechanical instabilities. To illustrate how the various 3D patterns can be utilized in practical applications, we create prototypes that harnesses their corrugation properties to separately control both friction and light. Using a modular approach, we showcase a soft robot that is able to utilize friction control properties to induce locomotion through the utilization of a single vacuum input.

As stated previously, this dissertation contains only chapters with major contributions (i.e., first-author publications); however, details on additional contributions (i.e., non-first-author publications) can be found in chapter 5. Furthermore, additional details, in the form of supplementary information for chapters 2 to 4, can be found in the latter appendix chapters. Lastly, a complete list of contributions can be found in the ‘*List of Publications/Patents*’ section at the end of the dissertation.

2

Mechanically Robust Lattices Inspired By Deep-Sea Glass Sponges

BY: MATHEUS C. FERNANDES, JOANNA AIZENBERG, JAMES C. WEAVER, AND KATIA BERTOLDI. PUBLISHED IN *NATURE MATERIALS*, ON SEPT. 21 2020. [doi:10.1038/s41563-020-0798-1](https://doi.org/10.1038/s41563-020-0798-1)

2.1 Abstract

The predominantly deep-sea hexactinellid sponges are known for their ability to construct remarkably complex skeletons from amorphous hydrated silica. The skeletal system from one such example, *Euplectella aspergillum*, consists of a square-grid-like architecture overlaid with a double set of diagonal bracings, creating a checkerboard-like pattern of open and closed cells. Here, using a combination of finite element simulations and mechanical tests on 3D-printed specimens of different lattice geometries, we show that the sponge’s diagonal reinforcement strategy achieves the highest buckling resistance for a given amount of material. Furthermore, using an evolutionary optimization algorithm, we show that our sponge-inspired lattice geometry occurs near the design space’s material distribution optimum. Our results demonstrate that lessons learned from the study of sponge skeletal systems can be exploited for the realization of square lattice geometries that are geometrically optimized to avoid global structural buckling, with implications for improved material use in modern infrastructural applications.

2.2 Introduction

The mineralized skeletal system of the hexactinellid sponge, *Euplectella aspergillum*, commonly known as Venus’ Flower Basket, has received significant attention from the engineering and materials science communities for its remarkable hierarchical architecture and mechanical robustness across multiple length scales. Its constituent glassy skeletal elements (spicules) consist of a central proteinaceous core surrounded by alternating concentric layers of consolidated silica nanoparticles and thin organic interlayers.^[18,20,96] These spicules are further organized to form a highly regular

square grid, reinforced by two intersecting sets of paired diagonal struts, creating a checkerboard-like pattern of alternating open and closed cells (figure 2.1). While the effects of the spicules' laminated architecture in retarding crack propagation^[97] and increasing buckling strength^[98] have been demonstrated previously, the potential mechanical benefits imposed by the double diagonal square lattice created from the assembly of these constituent spicules remains largely unexplored.

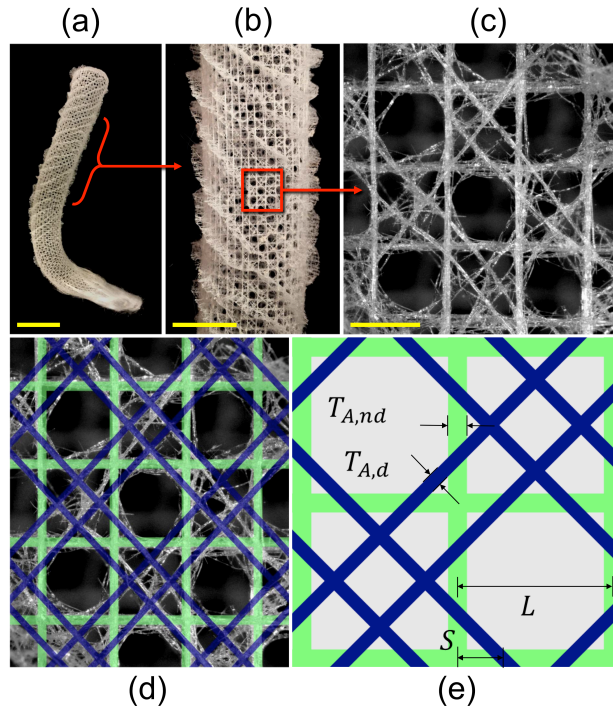


Figure 2.1: Representative skeletal system of the hexactinellid sponge *Euplectella aspergillum*. (a-c) Progressively magnified views of the sponge's skeletal system. (d) Composite overlay of the idealized truss model (green and blue lines) and the sponge's underlying skeletal structure. (e) Schematic of our sponge-inspired lattice with rectangular cross-section (*Design A*) comprising non-diagonal elements with length L and thickness $T_{A,nd}$ and diagonal elements with thickness $T_{A,d}$ located at a distance S from the nodes. Scale bars: (a) 4 cm; (b) 2 cm; (c) 2.5 mm.

Grid-like, open-cell lattices, such as those found in the skeletal system of *E. aspergillum* are commonly employed in engineering contexts, owing to their reduced weight^[99,100], high energy absorption^[3], and ability to control the propagation of acoustic^[101] and thermal waves^[13,17,102]. Generally, the properties and functionality of such geometries are dictated by their node connec-

tivity. For example, a minimum node connectivity of 6 is required for 2D lattices to be stretching-dominated, and therefore achieving a higher strength-to-weight ratio for structural applications^[103]. In contrast, lattices with simple square geometries (node connectivity of 4), are unstable when the loading vector has a transverse component (they are bending-dominated, and the only shear resistance arises from the joints)^[104], and typically require diagonal bracing for stabilization.^[105]

In this paper, we use the skeletal anatomy of *E. aspergillum* as inspiration for the design of mechanically robust square lattice architectures (more information on the sponge skeletal structure can be found in section A.1 and figure A.1). First, we use a combination of experimental and numerical analyses to investigate the mechanical properties of the sponge’s skeletal lattice. We then employ an optimization algorithm to identify the beam configuration in a diagonally reinforced square lattice that achieves the highest critical load, revealing unexpectedly, that the skeletal system of *E. aspergillum* is very close to this design optimum. These results demonstrate that an integrated work flow, combining biological, computational, and mechanical testing approaches, can guide the design of lattice architectures which are structurally more robust than those currently employed in modern infrastructure and devices.

2.3 Design Considerations

To understand the mechanical benefits of the sponge’s skeletal architecture, we compared the performance of its geometry to that of three other 2D square base lattices, all with the same total volume (i.e. the same total amount of material), to ensure a fair comparison^[104]. In each of these structures, the base square architecture was comprised of elements with lengths L , and with rectangular cross sections characterized by a depth H large enough to avoid out-of-plane deformation.

More specifically, we considered *Design A*, which was inspired by the sponge and comprised horizontal and vertical elements with thickness $T_{A,nd} = 0.1L$ and two sets of parallel double diagonals with thickness $T_{A,d} = 0.05L$ located at a distance $S = L/(\sqrt{2} + 2)$ from the nodes (figure 2.2(a)); *Design B*, which was similar to the sponge-inspired design with $T_{B,nd} = 0.1L$, but only contained a single diagonal with thickness $T_{B,d} = 0.1L$ crossing each of the closed cells (figure 2.2(b)); *Design C*, which was inspired by the bracings found in modern engineering applications with $T_{C,nd} = 0.1L$ and contained a crossed set of diagonal beams with thickness $T_{C,nd} = 0.05L$ in every cell (figure 2.2(c)); and *Design D*, with no diagonal reinforcement, and with horizontal and vertical elements with thickness $T_{D,nd} = 0.1L(1 + 1/\sqrt{2})$ (figure 2.2(d)). Note that in an effort to further provide a fair comparison, the volume ratio of diagonal to non-diagonal struts was also identical for *Designs A*, *B*, and *C* (see section A.2 and figures A.2 to A.5 for details and assumptions).

2.4 Experimental and Numerical Results

We began our analysis by comparing the mechanical response under uniaxial compression along the vertical elements of the four lattices described above. Samples comprising 6×6 tessellations of square cells with $L = 1.5$ cm and $H = 4$ cm were fabricated with a Connex500 multi-material 3D printer (Stratasys, Eden Prairie, Minnesota, United States) from a Shore A 95 durometer material (digital elastomer FLX9795-DM) and compressed uni-axially using a single axis Instron (Model 5969) with a 50 kN load cell (figure 2.2(e)). Two key features emerged from the stress-strain curves reported in figure 2.2(f). First, we found that all designs with diagonal reinforcement (i.e. *Designs A-C*) were characterized by a nearly identical initial elastic response, demonstrating that the different diagonal reinforcement designs did not impact the structure's initial overall stiffness.

Design D, as expected, exhibited a higher initial stiffness because of its thicker vertical and horizontal elements. Second, all curves showed a clear maximum load bearing capacity, with *Design A* (the sponge-inspired design) accommodating the highest load. Since each maximum load corresponded to the onset of buckling, we inferred that *Design A* displayed the highest critical buckling stress between the considered designs. Furthermore, we found that in all three designs with diagonals, the post-buckling behavior resulted in a homogeneous pattern transformation throughout the sample (figure 2.2(e)). In contrast, for *Design D*, the critical mode resulted in a much larger wavelength than the size of a square unit cell and resulted in a post-buckled shape qualitatively similar to that of a compressed buckled beam (more information on the experimental methods can be found in section A.3 and table A.1).

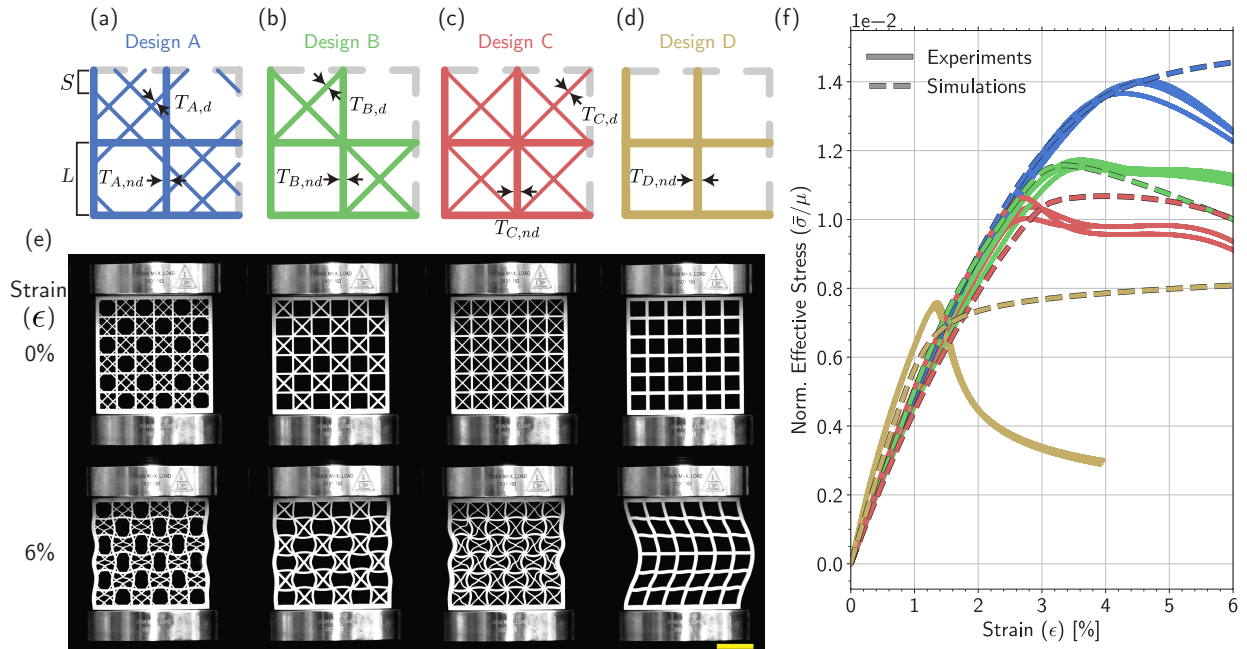


Figure 2.2: Experimental and numerical results. (a)–(d) Schematics of the different lattice geometries (*Design A–D*) considered in this study. (e) Mechanical deformation snapshots of the different 3D-printed models at 0% applied strain (top row) and 6% applied strain (bottom row). Scale bar: 3 cm. (f) Numerical (dashed lines) and experimental (solid lines) stress-strain curves for $n = 3$ independently tested samples of each design. Curves in this plot are color coded according to (a)–(d). All designs are characterized by the same total volume and mass ratio allocation between non-diagonals and diagonal elements.

In an effort to understand how the sponge-inspired lattice design resulted in significantly improved mechanical performance, we conducted Finite Element (FE) simulations using ABAQUS/Standard (Dassault Systèmes SE, Vélizy-Villacoublay, France). For these analyses, the geometries were constructed using Timoshenko beam elements (ABAQUS element type B22) and the material's response was captured using an incompressible Neo-Hookean material model with a shear modulus $\mu = 14.5$ MPa. Our simulations consisted of three steps: (i) a buckling analysis (*BUCKLE step in ABAQUS) was conducted to obtain the buckling modes for each of the structures, (ii) a perturbation in the form of the lowest buckling mode was then applied to the nodes of the mesh, and (iii) a static non-linear analysis (*STATIC step in ABAQUS) was performed to evaluate the nonlinear large deformation responses. To verify the validity of our analyses, we investigated the responses of models identical to those specimens tested in our Instron compression studies. As shown in figure 2.2(f), we found close agreement between the numerical and experimental results up to the onset of buckling, confirming the accuracy of our simulations for capturing the linear regime and critical load. Next, we extended our FE model to explore the effects of loading direction. To reduce computational cost and eliminate edge effects, we capitalized on the periodicity of the structures and investigated the response of Representative Volume Elements (RVEs) with suitable periodic boundary conditions^[106,107] (see section A.4 and figures A.6 to A.24 for details and additional numerical analysis). Figure 2.3(a) shows the evolution of the structures' effective stiffness, \bar{E} , as a function of the loading angle θ . We found that the stiffness of all structures containing diagonal reinforcement was virtually identical for any loading angle, further confirming that the structural stiffness was predominantly governed by the amount of material allocated along the loading direction. As a result, *Design D*, in which all of the material was allocated to the non-diagonal elements, exhibited the highest stiffness for $\theta = 0^\circ$, but had almost negligible load-bearing

capacity for $\theta = 45^\circ$, where the only contribution to its stiffness came from the minimal bending resistance of the joints (see figure A.21 for a detailed analysis of the effect of joint stiffness).

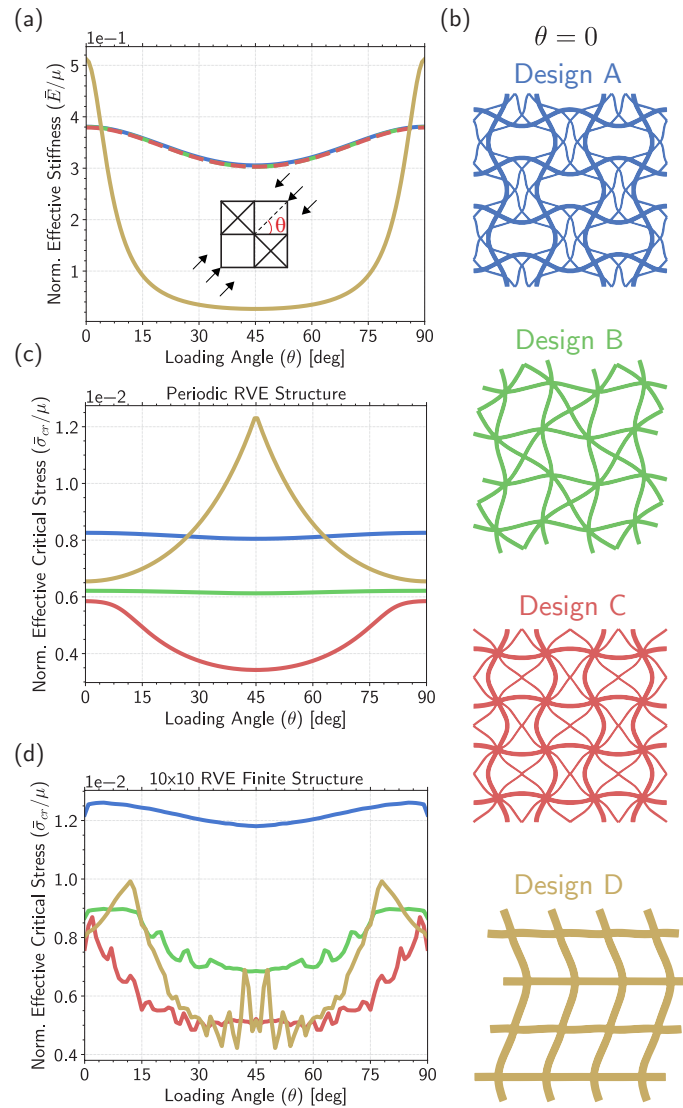


Figure 2.3: Numerical results describing structural response to varying loading angle. (a) Evolution of the structural stiffness for infinite size periodic lattice designs as a function of loading angle θ . (b) Critical buckling modes for *Design A-D* at $\theta = 0^\circ$. (c) Evolution of the effective buckling stress for the different lattice designs as a function of loading angle θ . Results are obtained by simulating a super-cell with 10 by 10 unit and periodic boundary conditions. (d) Evolution of the effective buckling stress as a function of the loading angle θ for finite (non-periodic) lattice structures comprising 10 by 10 unit cells. In each plot, the line color corresponds to the designs by color in (b). All designs are characterized by the same total volume and mass ratio allocation between non-diagonal and diagonal elements.

Next, we investigated the effect of θ on the buckling behavior of *Designs A-D*. We found that the

effective critical buckling stress ($\bar{\sigma}_{cr}$) of *Design A* was higher than the other diagonally reinforced designs (namely *Design B* and *Design C*) for all values of θ (figure 2.3(b)). *Design D* surpassed *Design A* for $27^\circ < \theta < 63^\circ$ when considering an infinite structure. However, given the global nature of the buckling mode for *Design D*, such performance was largely affected by boundary effects and the critical buckling stress was significantly reduced when considering a finite size structure comprising 10×10 RVEs (figure 2.3(d) - see also figure A.20). Furthermore, the *Design A* geometry maintained its robustness even after modifications to the lattice through the introduction of various levels of disorder, an observation consistent with the features observed in the native sponge skeleton (see figure A.23 and figure A.24).

2.5 Optimization Results

Having demonstrated the benefits of the sponge-inspired design (*Design A*) compared to *Designs B-D*, we wondered whether there existed a different diagonally reinforced square lattice design with even higher critical buckling stress. To address this question, we formulated an optimization problem to identify the number of diagonals, N , their distance from the nodes of the square lattice S_i (with $i = 1, 2, \dots, N$), as well as the ratio between diagonal and non-diagonal elements $\lambda = V_{nd}/V_d$ (V_{nd} and V_d being the volume of the non-diagonal and diagonal elements, respectively) that resulted in the highest buckling stress. Specifically, we considered finite size structures composed of 3×3 RVEs and focused on uni-axial compression parallel to the non-diagonal elements (i.e. $\theta = 0^\circ$), while constraining the total volume of the RVE to match that of the designs considered in figure 2.2. We maximized the objective function $\mathcal{Z} = \bar{\sigma}_{cr}$ using FE simulations coupled to a Python implementation of the Covariance Matrix Adaptation Evolution Strategy algorithm (CMA-ES)^[108]

(more information on the implementation found in section A.5, figures A.25 to A.27 and tables A.2 and A.3). For each set of inputs identified by CMA-ES, a FE buckling analysis was conducted to obtain $\bar{\sigma}_{cr}$ and, therefore, evaluate the objective function \mathcal{Z} . We conducted seven separate optimizations, each considering a fixed integer number of diagonal elements N , ranging from one to seven ($N = \mathbb{Z} \in [1, 7]$). Given the high strength of lattices reinforced by diagonals aligned at a 45° angle^[109], in all the runs we assumed that all of the diagonals were oriented at 45° with respect to the non-diagonal members and that V_d and V_{nd} were distributed equally among the diagonal and non-diagonal elements, respectively. Furthermore, to ensure symmetry, we assumed that $S_{2i-1} = S_{2i}$ ($i = 1, 2, \dots, N/2$) if N is an even number and $S_1 = 0$ and $S_{2i-1} = S_{2i}$ ($i = 2, 3, \dots, (N-1)/2$) for odd values of N . In figure 2.4(a) we report the highest $\bar{\sigma}_{cr}$ identified by CMA-ES for all considered number of diagonals N . Remarkably, we found that the highest $\bar{\sigma}_{cr}$ was only 9.55% higher than that of *Design A* and occurred for a design similar to the sponge-inspired one (with two diagonals located at a distance $S = 0.1800L$ from the nodes, and volume distributed so that $\lambda = 0.6778$). As such, this numerical prediction, which was validated by experimental results (figure 2.4(b)), demonstrated that the sponge-inspired design was extremely close to the design exhibiting the highest critical stress.

2.6 Discussion

Thus far, we demonstrated that the skeletal organization pattern found in *E. aspergillum* could be adapted to realize lattice structures with high buckling resistance under uniaxial compression. However, it should be noted that the superior mechanical performance of the sponge-inspired lattice (i.e. *Design A*) is not limited to this loading condition. To demonstrate this important point, figure 2.5

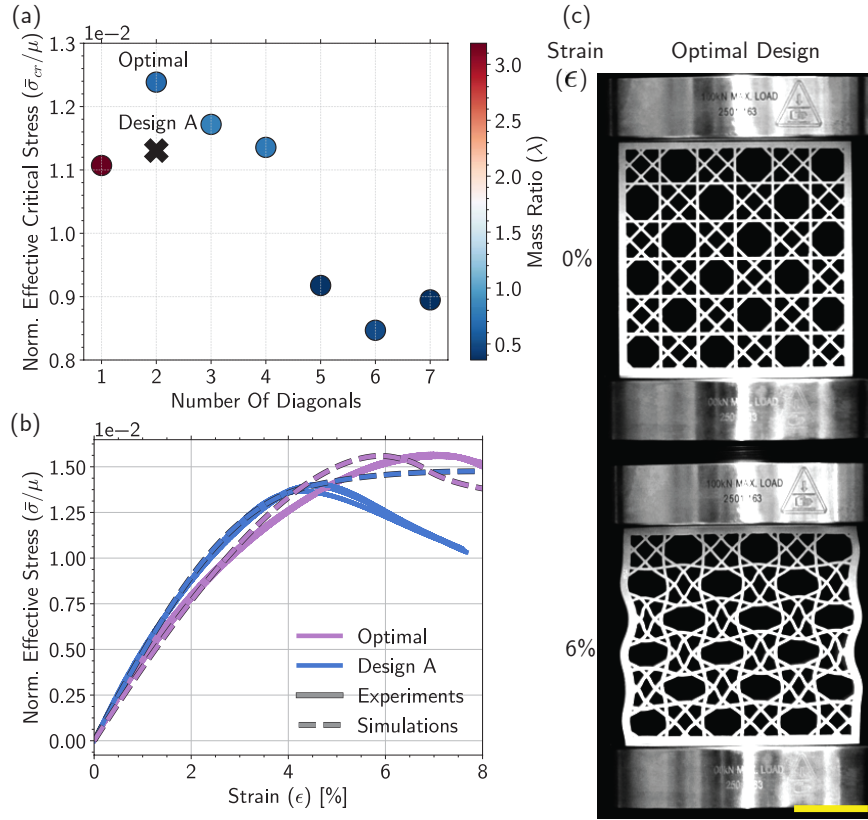


Figure 2.4: Optimization results and experimental validation. (a) Optimal value of critical buckling load for varying number of diagonals. The color of each point represents the optimal mass ratio λ . (b) numerical (dashed lines) and experimental (solid lines) stress-strain curves for $n = 3$ independently tested samples of *Design A* and the optimal design. (c) Experimental snapshots of the optimal design at 0% applied strain (top figure) and 6% applied strain (bottom figure). Scale bar: 3 cm.

shows results for a slender tessellation of 11×2 square cells loaded in three point bending. In this scenario, using an Instron, the slender geometry was mounted in a three-point bending configuration and a displacement δ_{appl} was applied at the top center of the geometry. As the displacement was applied, the reaction force was measured and plotted in figure 2.5(b) for the various geometries. Both our experiments and FE simulations demonstrated that the sponge-inspired design was stiffer and could withstand 15% higher loads over a larger range of applied displacements, illustrating the potential benefit of incorporating such a design into suspended structures. We further used FE simulations to evaluate the performance of Designs A-D in 5 other loading regimes. For all of

the loading cases considered (see figures A.9 to A.12), we found that *Design A* was able to withstand significantly higher loads than any of the other structures – making it the best candidate to realize load bearing structures for a variety of applications. Although in this study, we focused on lattices at the centimeter scale, we want to emphasize that our approach can be extended to design structures over a wide range of length scales as long as within the continuum limit. However, in our analysis, we did not account for the effect of gravity, which could become a significant source of loading for large-scale structures.

2.7 Conclusion

In summary, through the analysis of the skeletal organization of *E. aspergillum*, we discovered that its non-trivial, double-diagonal, checkerboard-like square lattice design provides unprecedented mechanical performance. We compared the sponge-inspired lattice (*Design A*) to other common diagonally reinforced square lattices (*Design B-C*) and a non-diagonally reinforced lattice (*Design D*), all with the same total mass, and found that the sponge-inspired design provides a superior mechanism for withstanding loads prior to the onset of buckling for a wide range of loading conditions. Additionally, by using optimization tools to survey a broad multi-dimensional design space, we found that the sponge skeletal architecture is nearly identical to the lattice design that provides the highest critical stress under uniaxial compression.

The results presented here, therefore demonstrate that by intelligently allocating material within a square lattice, it is possible to produce structures with optimal buckling resistance, without the need to add additional material to the system. The mechanical properties of the sponge-inspired lattice described here thus have implications for improving the performance of a wide range of truss

systems, with applications ranging from large-scale infrastructure such as bridges and buildings, to small-scale medical implants.

While not the primary focus of the present study, the results presented here may also shed new light on functional aspects of the skeletal organization in *E. aspergillum*. It is important to note that skeletal maturation in this and related species progresses through two distinct phases (a "flexible" phase and a "rigid" phase), ultimately resulting in the terminal growth form shown in figure 2.1^[7,20,110]. In the early "flexible" stage of growth, the vertical, horizontal, and diagonal skeletal struts are not fused to one another, and thus can accommodate radial expansion of the skeletal cylinder. In addition, at this point, the mechanical behavior of the sponge skeleton is dominated by the properties of the individual spicules, which have been reported to support significant bending deformation and fail at strains greater than those found for buckling in our lattices, namely at strains greater than $\varepsilon \approx 0.04$ ^[111,112]. Once the maximum length and width of the cylindrical lattice is achieved, the skeleton goes through a series of rigidification steps, resulting in a progressive stiffening of the skeletal system through nodal fusion of the vertical, horizontal, and diagonal struts via the deposition of a lower modulus laminated silica cement^[113], followed by the addition of the spiraling external ridges and additional densification of the skeleton. Therefore, while the results presented here are thus unlikely to be biologically relevant with regards to the fully mature skeleton shown in figure 2.1, they may very well be relevant during the early stages of skeletal consolidation in this and related species where the buckling strains exceed the laminate yield strains^[111–113].

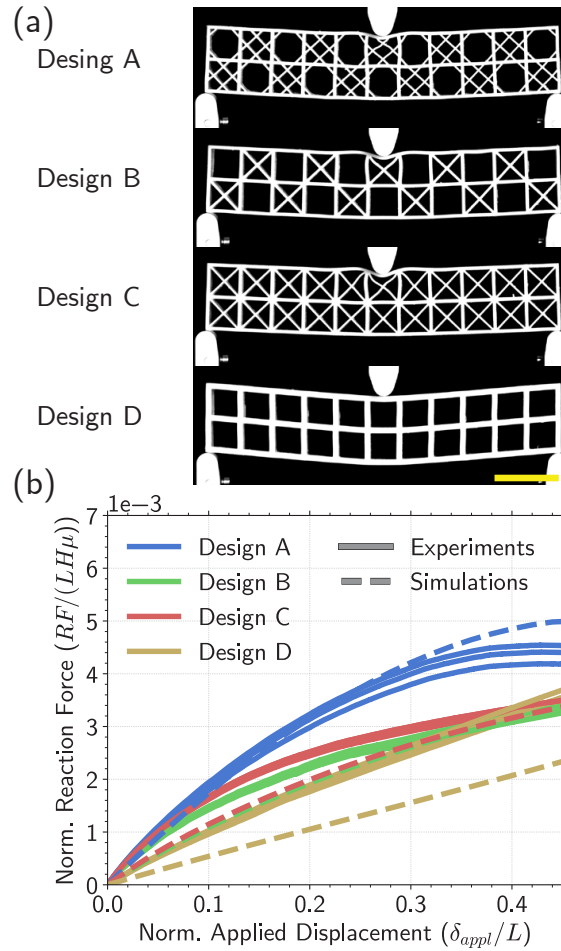


Figure 2.5: Numerical and experimental results of slender structures undergoing 3-point bending tests. (a) Experimental snapshots of the four lattices comprising 11×2 square cells when loaded in 3-point bending at $\delta_{appl}/L = 0.45$. Scale bar: 3 cm. (b) Evolution of $n = 3$ experimentally obtained samples (continuous lines) and numerically (dashed lines) recorded reaction forces for the four designs as a function of the applied displacement.

Methods and Materials

Parameter derivation and explanation of each geometry can be found in section A.2. Details on the fabrication of the samples and the protocol for testing can be found in section A.3. The numerical setup and explanation for the FE analysis can be found in section A.4. Additional numerical analysis including parameter exploration and consideration for different cross-sectional geometries is

presented in section [A.4.2](#). A detailed description of the optimization algorithm can be found in section [A.5](#).

3

Mechanical and Hydrodynamic Analyses of Helical Strakes in the Skeletons of Glass Sponges

BY: MATHEUS C. FERNANDES, MEHDI SAADAT, PATRICK CAUCHI-DUBOIS, CHIKARA INAMURA, TED SIROTA, HOSSEIN HAJ-HARIRI, GEORGE LAUDER, KATIA BERTOLDI, JAMES C. WEAVER. SUBMITTED TO *ROYAL SOCIETY INTERFACE*, JULY 2021.

3.1 Abstract

From the discovery of functionally graded laminated composites, to near-structurally optimized diagonally reinforced square lattice structures, the skeletal system of the predominantly deep-sea sponge *Euplectella aspergillum*, has continued to inspire biologists, materials scientists, and mechanical engineers. Building on these previous efforts, in the present study, we develop an integrated finite element and fluid dynamics approach for investigating structure-function relationships in the complex maze-like organization of helical ridges that surround the main skeletal tube of this species. From these investigations, we discover that not only do these ridges provide additional mechanical reinforcement, but perhaps more significantly, provide a critical hydrodynamic benefit by effectively suppressing von Kármán vortex shedding and reducing lift forcing fluctuations over a wide range of biologically relevant flow regimes. By comparing the disordered sponge ridge geometry to other more symmetrical strake-based vortex suppression systems commonly employed in engineering contexts ranging from antennas to underwater gas and oil pipelines, we find that the unique maze-like ridge organization of *E. aspergillum* can completely suppress vortex shedding rather than delaying their shedding to a more downstream location, thus highlighting their potential benefit in these engineering contexts.

3.2 Introduction

The geometrically complex siliceous skeletal systems of marine sponges have attracted a great deal of attention from the scientific community due to their multi-scale structural hierarchical organization and remarkable damage tolerance^[18,98,114]. For example, the mineralized tubular skeleton

from one such species, *Euplectella aspergillum* consists of bundles of individual needle-like elements (spicules) that are cemented together to form a diagonally reinforced square lattice-like structure that is further covered by a series of helical ridge-like features^[6,96]. Detailed investigations into the various components of this structural hierarchy have revealed their surprising mechanical benefits.

First, single-spicule studies have revealed the presence of an underlying laminated architecture consisting of concentric lamellae of consolidated silica nanoparticles separated by thin organic interlayers. The silica layers decrease in thickness from the spicule core to its periphery, resulting in a functionally graded design that effectively retards crack propagation through the spicules, while simultaneously increasing their buckling resistance^[112,114].

At a second level of structural hierarchy, bundles of these laminated spicules are further organized into a square lattice-like structure which is reinforced by pairs of diagonal struts that cross through every other cell of the lattice, creating a checkerboard-like organization. Through a combination of finite element simulations and direct mechanical testing, it has been demonstrated that this non-intuitive diagonal reinforcement strategy creates a geometry that exhibits a near-optimal strength-to-weight ratio for this specific family of truss structures^[115].

Finally, surrounding the underlying diagonally reinforced square lattice are a series of right and left-handed helical ridges, which are oriented perpendicular to the surface of the skeletal tube and form a distinctive maze-like organization. While previous studies have speculated that these ridge-like features provided a mechanical benefit to the sponge^[6], as has been demonstrated for other reinforcing axial and helical rib-like elements on tubular structures^[22–24], the striking morphological similarity of the sponge ridges to helical strakes used for vortex suppression in cylindrical structures under flow^[116–119] motivated the present study which explores their potential hydrody-

dynamic functionality.

Vortex shedding is a topic of great concern to the engineering community, not only for its ability to excite vortex-induced vibrations (VIV), potentially leading to resonance structural vibrations^[9,116], but also for its periodic forcing effects and noise generation^[119]. Fluid flow past bluff cylindrical structures is known to generate vorticity due to the presence of shear in the fluid's boundary layer. These small vorticity regions coalesce into regions of concentrated vorticity (known as vortices) on both sides of the cylinder, leading to a phenomenon known as von Kármán vortex shedding.^[116] Because of the implications of von Kármán vortex shedding on the structural integrity of cylindrical forms, the addition of helical strakes (protruding ridge-like elements) is commonly employed as a method to suppress this effect.^[117,119]

Here, we describe a computational framework for investigating structure-function relationships of the complex helical ridge system in the skeleton of *Euplectella aspergillum*. Using an integrated approach that combines finite element simulations and computational fluid dynamics, we explore both the mechanical and hydrodynamic effects of these skeletal features and compare these results to alternative ridge geometries employed for similar functions in their synthetic engineering analogues.

3.3 Skeletal Geometry

As demonstrated from previous studies^[6], the skeletal system of a fully mature specimen of *E. aspergillum* (figure 3.1(a)) is covered with a laminated silica cement, forming a rigid construct, and contains a maze-like network of external helical ridges that extend perpendicular to the skeletal tube. To explore the organizational details of this complex ridge system, we examined ten differ-

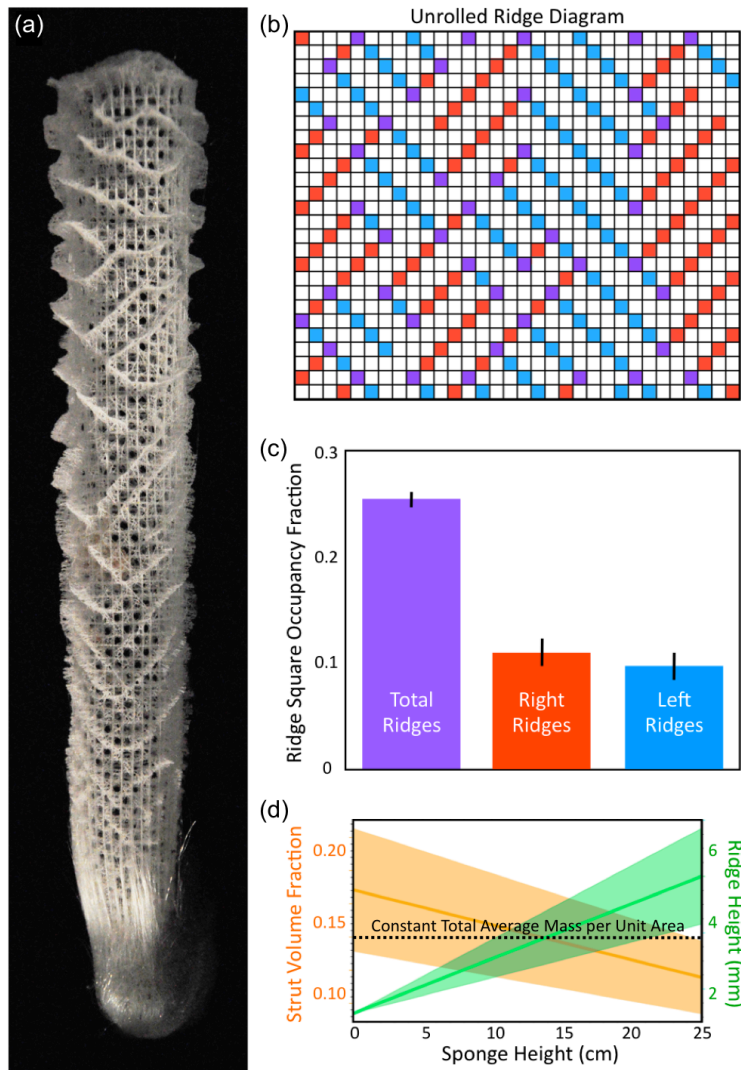


Figure 3.1: Skeletal features of *Euplectella aspergillum*. (a) Photograph of a cleaned and dried siliceous skeleton of *E. aspergillum*, clearly depicting its tapered tubular form, its highly regular diagonally reinforced checkerboard-like square lattice structure, and its complex network of external ridges. (b) Unrolled ridge diagram illustrating the location of ridge elements in relation to the checkerboard-like lattice system. Filled squares denote the presence, and white squares denote the absence of ridge elements. Red squares denote clockwise ridge elements, blue squares denote counter-clockwise ridge elements, and purple squares denote corner elements (which do not count toward the number of either clockwise or counter-clockwise elements). (c) Bar plot showing the mean occupancy fraction for ridge elements ($n=10$ from figure B.7). Data presented are averages, and error bars represent \pm one standard deviation. The purple bar shows the total ridge occupancy fraction, which includes all clockwise (red bar), counter-clockwise (blue bar), and corner elements. (d) Plot adapted from Weaver et al.^[6], which illustrates that the combination of a decreasing volume per unit area for the underlying diagonally reinforced square lattice (orange) with an increasing ridge height (green) along the length of the tapered tube, results in a relatively consistent total material volume of silica per unit area throughout the entire skeletal system (black dotted line). For the orange and green data, the solid lines denote averages and the shaded regions denote \pm one standard deviation for $n=10$ specimens.

ent sponge skeletal samples and manually mapped each of the different ridge designs, ultimately constructing a series of planar ridge connectivity diagrams, a representative example of which is shown in figure 3.1(b) (all ten maps are shown in figure B.7). In this surface map, the colored squares represent the ridge locations (the ridge-less unit cells are white), with red squares denoting clockwise ridges, and blue squares denoting counterclockwise ridges (corner elements are denoted in purple). From examination of these different sponge specimens, we identified several common ridge design themes, which include the following (and are consistent with observations from previous studies^[6]):

- The ridges occur at 45-degree angles relative to the long axis of the skeletal tube.
- The ridges populate, on average, every other closed square in the skeletal lattice.
- The ridges intersect at 90-degree angles.
- The ridges never cross each other, however, they may form T-junctions.
- The total number of ridge-filled cells is similar between specimens, as shown by the purple bar in figure 3.1(c), which denotes the mean ridge quantity for ten different sponge specimens (error bars represent +/- one standard deviation).
- The total number of clockwise ridges is similar to that of the total number of counter-clockwise ridges, as denoted by the red and blue bars in figure 3.1(c), which correspond to the mean clockwise and counterclockwise ridge lengths for ten different sponge specimens (error bars represent +/- one standard deviation).

Finally, it is important to note that, on average, the height of the ridges linearly increases from ca. 1 mm to ca. 6 mm from its anchoring point on the seafloor to its apex (illustrated by the green line in figure 3.1(d)).^[6] Despite this increasing ridge height, a relatively constant material volume per unit area has been measured along the length of the tapered skeletal network (illustrated by the dashed black line in figure 3.1(d))^[6], which results from a simultaneous increase in lattice unit cell size and a relatively constant strut thickness, which lead to a corresponding decreasing strut width-to-unit cell width ratio as you ascend the sponge (illustrated by the orange line in figure 3.1(d)).

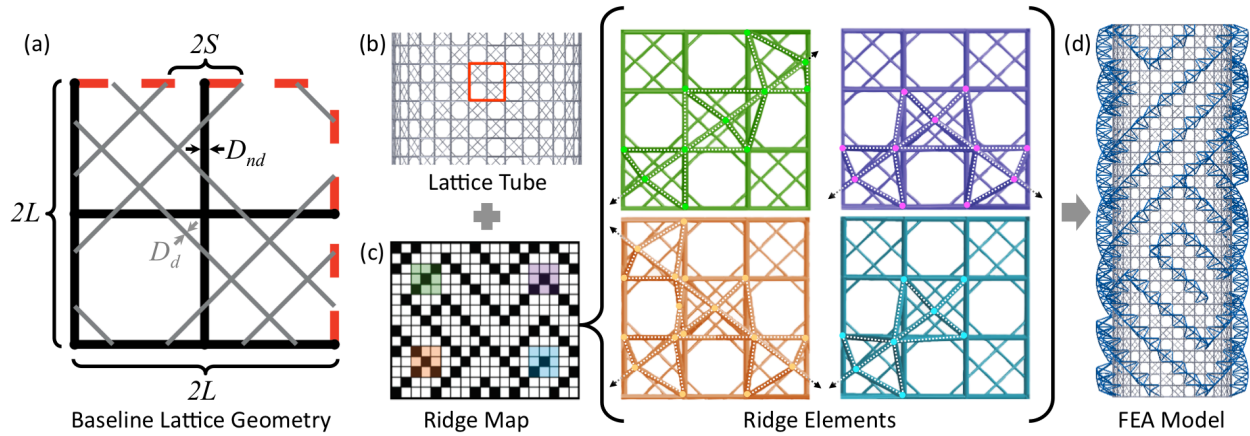


Figure 3.2: Workflow for the generation of sponge structural models. (a) Schematics showing the underlying diagonally reinforced square unit-cell geometry, which was tiled to produce the tubular lattice shown in (b). (c) Schematics showing the different ridge elements used to construct the complete skeletal model. Each component is color-coded in the left map, indicating its location. The dotted lines in each of the four 3D models correspond to the main ridge supporting elements, the brightly colored dots denote nodes of fusion between the struts, and the black arrows denote the direction of ridge elongation. To construct the complete ridge system for each tested sponge geometry (as shown in (d)), each of these four elements could be either translated, rotated, or mirrored (with the exception of the *Bidirectional* design which requires an additional crossing element).

3.4 Model Generation

To construct the 3D models used in both our mechanical and hydrodynamic studies, we subdivided the geometry into two primary components: (1) the hollow cylindrical core, and (2) the external ridge system.

3.4.1 Hollow cylindrical core

Structural analysis. For the structural analyses, we considered only the load-bearing glassy skeletal components of the sponge. To produce this model, we tiled the diagonally reinforced square lattice geometry described in Fernandes et al.^[115] (figure 3.2(a)) to generate a tubular lattice (figure 3.2(b)), which consisted of 32 horizontal struts, and 32 vertical struts in circumference (creating a cylinder with height to radius ratio $H/R \sim 6.2$). The ratio between the strut diameter

and strut separation was $D_{\text{nd}}/L = 0.1$ (where L is the square grid strut separation) to match the average dimensions found in this species^[115] (figure 3.2(a)). Overlaid on this square grid is a system of paired diagonal reinforcing struts (figure 3.2(a)), the periodic spacing of which creates a checkerboard-like open and closed cell structure, where every open cell contains an octagonal aperture. This geometry leads to two independent pairs of crisscrossing diagonal struts, each with a spacing of

$$S = \frac{L}{\sqrt{2} + 2}.$$

In this configuration, the pairs of diagonals are thinner than the non-diagonal struts^[6,115], with a relationship given by^[115]

$$D_{\text{d}} = \frac{D_{\text{nd}}}{2}.$$

Hydrodynamic analysis. For the hydrodynamic analyses, we explored three different geometries for the cylindrical core, all characterized by an external radius R_o , an internal radius $R_i = 0.9R_o$, and a height $H = 6.2R_o$:

- *No Pores*: This design consisted of a featureless smooth cylinder (see figure 3.3 - second column), a geometry that has been widely studied in the field of hydrodynamics, and is known to produce von Kármán vortices.^[120,121]
- *Small Pores*: Inspired by the anatomy of living specimens of *E. aspergillum*, small holes (approximated as octagons) populate locations corresponding to the positions of every open square in the underlying diagonally reinforced skeletal lattice (see figure 3.3 - third column). In this configuration, the effective surface porosity is given by $\varphi_s = 0.06$. For details regarding the geometry and porosity calculations, see figure B.1.
- *Large Pores*: This geometry is very similar to that of the *Small Pores* tube, but with larger diameter holes (see figure 3.3 - third column). The porosity of this design reflects that of only the sponge's skeleton, and the effective surface porosity of this structure is given by $\varphi_s = 0.41$. For the details regarding geometry and porosity calculations, see figure B.1.

To create the small and large pore models, respectively, octagonal openings measuring with side $S_0 = 0.16L$ (figure 3.4(f) and (g)) and $S_0 = 0.4L$ (figure 3.4(h) and (i)) were cut through the cylinder-ridge construct.

3.4.2 External ridge system

For our structural and hydrodynamic analyses, we considered three different diagonal ridge arrangements (figure 3.3)

- *Unidirectional Ridges*: This geometry consists of eight uninterrupted parallel *unidirectional* helical ridges, each of which measures 32 cells in length, and occupy every other filled square cell of the sponge's skeletal lattice (figure 3.3(b)).
- *Bidirectional Ridges*: As with the unidirectional ridge model, this design also incorporates eight helical ridges, each of which measures 32 cells in length. However, for this design, four of the helices are right-handed and four are left-handed (figure 3.3(c)).
- *Sponge Ridges*: Inspired by the external ridge structure of *E. aspergillum*, this geometry is composed of a maze-like combination of right- and left-handed ridges that occupy every other filled square cell of the sponge's skeletal lattice. One example (from the list of ten mapped sponges) is shown in figure 3.3(d). The other nine mapped designs can be found in figure B.7.

It is important to note that for the three different ridge configurations described above, the total ridge lengths are nearly identical. Furthermore, in all our models, we chose the height of the ridges to be $h_r = 1.45L$, which is equivalent to the mean ridge height ($R_r - R_o$ in figure 3.4(c) and (d)) across the length of the sponge.^[6]

Structural analysis. To generate the ridges for our structural models, we first identified the four distinctive design elements shown in figure 3.2(c), which formed the basis of a complete ridge system. These elements are a result of ridge continuations (green schematic), 90 degree turns (purple schematic), T-junctions (orange schematic) and ridge terminations (blue schematic) in the

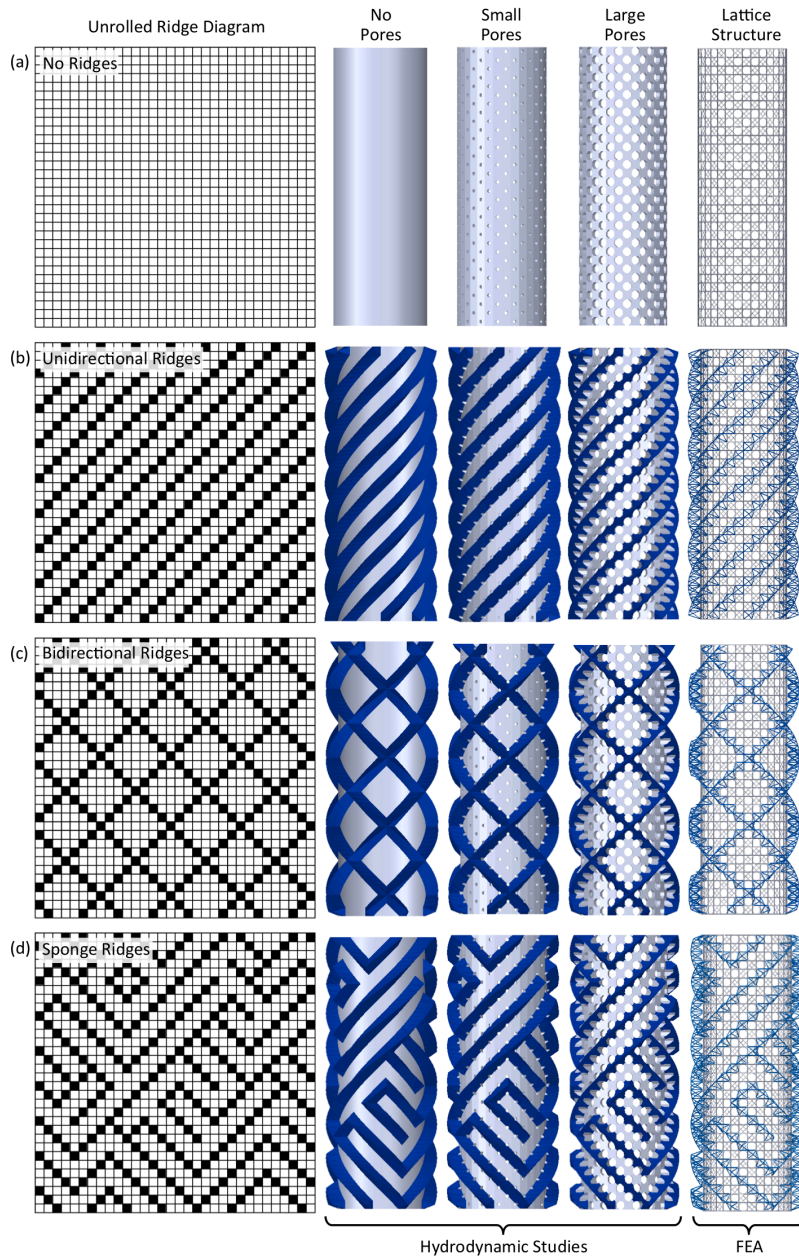


Figure 3.3: Fully constructed skeletal models for structural and hydrodynamic analyses. Schematics showing (a) the baseline cylinder (containing no ridges), (b) the *Unidirectional* ridge design, (c) the *Bidirectional* ridge design, and (d) one representative example of the *Sponge* ridge design. For each ridge geometry, we also considered four variations of the inner tube (left to right): a solid (nonporous) tube, a low-porosity tube (matching the porosity of the living sponge), a high-porosity tube (matching the porosity of only the skeleton), and that of only the load-bearing skeletal elements of a sponge. CFD simulations were conducted on the first three tube geometries (solid, low-porosity, and high-porosity geometries) and FE simulations were conducted on the last geometry (load-bearing skeletal elements).

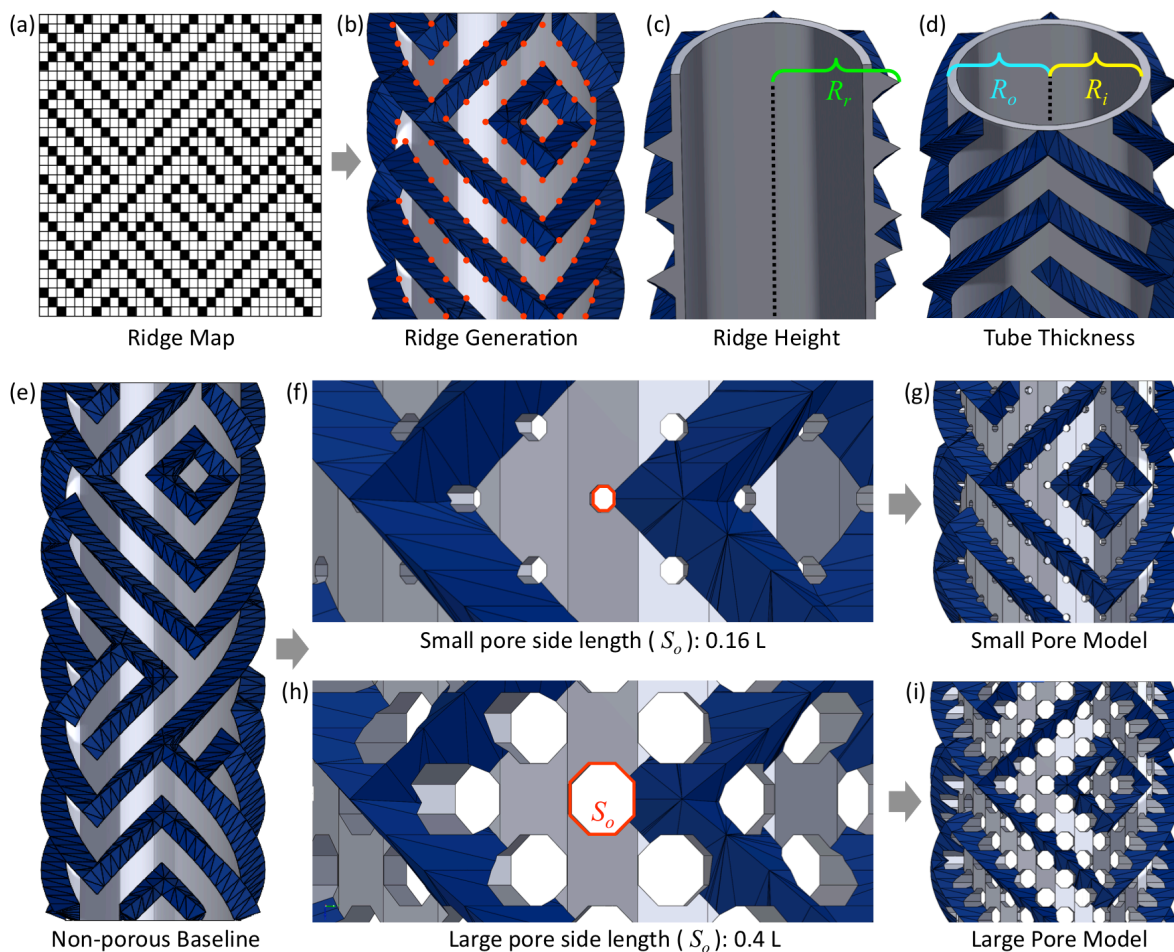


Figure 3.4: Hydrodynamic model generation workflow. (a) Schematics showing one of the ten sponge ridge diagrams that provided a road map for the construction of a complete ridge network (b). The apex of the triangular ridges (blue) cross diagonally through the squares in (a) and their flat sides contact the underlying cylinder (gray) at the geometric centers (denoted by red dots) of the octagonal openings shown in figure 3.2(a). (c) Schematics showing a cross-sectional view of the non-porous cylindrical core (gray) with the labeled radius encompassing the ridge height R_r . (d) Schematics showing the cylinder thickness parameters, with R_o and R_i denoting the outer and inner radii, respectively. For (c) and (d), the vertical black dotted lines denote the model's neutral axis. (e) Schematics showing the complete non-porous baseline ridge geometry, which was generated from the map shown in (a). High (f) and low (g) magnification views, showing the geometries of the octagonal holes (red) for the small pores containing a side length of $S_o \approx 0.16L$, which approximates the porosity of a living sponge. High (h) and low (i) magnification views, showing the geometries of the octagonal holes (red) for the large pores containing a side length of $S_o \approx 0.4L$, which approximates the porosity of only the sponge's glassy skeletal system.

sponge ridge system. Utilizing these elements and their possible rotations, we generated all of the different ridge-containing models. For all of the struts composing the ridge structure, the diameter matched that of the non-diagonals, namely, $D_{\text{rg}} = D_{\text{nd}}$, where D_{rg} is the ridge strut diameter and D_{nd} is the non-diagonal strut diameter.

Hydrodynamic analysis. To generate the ridges for our hydrodynamic models (which were modeled after those found in living examples of *E. aspergillum*), we began with a planar ridge diagram (figure 3.4(a)), which was used as a road map to construct a series of triangular surface ridges (figure 3.4(b)) on an extruded 32-sided polygon (which approximated the cylindrical geometry of the sponge). The flat-sided ridges were designed such that their apex ran diagonally through the squares in the planar ridge map, and contacted the cylinder at a location that corresponded to the geometric centers of each of the octagonal openings shown in figure 3.4(a) (and denoted by the red dots in figure 3.4(b)).

3.5 Structural Analyses

3.5.1 Methods

In an effort to understand how the ridges affected the sponge’s structural performance, we conducted Finite Element (FE) simulations using ABAQUS/Standard (Dassault Systèmes SE). For these analyses, the geometries were constructed using Timoshenko beam elements (ABAQUS element type B22) with circular cross-sections and the material’s response was captured using a linear elastic material model with Young’s modulus E_{mat} . In our simulations, we considered the ten different sponge ridge designs shown in figure B.7 and compared their response to the *Unidirectional*

and *Bidirectional* models. We also considered a model without ridges, where the ridge material was instead allocated to the cylindrical beams of the underlying diagonally reinforced square lattice (we refer to this model as the *Reallocated Ridge Mass* model).

For each design, we assumed that the cylindrical sponge structure was fully constrained at its base (i.e. $u_x = u_y = u_z = 0$), and performed two different analyses: (1), a linear static analysis to extract the stiffness, and (2), a buckling analysis (*BUCKLE step in ABAQUS) to obtain the critical buckling force. In the simulations, we considered four loading cases (illustrated in figure 3.5(a))

- *Compression*: For this case, we applied a vertical displacement parallel to the z-axis ($\delta_{appl} = \delta_z$) to all the nodes of the top ring.
- *Torsion*: For this case, we applied a tangential displacement ($\delta_{appl} = \delta_\theta = \theta_{appl}R$) to all the nodes of the top ring.
- *Bending*: For this case, we applied a displacement in the x-y plane ($\delta_{appl} = \sqrt{\delta_x^2 + \delta_y^2}$) to all the nodes of the top ring. Note that we systematically varied δ_x and δ_y to survey the bending behavior in different directions. Specifically, we considered 8 equally spaced directions for each structure.
- *Pressure*: For this case, we apply a radial displacement ($\delta_{appl} = \delta_R$) to all nodes belonging to the cylindrical core of the models.

To implement these boundary conditions for *Compression*, *Torsion*, and *Bending*, we constrained the degrees of freedom of the nodes of the top ring to a virtual node using equation constraints. Similarly, for the loading case *Pressure*, we tied the degrees of freedom of all nodes belonging to the cylindrical core to a virtual node using equation constraints. For all loading cases, we then applied δ_{appl} to the virtual nodes and extracted the resulting reaction force RF .

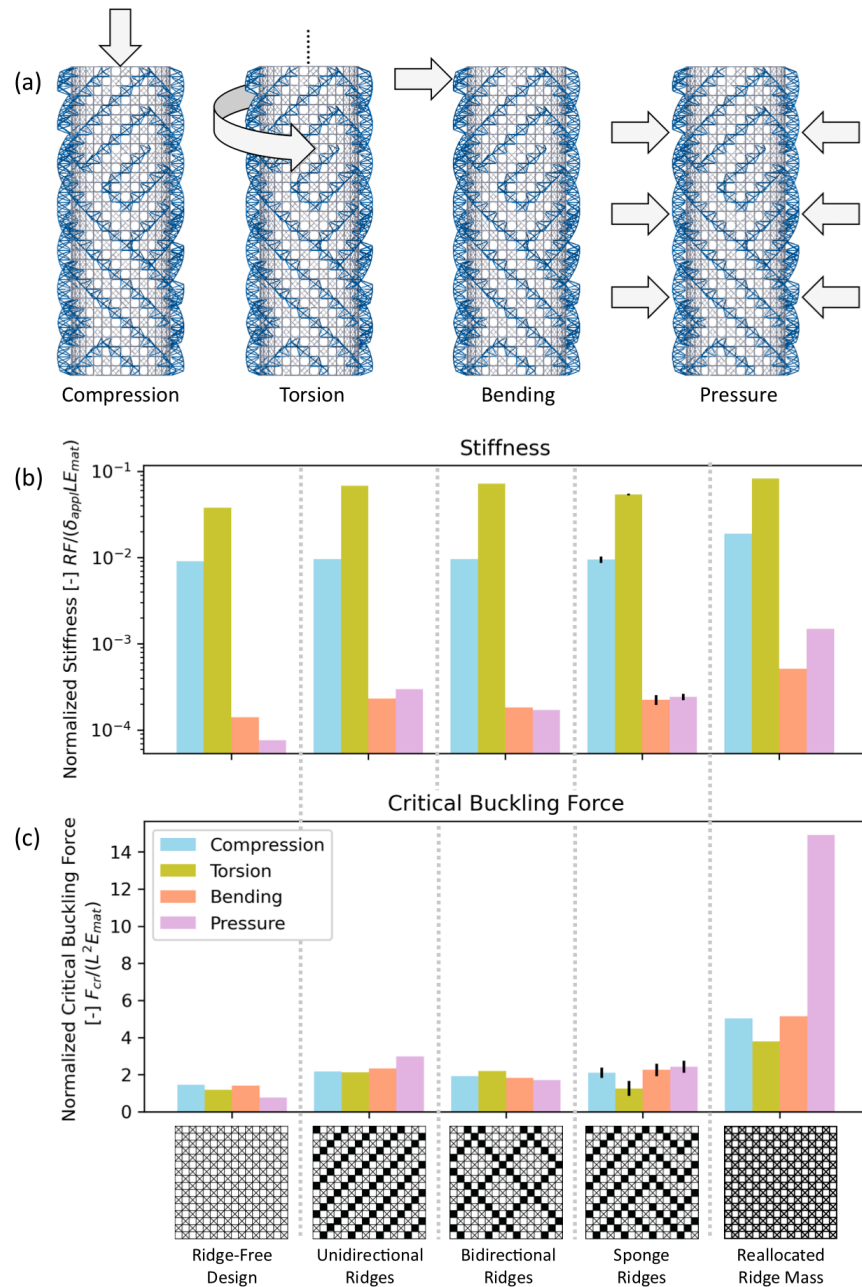


Figure 3.5: Structural Analysis. (a) Schematics illustrating boundary conditions considered in the FE simulations. For all considered loading conditions, the displacement at the bottom was held fixed, namely $u_x = u_y = u_z = 0$, and a displacement δ_{appl} (indicated with arrows) was applied. (b)-(c) Bar plots showing normalized stiffness $RF/(\delta_{appl}LE_{mat})$ and normalized critical buckling force $F_{cr}/(L^2E_{mat})$ with different colors corresponding to each loading condition. The models considered were the ten mapped *Sponge* geometries (see figure B.7), the *Unidirectional* and *Bidirectional* geometries, the *Ridge-Free* design, and the *Reallocated Ridge Mass* design, from left to right respectively. For the the *Reallocated Ridge Mass* design, we employed the *Ridge-Free* design, but reallocated the volume from the ridges into the cylinder elements, thus making each element thicker and more robust.

3.5.2 Results

In figure 3.5(b) and (c) we report the numerically predicted stiffness and critical buckling load for all considered models and loading cases. We find that the addition of ridges increase the overall stiffness of the cylindrical structure for loading conditions *Bending* and *Pressure* (figure 3.5(b)) and improve the buckling performance for all loading conditions on average by ca. 2-fold over the ridge-free example (figure 3.5(c)). However, if we compare the performance between the different ridge-containing geometries, we see that the stiffness values differ negligibly between the different ridge designs. In contrast, if the ridge material volume was instead allocated away from the ridge system and into the main cylindrical truss frame, the resulting structure, on average, measurably outperforms the other designs for most loading conditions in terms of both stiffness and buckling force. This result is not unexpected, since in this scenario, more material is allocated to the truss members aligned parallel to the loading direction.

These results demonstrate that the unusual maze-like ridge pattern found in *E. aspergillum* does not likely add any significant additional mechanical benefit (with regards to either stiffness or critical buckling force) compared to the other investigated ridge geometries, which prompted additional studies into its potential hydrodynamic functions (see section 3.6, below). Further, the observation that reallocating the ridge material into the underlying diagonally reinforced skeletal lattice, resulted in a significant enhancement in the structure's mechanical performance may be functionally relevant to the sponge's skeletal anatomy. As shown in figure 3.1(d), the sponge's material volume per unit area remains relatively constant along the length of the tapered skeletal tube, which is achieved due to an increase in ridge height (and volume), from the base of the sponge to its apex, and a corresponding loss in volumetric skeletal density of the underlying diagonally

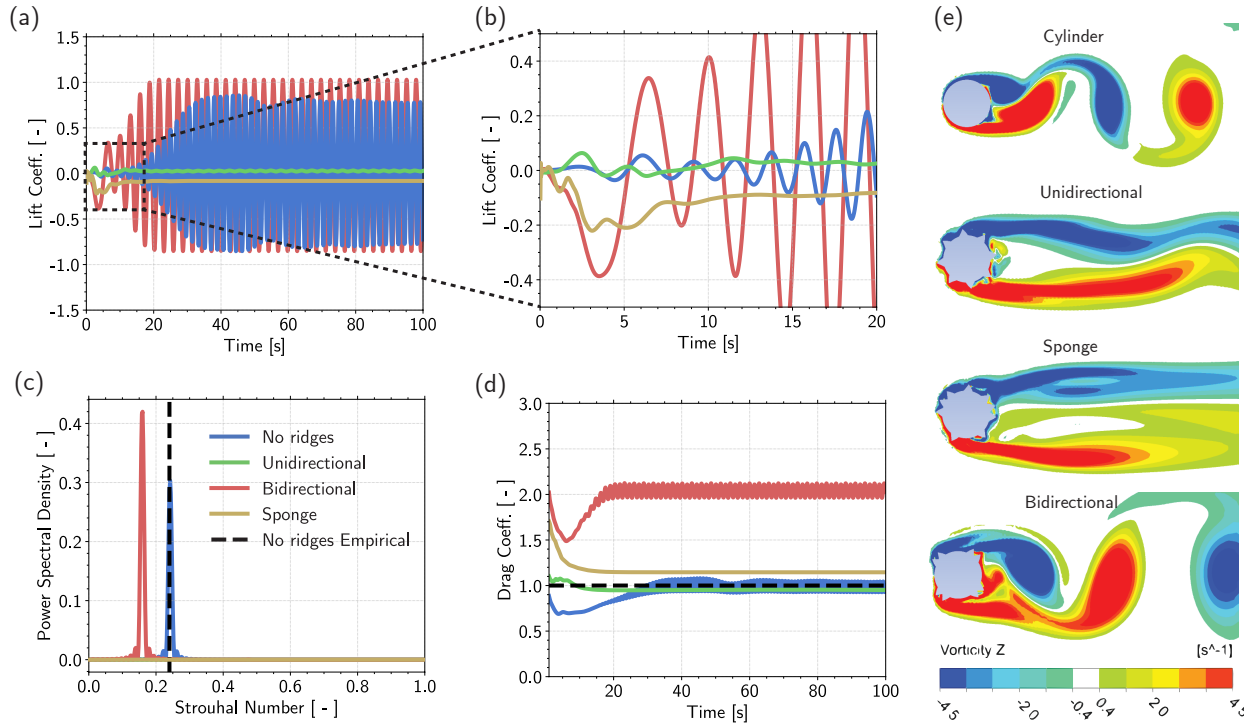


Figure 3.6: Hydrodynamic results for non-porous cylindrical geometries. (a) Plot showing transient lift coefficient C_l for the different non-porous geometries. (b) Magnified view of transient lift coefficients, showing the initial shedding behavior for different non-porous geometries. (c) Plot showing power spectral density (PSD) as a function of Strouhal number for different ridge-containing geometries. The vertical dashed black line shows the empirical Strouhal number for a smooth cylinder using a $Re = 5500$ flow regime. Note that the last 20 seconds of the transient data (when the flow reaches a periodic state) were used to compute the PSD. (d) Plot showing transient drag coefficient C_d for the different ridge-containing geometries. The horizontal black dashed line corresponds to empirical drag coefficient data for a smooth cylinder using $Re = 5500$ flow regime. (e) Vorticity fields illustrating shedding for the different non-porous geometries.

reinforced square lattice (which results from an increase in vertical and horizontal strut spacing). As such, the mechanically most robust portion of the composite skeleton coincides with its thickened and ridgeless connection point to the flexible holdfast apparatus, which secures the sponges into the soft sediments of the sea floor. Based on our results, this transition in the skeletal anatomy from the rigid skeleton to its flexible holdfast apparatus, is likely a point of highest mechanical stresses and a potential location of skeletal failure, an observation consistent with our simulated buckling locations shown in figure B.8.

3.6 Hydrodynamic analyses

To explore the potential hydrodynamic benefits of the unique maze-like collection of bidirectional helical ridges located on the skeletal tube of *E. aspergillum*, we developed a Computational Fluid Dynamics (CFD) framework, and compared their performance to alternative equal-length ridge geometries that are commonly employed in modern engineering applications for vortex suppression and drag reduction^[116,117,119].

Since the natural habitat of the genus *Euplectella* can vary widely (occurring in low and temperate latitudes at depths ranging from 36 to 5,050 meters^[122]), these sponges are likely to experience a wide range of flow patterns and velocities that must be considered. As such, in our simulations, we considered non-dimensional Reynolds number $Re \in [5000, 60000]$, where Re was defined as

$$Re = \frac{uL}{\nu},$$

u being the flow speed, L the characteristic length scale, and ν the fluid kinematic viscosity. It

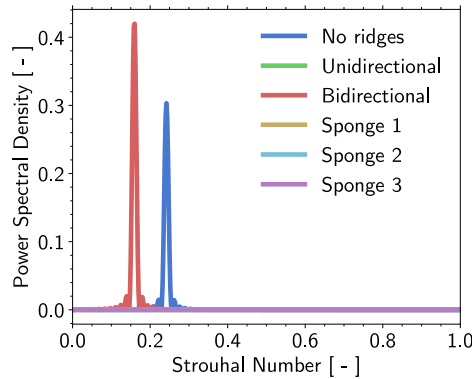


Figure 3.7: PSD for additional sponge geometries. PSD plot comparing the different considered structures to additional sponge ridge designs obtained from real sponge samples (see figure B.7). Results are presented for $Re = 5,500$.

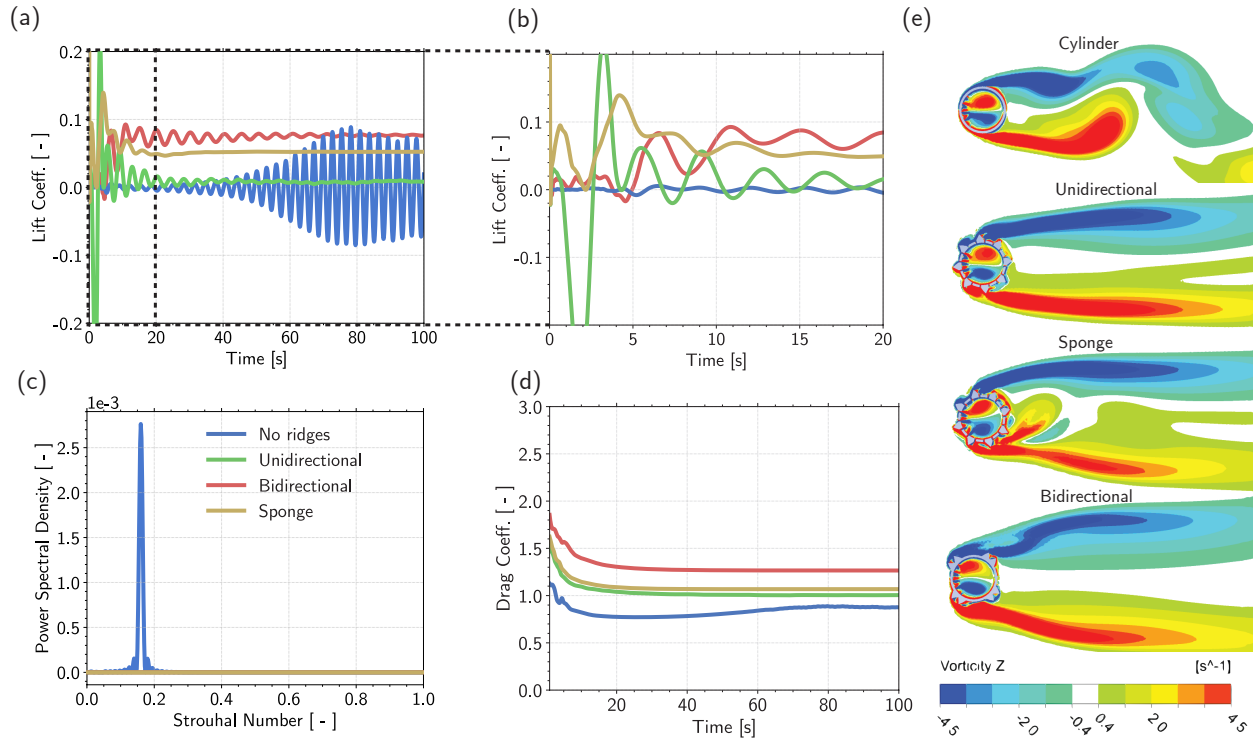


Figure 3.8: Hydrodynamic results for cylindrical geometries exhibiting biologically relevant (small) porosities inspired by the anatomy of living specimens. (a) Plot showing transient lift coefficient C_l for the different porous geometries. (b) Magnified view of transient lift coefficients, showing the initial shedding behavior for different non-porous geometries. (c) Plot showing power spectral density (PSD) as a function of Strouhal number for different ridge-containing geometries. Note that the last 20 seconds of the transient data (when the flow reaches a periodic state) were used to compute the PSD. (d) Plot showing transient drag coefficient C_d for the different ridge-containing geometries. (e) Vorticity fields illustrating shedding for the different different non-porous geometries.

is important to note that the length scale L for all computations do not include the dimensions of the ridges (i.e. cylinder outer diameter only), and the resulting Re range encompasses a large flow regime, where vortex shedding behind cylindrical structures is known to occur.

3.6.1 Methods

To model fluid flow around the different cylindrical geometries, we used the CFD package *ANSYS CFX, Release 18*, which employs a hybrid finite-volume/finite-element approach to discretizing the Navier Stokes equations governing fluid flow. The systems of equations were solved using

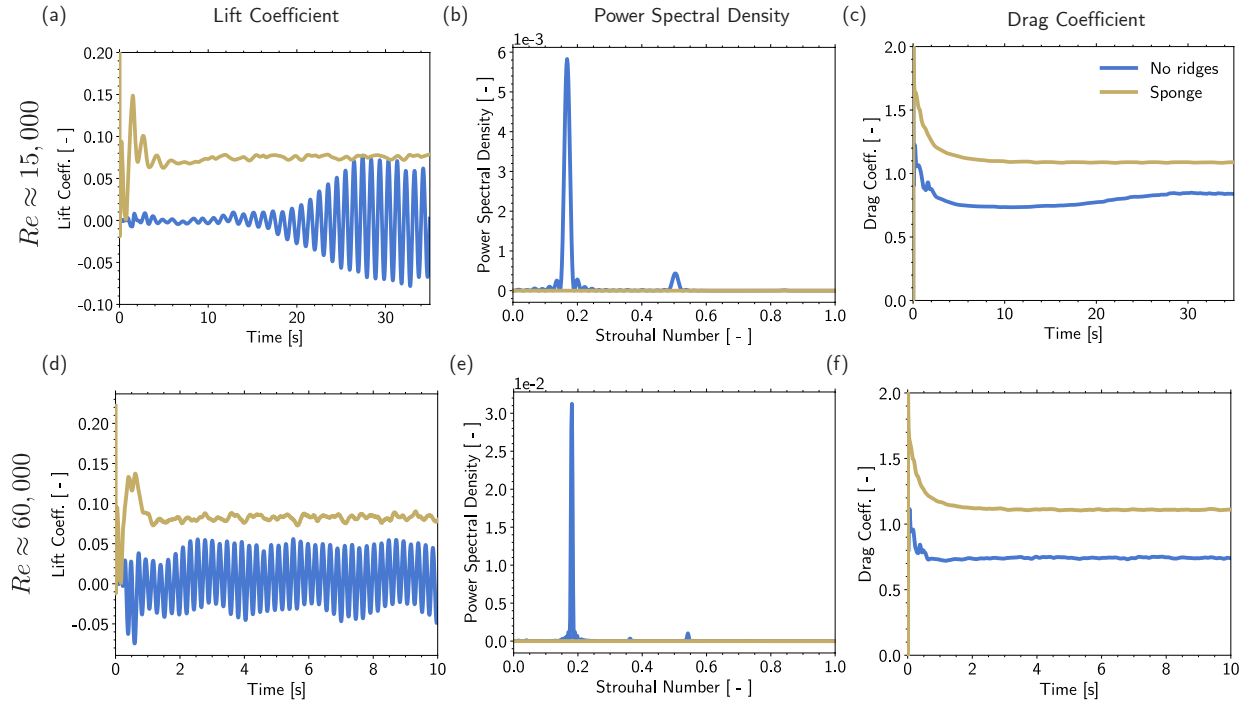


Figure 3.9: Hydrodynamics results for $Re = 15,000$ and $Re = 60,000$ low-porosity cylinder baseline and sponge. (a) Plot showing transient lift coefficient C_L as a function of time at $Re = 15,000$. (b) PSD plot showing density with frequency converted to Strouhal number. Note that the last 10 seconds of the transient data were used to compute the PSD at $Re = 15,000$. (c) Plot showing transient drag coefficient C_D as a function of time at $Re = 15,000$. (d) Plot showing transient lift coefficient C_L as a function of time at $Re = 60,000$. (e) PSD plot showing density with frequency converted to Strouhal number at $Re = 60,000$. Note that the last 5 seconds of the transient data were used to compute the PSD. (f) Plot showing transient drag coefficient C_D as a function of time at $Re = 60,000$.

an unsteady fully-implicit, fully-coupled multi-grid second-order backward Euler solver in the laboratory frame of reference. The Shear Stress Transport turbulence model^[123], which combines the $k - \omega$ model near the wall and the $k - \varepsilon$ model away from the wall, was used throughout this study. This choice of turbulence model ensured accurate prediction of onset and amount of flow separation under adverse pressure gradient conditions. This approach also allowed the model to handle transitions of the flow from laminar to turbulent, accurately refining the flow profile around the complex geometry of the ridges. It is important to note that in our CFD simulations, we did not account for interactions between the flow and the mechanical deformation of the sponge (i.e. we

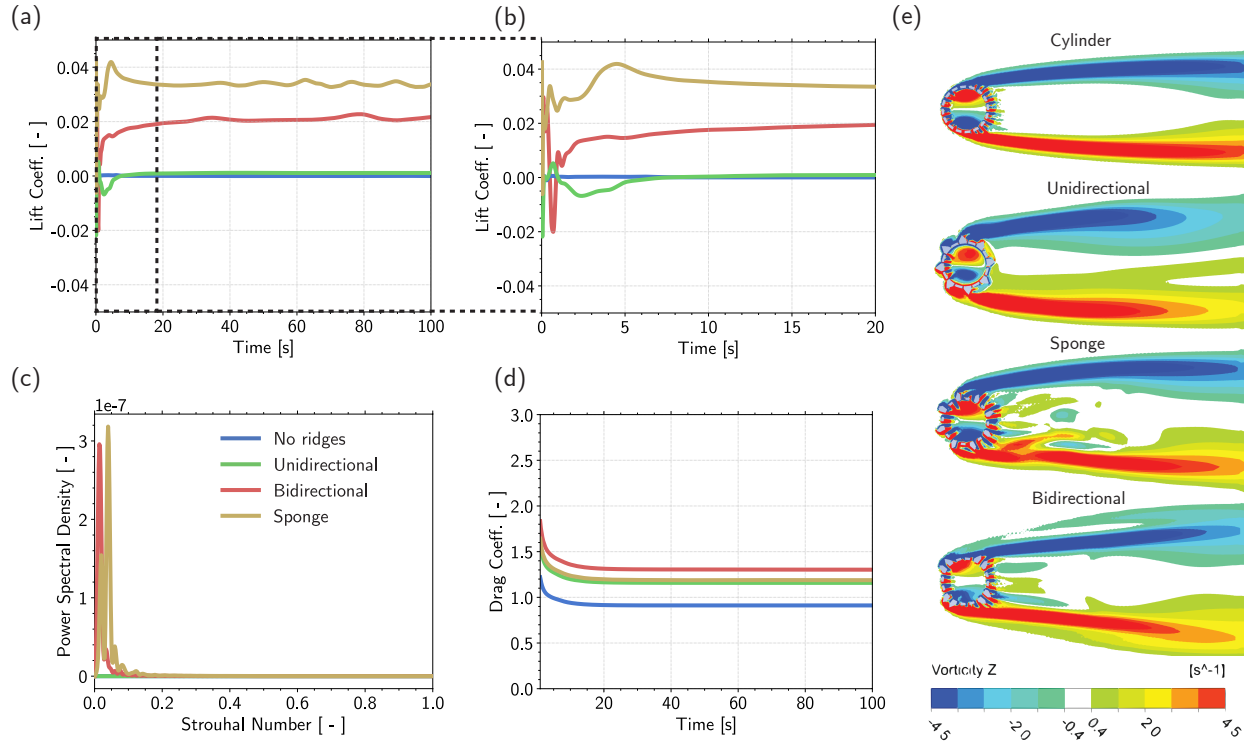


Figure 3.10: Hydrodynamic results for cylindrical geometries exhibiting biologically relevant (large) porosities reflecting the skeletal anatomy of specimens. (a) Plot showing transient lift coefficient C_l for the different porous geometries. (b) Magnified view of transient lift coefficients, showing the initial shedding behavior for different non-porous geometries. (c) Plot showing power spectral density (PSD) as a function of Strouhal number for different ridge-containing geometries. Note that the last 20 seconds of the transient data (when the flow reaches a periodic state) were used to compute the PSD. (d) Plot showing transient drag coefficient C_d for the different ridge-containing geometries. (e) Vorticity fields illustrating shedding for the different different non-porous geometries.

did not perform fluid-structure interaction simulations).

In the hydrodynamic simulations, we focused on comparing one representative sponge ridge design (from the ten mapped), specifically *Sponge 1* shown in figure 3.3(c), to the *Unidirectional* and *Bidirectional* configurations for cylindrical cores with both small and large pores. All models with a porous cylindrical core were placed at the bottom of a rectangular prism-shaped fluid domain, with size $40R_o \times 80R_o \times 20H$, to which symmetry condition on the top face and a slip condition on the bottom face were applied (see figure B.4 for details). To facilitate direct comparisons to previously published results^[8,9], the models with a non-porous cylindrical core were placed in a fluid domain

with size $40R_o \times 80R_o \times H$, to which we applied periodic boundary conditions at the top-bottom faces (see figure B.3 for details). For all analyses, we then imposed a uniform flow velocity perpendicular to one of the side walls, zero pressure to the opposite face, and slip conditions on the remaining two side walls. Finally, we imposed no-slip conditions on the boundaries of the cylindrical structure. For each model, we conducted simulations to calculate

- *Lift coefficient*: for each timestep, we obtained the coefficient of lift as

$$C_L = \frac{2F_L}{\rho Au^2},$$

where F_L was obtained by integrating the perpendicular-to-flow component of the pressure acting on all external faces of the cylindrical structure, ρ was the fluid density, A was the surface area of all external faces of the cylindrical structure, and u was the flow velocity.

- *Shedding frequency*: Once C_L was computed as a time series, we performed a Power Spectral Density (PSD) analysis on the C_L data to obtain a power spectrum of frequencies for the lift force. To obtain the PSD for the time series, we computed the Fourier decomposition of the signal and analyzed the relative magnitudes of each of the coefficients. In this analysis, the shedding frequency is identified as the highest power frequency, if shedding exists. Note that in order to ensure that the vortex shedding results were reproducible for perturbations within the sponge ridge design space (in addition to *Sponge 1*), we also performed a the PSD analysis on two additional sponge ridge configurations (*Sponges 2* and *3* in figure B.8).
- *Drag coefficient*: To measure the drag on the structure, we computed the coefficient of drag for each time-step, which was defined as

$$C_D = \frac{2F_D}{\rho Au^2},$$

where F_D was obtained by integrating the parallel-to-flow component of the pressure acting on all external faces of the cylindrical structure. Note that in order to validate our simulations, we compared our results for a cylinder without pores and without ridges, to the drag coefficient data obtained from Blevins^[9](See figure B.5(b) for more information).

- *Flow profile through the openings in the cylindrical core*: To investigate the potential role of the ridges as a mechanism for increasing/redirecting fluid flow through the sponge for feeding/gas exchange purposes, we created a closed cylindrical boundary matching the geometry of the sponge's interior and computed the time-averaged flow profile through the openings

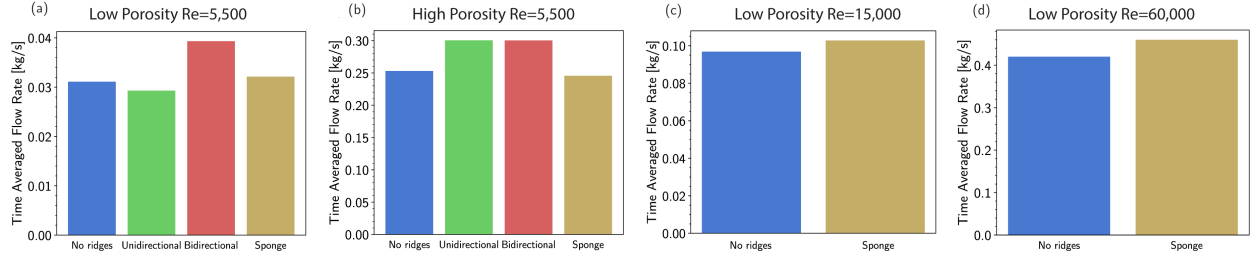


Figure 3.11: Quantification of flow rate through the different investigated geometries. (a) Bar plot showing time-averaged flow rate through the wall of the low-porosity tubular structures for $Re = 5,500$. (b) Bar plot showing time-averaged flow rate through the wall of the high-porosity tubular structure for $Re = 5,500$. (c) Bar plot showing time-averaged flow rate through the wall of the low-porosity tubular structure for $Re = 15,000$. (d) Bar plot showing time-averaged flow rate through the wall of the low-porosity tubular structure for $Re = 60,000$.

in the sponge's body wall by averaging the flow over three cycles of shedding. Using this flow profile, we integrated the absolute value of the flow rate over the area of the cylindrical boundary defined by

$$V = \int_A \frac{1}{2} \left| \frac{\dot{V}}{A} \right| dA.$$

Note, that because of fluid incompressibility and conservation of mass, the volume flow in the boundary V_{in} must equal the volume out V_{out} leading to a division by 2 to obtain total volume exchanged.

To balance model accuracy and computational efficiency, in all our simulations we refined the mesh near the region of interest (in the sponge's vicinity) and kept the down-field meshing course. For each of the models, we produced a mesh consisting of more than 2 million elements, an illustration of which can be found in figure B.6.

3.6.2 Results

In figure 3.6, figure 3.8, and figure 3.10 we report the lift coefficient, shedding frequency, and drag coefficient (together with numerical snapshots that show the vorticity fields) at $Re = 5500$ for designs comprising a hollow cylindrical core with no pores, small pores ($\varphi_s \approx 0.06$), and large pores ($\varphi_s \approx 0.41$), respectively. For all three cases, we considered three different ridge geometries

(*Unidirectional*, *Bidirectional*, and *Sponge* configurations) and compared their performance to a ridge-free control.

As shown in figure 3.6(a) and (b) we find that for the geometries with non-porous cylindrical cores and either *Bidirectional* ridges or no ridges, there exists large cyclic lift forcing acting on the structures. In contrast, we see that for the *Sponge* and *Unidirectional* ridge designs, the cyclic forcing is quickly suppressed. The PSD performed on these lift data reveals that the *Sponge* and *Unidirectional* ridge designs are effective at suppressing vortex shedding forcing on the cylindrical structure, as evident by the lack of a localized peak in figure 3.6(c). In contrast, we observe vortex shedding behind the cylinder for both the no ridge and *Bidirectional* ridge configurations, with the vortices actually amplified by the bidirectional ridge design (as indicated by a higher peak in the PSD in figure 3.6(c)). It is also important to note that while the *Unidirectional* ridge design shifts the shedding downstream, the *Sponge* ridge design completely suppresses the vortex shedding behind its cylindrical structure (see snapshots in figure 3.6(e)), demonstrating a more efficient vortex suppression mechanism. While the *Sponge* ridge design outperforms the *Unidirectional* ridge design in vortex suppression, it does, however, lead to a slightly increased drag force on the structure (figure 3.6(d)).

To validate our results, we first compared both the location of the peak in the PSD and the drag coefficient obtained for a non-porous cylindrical core without ridges to existing empirical data for a cylinder in a uniform 2D flow at $Re = 5500$ (black dashed lines in figure 3.6(c) and (d) - for more information, see figure B.5).^[8,9] The good agreement between these two data sets confirmed the suitability of our numerical approach. To further validate the effects of vortex shedding observed for our selected sponge ridge geometry with a non-porous cylindrical core, in figure 3.7 we analyzed the PSD for two additional *Sponge* ridge designs (*Sponge 2* and *Sponge 3* from figure B.7),

in addition to the original sponge design (*Sponge 1*), the *Unidirectional*, the *Bidirectional*, and the cylindrical baseline geometries. In this plot, we observe that all three of the sponge-inspired designs can efficiently suppress vortex shedding compared to the other more symmetrical ridge geometries. These results thus demonstrate that the observations presented in figure 3.6 are likely not specific to the unique sponge ridge geometry investigated.

In figure 3.8, we report results for designs comprising a hollow cylinder with small pores. For this case, we find that large cyclic lift forcing acting on the structure exists only for the model without ridges (figure 3.8(a)). We also note that for the *Bidirectional* and *Sponge* ridge geometries, the lift coefficient does not average to zero, since the ridges break the flow symmetry and bias the lift coefficient to a particular direction (see figure B.10 for more information). By taking the data from the lift coefficient and computing the PSD, we observe that for this level of biologically relevant porosity, prominent vortex shedding still exists behind the cylindrical baseline geometry (figure 3.8(c)), while all three models with ridges are capable of suppressing vortex shedding. As such, these results demonstrate that for $\phi_s \approx 0.06$, the introduction of helical ridges is sufficient to suppress vortex shedding regardless of the specific ridge arrangement. However, although all three ridge geometries suppress the vortices over the long term, it is important to note that some geometries provide a faster dissipation mechanism than others. As shown in figure 3.8(b), the *Unidirectional* and *Bidirectional* ridge designs exhibit cyclical lift forcing as soon as flow is initiated, indicating an early onset of vortex shedding, and whose amplitude is partially dissipated over time. The *Sponge* ridge design, in contrast, transitions much earlier to a steady flow profile with no indication of cyclical lift forcing. Such rapid suppression of vortex shedding is of biological relevance to the sponge, since its local environment can be prone to fluctuations in flow velocity depending on the depth at which it occurs. Finally, the results shown in figure 3.8(d) demonstrate that the

choice of ridge design has also implications on the drag imposed on the cylindrical structure, with the *Bidirectional* design increasing the drag substantially compared to the other ridges geometries.

While the hydrodynamic results reported so far are for $Re = 5500$ (a value relevant to the natural habitat of the sponge), in figure 3.9, we investigated the effect of other Reynolds numbers on these observed behaviors. Specifically, we considered $Re = 15000$ and $Re = 60000$ and, due to the computational complexity of these simulations, compare the hydrodynamic performance of a cylindrical tube with small pores and sponge ridge design to that of a cylindrical tube with small pores and no ridges. We find that for both considered Reynolds numbers, the trends observed in figure 3.8 are unchanged for lift coefficients, shedding frequencies, and drag coefficients.

Finally, in figure 3.10, we report the hydrodynamic results for models with a large surface porosity ($\varphi_s \approx 0.42$), approaching that of a cleaned (bare) sponge skeleton. The results show two key trends. First, we find that at this level of porosity, the existence of von Kármán vortices is not prominent for any of the models, as indicated by the lack of cyclic lift forcing acting on the structures shown in figure 3.10(a) and (b). These results therefore suggest that the introduction of ridges is unnecessary for this level of porosity and that there exists a transition in the flow for surface porosities between $\varphi_s \approx 0.06$ and $\varphi_s \approx 0.42$. Second, the results shown in figure 3.10(c) also demonstrate that for large surface porosities, the drag coefficient remains dependent on the ridge arrangements, and that the dependency is similar to that observed in figure 3.8(d) for $\varphi_s \approx 0.06$.

Beyond the vortex suppression and drag reduction properties of the sponge's external ridges, we also investigated their potential role as a mechanism for increasing/redirecting fluid flow through the sponge for feeding/gas exchange purposes. Towards this end, in figure 3.11(a) and (b), we report the time averaged flow rate over the area of the cylindrical core (defined as in section 3.6.1) at $Re = 5500$ for all considered different geometries with a cylindrical core with both small and large

pores, respectively. These results demonstrate that the flow through the core of the cylinder for the *Sponge* design is almost identical to that of the model without ridges, whereas the *Unidirectional* or *Bidirectional* ridges lead to a slight increase. Similar trends are also observed for $Re = 15,000$ (figure 3.11(c)) and $Re = 60,000$ figure 3.11(d) in the case of small porosity, suggesting that the presence of the *Sponge* ridge design does not offer significant added mass flow through the walls of the main cylinder across a wide range of flow regimes.

3.7 Conclusion

To summarize, using a combination of finite element simulations and computational fluid mechanics, in this study we explored the potential multi-functionality of the complex network of external maze-like ridges found in the skeletal system of the marine sponge, *Euplectella aspergillum*. Using this integrated approach, we demonstrate that this complex ridge system offers the sponge an efficient mechanism for rapidly suppressing von Kármán vortex shedding and reducing lift forcing oscillations (which may be essential for keeping the sponge anchored into the soft sediments of the sea floor), while at the same time, retaining its skeleton's mechanical performance. Beyond their ability to suppress vortex-induced vibrations, which could weaken the attachment point between the sponge's holdfast apparatus and its surrounding substrate, the ridges also likely play a critical role in preventing substrate-associated turbulence and subsequent sediment excavation (see [Video 1](#)), as has been demonstrated for other bottom-anchored cylindrical geometries under flow^[124,125]. The prevention of sediment transport from the down-stream side of the sponge is likely of critical importance to the sponge's survival, since excavation near its holdfast apparatus would also compromise its ability to remain anchored into the soft sediments of the sea floor.

To explore the additional benefits of its maze-like organization, we also compared the sponge ridge geometry to helical strake-based vortex shedding suppression systems commonly employed for above ground (e.g. antennas, and smokestacks) and underwater (support beams, vertical pipelines) high aspect ratio cylindrical structures. From these studies, we find that the sponge's ridge design can completely suppress vortex shedding, a behavior which differs from that of more symmetrical helical strake configurations, which either delay shedding downstream (*Unidirectional* ridge design) or amplifies the shedding magnitude (*Bidirectional* ridge design). Further, we demonstrate that the *Sponge* ridge design continues to effectively suppress vortex shedding across a wide range of flow regimes.

While the findings of this study provide new insight into the multi-functionality (mechanical and hydrodynamic) of the complex external ridges in the skeleton of *E. aspergillum*, it is important to note that the flow regimes considered in this study, namely $Re \in [5500, 60000]$, are also relevant for many man-made cylindrical structures including smokestacks, antennas, submerged piping, and offshore floating platforms. As such, the geometric features identified by this study could be directly utilized in engineering applications where effective dissipation of vortex shedding is necessary, and where vortex-induced vibrations are to be avoided.

4

Surface Texture Modulation via Buckling in Porous Inclined Mechanical Metamaterials

BY: MATHEUS C. FERNANDES, SAURABH MHATRE, ANTONIO E. FORTE, BING ZHAO, OLGA MESA,
JAMES C. WEAVER, MARTIN BECHTHOLD, KATIA BERTOLDI. UNDER REVIEW IN *ADVANCED MATERIALS*,
SUBMITTED APRIL 2021.

4.1 Abstract

Porous materials with well-defined periodicity are commonly encountered in biological and synthetic structures and exhibit a wide range of behaviors, ranging from negative Poisson's ratios, to high energy absorption and acoustic damping. Recently, the response of these systems has been shown to be enhanced by mechanical instabilities that lead to sudden and reversible geometric transformations. Although buckling induces planar transformations in most of 2D porous metamaterials, here we describe the emergence of 3D morphologies triggered by mechanical instabilities in an elastomeric block with tilted cylindrical holes. As a proof of concept, we demonstrate that these structures can be leveraged to tune surface properties including friction and light reflection, thus providing a new experimental platform for investigating deformation-dependent dynamics for tribological and optical applications.

4.2 Introduction

Recently, instabilities have been recognized as a feature to be harnessed rather than avoided^[126]. For example, mechanical metamaterials can be designed to trigger instabilities upon loading, which can lead to dramatic changes in geometry and create functionality^[39,127,128]. Among numerous designs, one of the simplest is a block of elastomer with a square array of cylindrical holes^[81,129,130]. When this structure is compressed in the plane perpendicular to the long axis of the holes, the beam-like ligaments separating them buckle cooperatively. Such instabilities lead to a sudden transformation of the circular holes into mutually orthogonal ellipses. This reversible morphological change has been harnessed to realize structures with unusual mechanical properties, such as

negative Poisson's ratio^[82] and negative swelling ratio^[131], which can function as phononic and photonic switches^[107,132–135], color displays^[135], and soft robots capable of grasping and walking^[71].

While the geometric transformations induced by buckling in 2D porous metamaterials are typically planar, buckling can also trigger the formation of out-of-plane 3D patterns. For example, a bilayer system comprising a thin elastic film covering a pre-strained soft substrate can undergo a buckling instability, leading to the formation of complex wrinkle patterns^[136,137]. These wrinkles have been investigated for applications ranging from stretchable electronics^[138,139] and diffraction gratings^[137,140], to reversibly adhesive pads^[141] and tunable flow control in microfluidic devices^[142]. Beyond these bilayer systems, mechanical instabilities in kirigami sheets can also result in out-of-plane deformations that have been exploited to realize morphable structures^[91,143–145] or the skin of snake-inspired crawling actuators^[146].

Here, inspired by a tilted cuboid structure that can fold into a 3D configuration^[147], we show that buckling generates complex 3D morphologies in a new porous metamaterial comprising a square array of tilted cylindrical holes within an elastomeric matrix. We demonstrate that such buckling-induced 3D deformations can be harnessed to actively control surface properties such as reflectance and friction, providing new opportunities for the production of tunable light-diffusion devices and crawling robots. Finally, we show that this concept can be extended to different periodic arrangements of tilted cylindrical holes, thus providing a new platform to control surface morphology in flexible structures, along with innovative design rules for the production of smart surfaces, soft robots, and active facades for architectural applications.

In this study, we investigate a metamaterial conceptually obtained from slicing a block of elastomer, containing a square array of cylindrical holes aligned along the z -axis, at an angle θ with re-

spect to the xy -plane (figure 4.1(a)). The holes in the gray starting block have a radius $R_h = 5.83$ mm and center-to-center distance d_h , chosen so that the initial porosity is $\varphi_0 = \pi R_h^2 / d_h^2 = 0.59$, which provides the structure a large enough hinge thickness to balance the structure's stiffness and out-of-plane displacement. The resulting metamaterial has an out-of-plane thickness $T = 23.32$ mm and elliptical holes on its top and bottom faces (figure 4.1(a)) with major and minor axis of length $R_h / \cos \theta$ and R_h , respectively.

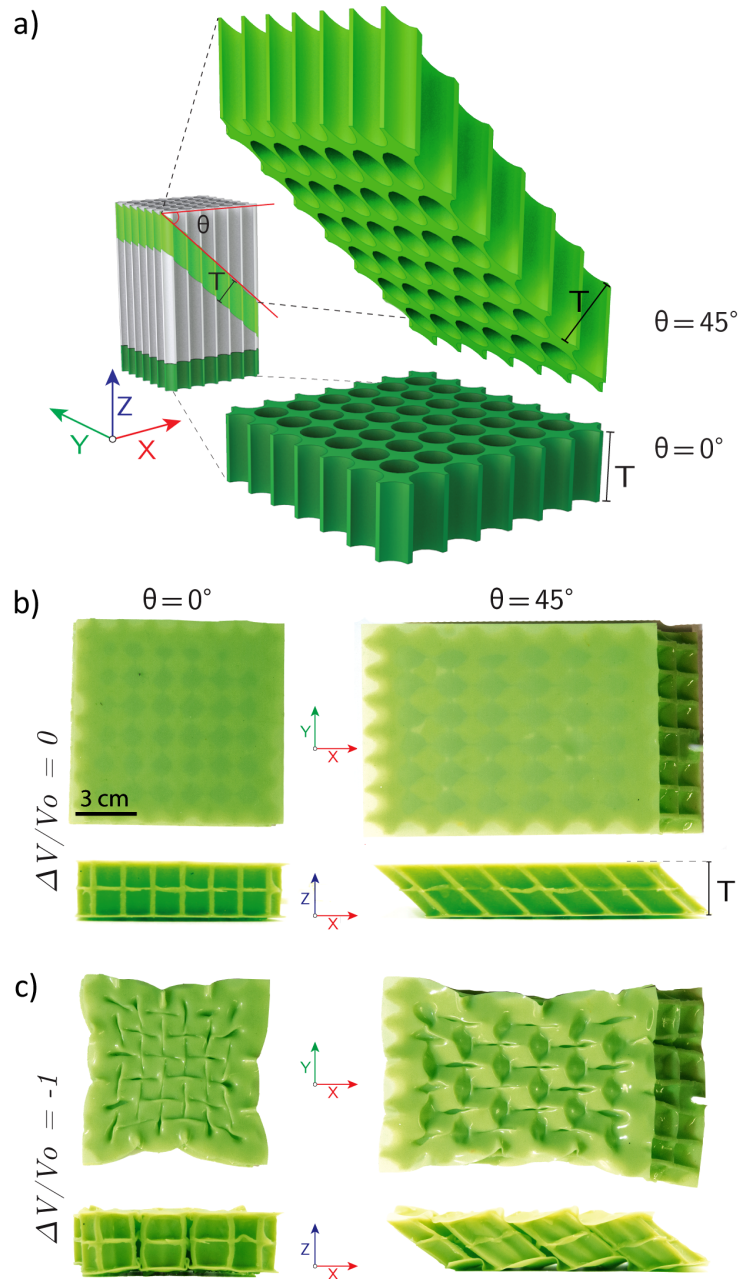


Figure 4.1: Conceptual visualization and buckling-induced geometric transformations in our inclined metamaterial. (a) Shown in light green, this structure is derived from conceptually slicing a block (shown in gray), containing a square array of cylindrical holes, at an angle θ . (b)-(c) pre- and post-buckling photos of the metamaterial at (b) $\Delta V/V_0 = 0$ and at (c) $\Delta V/V_0 = -1$ configurations for samples with $\theta = 0^\circ$ (left) and $\theta = 45^\circ$ (right). Both top and side views are shown. Additional information on this figure can be found in [Supplementary Video 1](#).

The structures were fabricated from a silicone elastomer (Zhermack Elite Double 32) utilizing a molding approach, and hydraulic actuation was employed to load the structures, while minimizing boundary effects. To achieve this behavior, the metamaterial was made air/water-tight by covering its top and bottom faces with thin elastomeric sheets (with thickness of ~ 0.5 mm). A single pressure input actuation was achieved by connecting the cylindrical cavities via channels and slowly removing a ΔV volume of water through a syringe pump (see sections C.1 to C.3 and figures C.1, C.2 and C.4 for details on geometry, fabrication, and experimental testing).

In figure 4.1(b)-(c), we show photos of the metamaterial with $\theta = 0^\circ$ and 45° for $\Delta V/V_0 = 0$ (initial configuration - figure 4.1(b)) and $\Delta V/V_0 = -1$ (figure 4.1(c)), where V_0 denotes the total volume of the holes in the initial (non-evacuated) configuration. As expected^[71], in the negative pressure regime, the ligaments separating the cavities buckle cooperatively, triggering a sudden transformation of the circular holes into a periodic pattern of alternating, and mutually orthogonal, elliptical holes. For the structure with $\theta = 45^\circ$, such transformations were accompanied by the formation of a periodic 3D pattern on its initially flat outer surfaces, suggesting that the angle θ may be exploited to trigger the formation of out-of-plane textured geometries.

To better understand the effect of θ on the post-buckling geometry of this class of metamaterials, we fabricated and characterized examples with $\theta = 0^\circ, 15^\circ, 30^\circ$ and 45° . The water-filled structures were connected to a syringe pump and the incompressible fluid was slowly removed from the cavities, while monitoring the evolution of the pressure using a pressure sensor (MPX5050DP, NXP USA Inc)(see section C.3.1 for details). The results reported in figure 4.2(a) demonstrate that all considered metamaterials are characterized by three distinct regions: (i) a linear elastic regime; (ii) a stress plateau following thereafter; and (iii) stiffening by further deflation. While in the initial linear regime the holes homogeneously contracted and the samples remained flat, the

sudden departure from linearity to a plateau pressure was caused by the buckling of the ligaments. Remarkably, for $\theta \neq 0^\circ$ the instability triggered the morphing of the sample's surfaces and produced 3D patterns with similar geometric features, whose sizes varied with θ (see figure C.6 for more information).

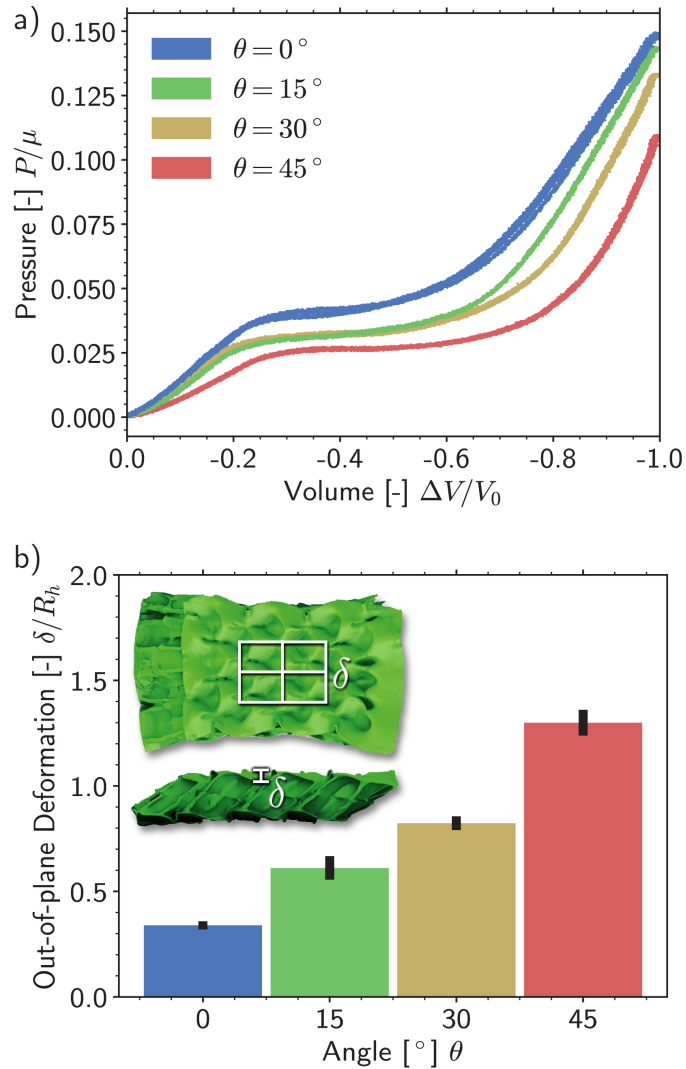


Figure 4.2: Experimental characterization of out-of-plane metamaterial buckling. (a) Pressure-volume relationship for the four different θ 's considered ($\theta=0^\circ, 15^\circ, 30^\circ, 45^\circ$). Each sample was tested independently three times and the results from each test are reported as separate lines. (b) Normalized out-of-plane deformation measurements of the samples, obtained from 3D surface scans. The inset specifies the four regions (denoted by white boxes) used for measuring δ . Additional information on this figure can be found in [Supplementary Video 2](#).

To quantify the magnitude of the associated out-of-plane deformation, we used a hand-held 3D scanner (Artec Space Spider, Artec Studio 14.1.1.75) and recorded the buckled surface profile at $\Delta V/V_0 = -1$ (see figure C.7 and section C.3.2 for more details). For these measurements, we focused on the four central unit cells of the sample (see dashed rectangles in figure 4.2(b) inset) and used a custom Python script to segment and detect the amplitude of the out-of-plane displacement in each of the four regions, $\delta = \max(u_z) - \min(u_z)$. In figure 4.2(b) we report the average of the four measured values of δ for each metamaterial. These results clearly show that the out-of-plane deformation of the structures becomes more accentuated as θ increases from 0° to 45° .

Since the buckling-induced textures have identical morphologies, but an out-of-plane amplitude that monotonically increases with θ , in the following sections, we only consider the metamaterials with $\theta = 0^\circ$ and $\theta = 45^\circ$. These two configurations provide the maximum difference in 3D deformation, and therefore represent the best candidates for demonstrating how the buckling-induced textures can be leveraged to modulate additional functionalities of these metamaterials, such as light reflection and friction.

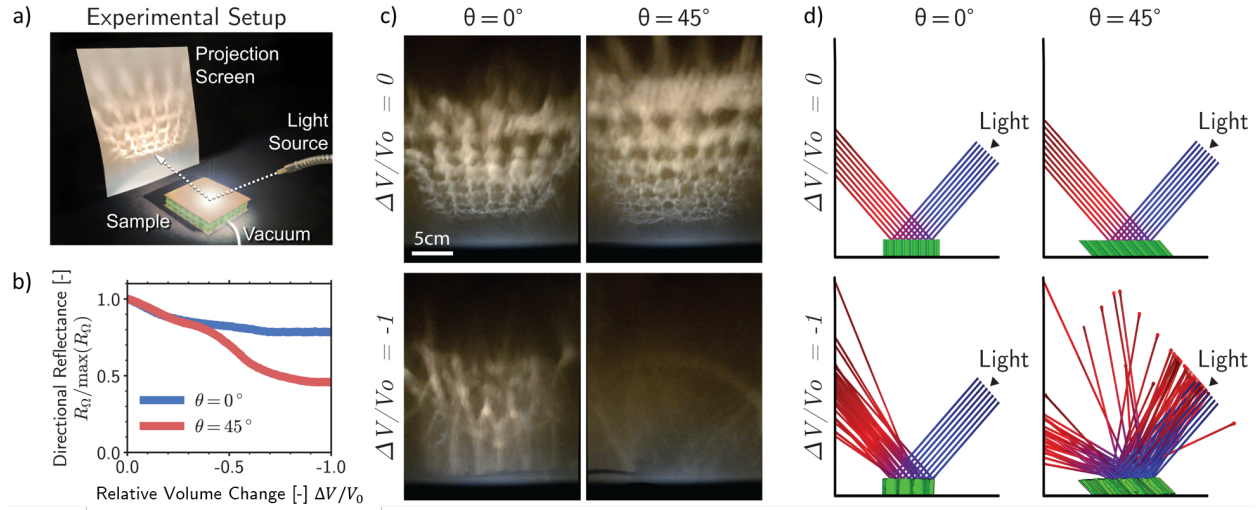


Figure 4.3: Buckling-induced tunable light reflection. (a) Photograph of the experimental setup outlining the sample location, light source, and pattern collection screen. (b) Evolution of the measured directional reflectance R_{Ω} (normalized by $\max(R_{\Omega})$) as a function of $\Delta V/V_0$ for samples with $\theta = 0^\circ$ and $\theta = 45^\circ$. (c) Snapshots obtained during the deflation process for the $\theta = 0^\circ$ (left column) and $\theta = 45^\circ$ (right column) samples at $\Delta V/V_0 = 0$ (top row) and $\Delta V/V_0 = -1$ (bottom row). (d) Ray tracing simulations showing the directionality of light reflection for $\theta = 0^\circ$ (left column) and $\theta = 45^\circ$ (right column) samples at $\Delta V/V_0 = 0$ (top row) and $\Delta V/V_0 = -1$ (bottom row). For reference, the initial periodic reflected light pattern is due to small surface depressions in the non-evacuated structure. Additional information on this figure can be found in [Supplementary Video 3](#).

To investigate buckling-induced tunable light reflection of our metamaterial, we turned its surface into a mirror by mixing gold paint with the silicone elastomer used for casting the thin membranes that formed the top and bottom surfaces of the structure. For the experiments, which were conducted in a dark room, we positioned a goose-neck halogen lamp at a distance of 9.5 cm from the sample and at an incident angle of 45° relative to the metamaterial's surface (see section [C.3.3](#) for details). While filled with water, we slowly evacuated the structure and monitored the light reflected onto a white panel positioned at a distance of 11 cm from the sample (see figure [4.3\(a\)](#)). As shown in figure [4.3\(c\)](#), while for $\Delta V/V_0 = 0$, the amount of light reflected is similar for both the samples with $\theta = 0^\circ$ and $\theta = 45^\circ$, at $\Delta V/V_0 = -1$ it is substantially lowered for the $\theta = 45^\circ$ structure. To quantify this light scattering behavior, we converted the recorded projection screen

images to gray-scale, and measured the brightness of all pixels in this region of interest (denoted by the dashed red rectangle in figure 4.3(a)) and calculated the directional reflectance R_Ω as the mean of these values (see section C.3.3 for details). The results shown in figure 4.3(b) indicate that for $\Delta V/V_0 = -1$ the normalized directional reflectance, $R_\Omega/\max(R_\Omega)$, for the $\theta = 45^\circ$ structure is 32% lower than that for the $\theta = 0^\circ$ structure. This stark difference in performance is due to the fact that upon buckling of the top surface of the $\theta = 45^\circ$ metamaterial, the incident rays are scattered in multiple directions, such that only few of them reach the white panel. This phenomenon is also clearly visible in simulations conducted using the Ray Tracing Module in COMSOL (see section C.4.2 for details). The numerical results reported in figure 4.3(d) show that (i) for $\Delta V/V_0 = 0$ (i.e. when the top surface is flat) the metamaterial acts as a planar mirror irrespective of θ and reflects all rays at 45° angle; (ii) for $\Delta V/V_0 = -1$ the $\theta = 0^\circ$ sample, on average, still reflects the incident rays at a 45° angle from the sample surface, with small deviations due to small and local perturbations of the surface smoothness; (iii) for $\Delta V/V_0 = -1$ the $\theta = 45^\circ$ sample reflects the light rays at vastly different angles from the sample surface – resulting in a diffuse distribution of light reflected in multiple directions. While wrinkling patterns have been proposed to create microlenses with variable focal length^[136,148] and achieve dynamic changes in optical transmittance and diffraction patterns^[149], our results show that buckling in porous metamaterials also provides opportunities to control the specular and diffuse optical scattering, opening avenues for tuning sunlight reflection in architectural applications or the encryption of messages and graphics that reversibly appear and disappear due to actuation.^[149]

Changes in surface morphology can also translate into changes in frictional properties of a structure, and to demonstrate this behavior, we placed our metamaterial on an acrylic plate, containing a layer of masking tape (Duck 240883) to reduce surface friction. The acrylic plate was

then tilted, and the smallest tilting angle for which the sample began sliding, ϕ_{cr} , was recorded. From these measurements, we calculated the coefficient of static friction $\mu = \tan \phi_{cr}$ as a function of ΔV for each geometry. Since μ is determined by the interaction between the substrate (tape) and the surface of the metamaterial, we found that μ remains constant when varying $\Delta V/V_0$ and/or θ for each sample. For example, if we consider the sample with $\theta = 45^\circ$ (see figure 4.4(a), first column), we observed that the structure has the same tilting angle ϕ_{cr} in both the initial and the buckled configuration (figure 4.4(b), first column) - a feature that is also observed for the sample with $\theta = 0^\circ$ (see figure C.9). As such, the friction coefficient is $\mu \approx 0.95$ for any $\Delta V/V_0$ (gold bars in figure 4.4(c)).

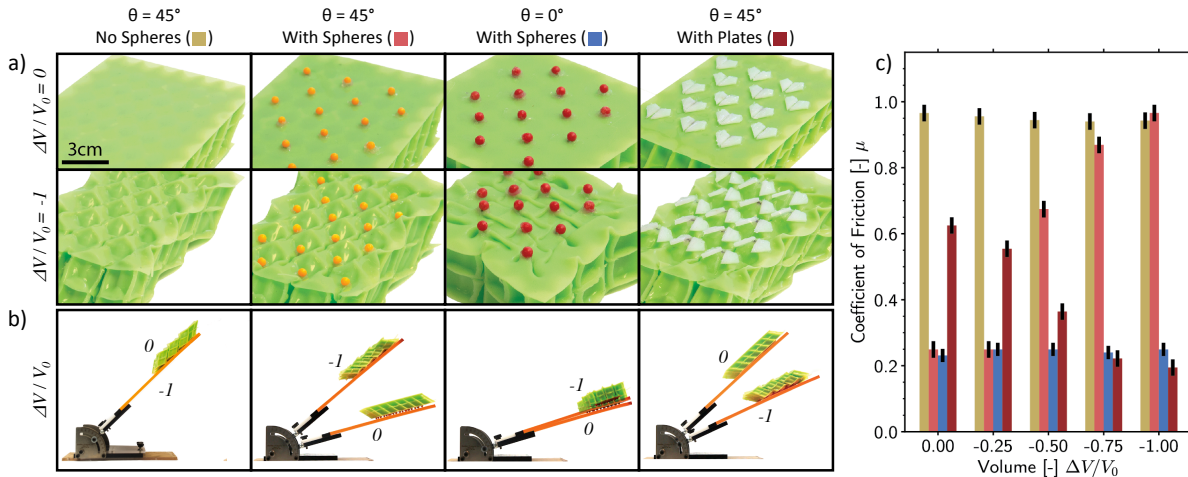


Figure 4.4: Frictional measurements for our inclined metamaterial. (a) Photographs showing the bottom surface at the $\Delta V/V_0 = 0$ (top row) and $\Delta V/V_0 = -1$ (bottom row) states of samples with (from left to right): (i) $\theta = 45^\circ$ and no acrylic features; (ii) $\theta = 45^\circ$ and acrylic spheres; (iii) $\theta = 0^\circ$ and acrylic spheres; (iv) $\theta = 45^\circ$ and acrylic plates. (b) Photographs qualitatively showing the effect of the buckling-induced morphology on the tilting angle for which the sample began to slide, ϕ_{cr} . (c) Coefficient of friction for the different samples as a function of $\Delta V/V_0$. See figures C.8 to C.10 for additional information and results. Additional information on this figure can be found in [Supplementary Video 4](#).

Beyond the ability of these metamaterials to generate large-scale out-of-plane surface geometries, this behavior also offers the opportunity to expose/retract a third material, leading to a tunable

μ . For example, if we simply attach small acrylic spheres in the areas of the surface that retract during buckling (figure 4.4(a), second column), such elements (*i*) dominate the contact properties in the initial configuration and (*ii*) disengage with the substrate under vacuum, which then comes in contact with the the elastomer. This behavior enables switching from an acrylic-tape to a elastomer-tape interaction. As such, the frictional coefficient between the metamaterial and the substrate is low prior to buckling (with $\mu \approx 0.25$) and progressively increase as the buckling-induced pattern becomes more accentuated, eventually reaching $\mu \approx 0.95$ (pink bars in figure 4.4(c)). Note that in this structure, the changing in frictional behavior is solely due to the emergence of the 3D pattern induced through buckling. In fact, if we attach the same acrylic spheres to the surface of the sample with $\theta = 0^\circ$, which does not exhibit a 3D pattern upon air evacuation (figure 4.4(a), third column), we find that $\mu \approx 0.25$ for both the initial and the buckled configuration (blue bars in figure 4.4(c)) as the spheres are always in contact with the substrate.

An effective friction coefficient μ that decrease as a function of $\Delta V/V_0$ is also achievable. By swapping the spheres with acrylic plates (figure 4.4(a), fourth column) coated by a thin layer of silicone adhesive (Sil-Poxy, Smooth-On), one can obtain a metamaterial with a friction coefficient that decrease upon air evacuation. Initially, the silicone adhesive is in contact with the substrate and $\mu \approx 0.62$. However, when the buckling-induced 3D pattern forms, the acrylic plates rotate and their edges (which are not coated) come in contact with the substrate, reducing μ to approximately 0.2 (dark red bars in figure 4.4(c)).

To demonstrate this effect, we created a soft crawling robot that harnesses the switchable frictional properties of our metamaterial to achieve locomotion. The robot comprises three metamaterial modules (see figure 4.5(a)). The first module is characterized by $\theta = 45^\circ$ and has spheres attached to its surface. The second module also has spheres attached to its surface, but with $\theta = 0^\circ$.

Finally, the third module ($\theta = 45^\circ$) is rotated 180 degrees relative to the first, and contains acrylic plates instead of spheres. During assembly, the first and third modules of the robot were connected to the same pressure source, which allowed us to provide the same negative pressure at the front and the rear of the robot, and to reset it to atmospheric pressure, simultaneously. Moreover, in order to provide pressure continuity between the first and the second modules, we coupled these via a short tube (with 1.75 mm diameter).

In the initial configuration (photograph (i) in figure 4.5(b)) the friction coefficient between the first two modules and the substrate is $\mu \approx 0.25$, whereas for the third module, is $\mu \approx 0.6$. However, upon air evacuation, the coefficient of friction varies differently for each of the three modules (see figure 4.4(c)). Note that, for simplicity, in this demonstration we use a pressure controlled air vacuum line to power the robot, but the effect of fluid compressibility on the response of the system was negligible.

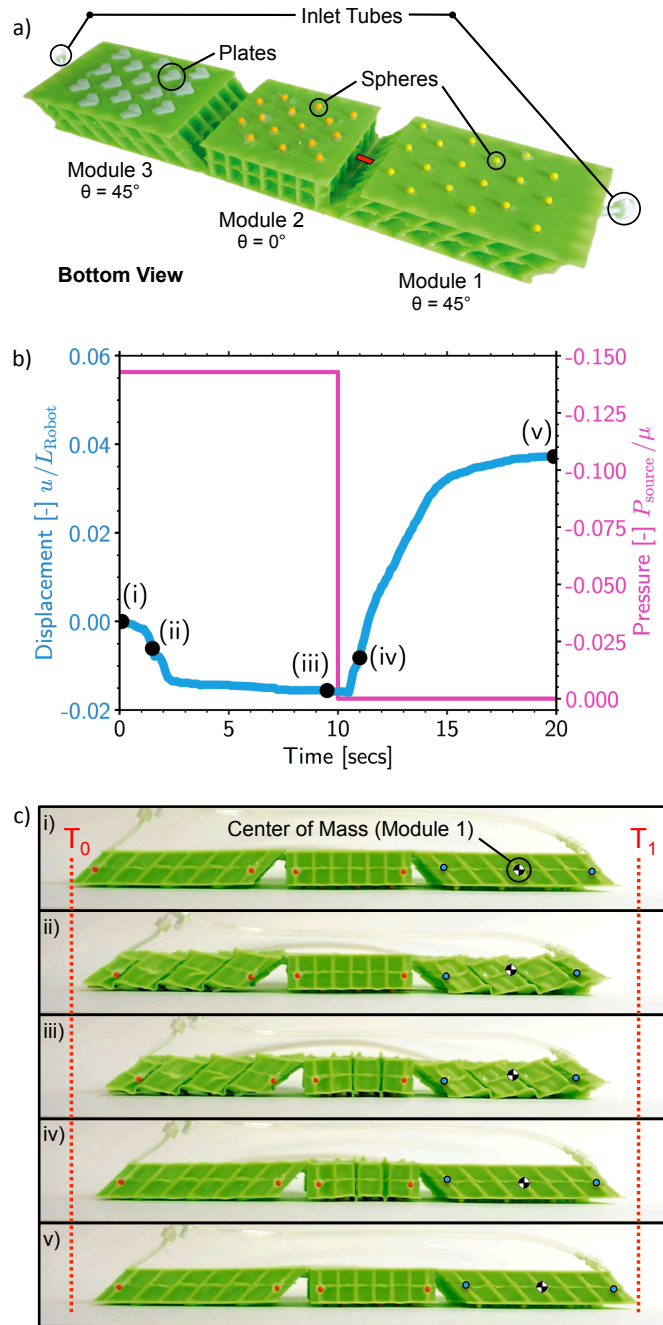


Figure 4.5: Design elements and performance of our soft robotic crawler. (a) Photograph showing the bottom of the soft robotic crawler. (b) Displacement of the center of mass of the first module of the crawler, u , normalized by the initial length of the crawler, L_{robot} , (blue line) and source pressure, P_{source} , (magenta line) versus time during a cycle. The center of mass provides information on the average displacement of the first module of the robot, which is obtained by averaging the displacement of both edge points for each frame. (c) Experimental snapshots of our soft crawler at $t = (i) 0, (ii) 1.5, (iii) 9.5, (iv) 11$ and $(v) 20$ s. The distance traveled during one full motion cycle (between T_0 and T_1) is indicated by the locations of the two red dotted lines. Additional information on this figure can be found in [Supplementary Video 5](#).

From analyzing the pressure-volume relationship reported in figure 4.2(a), we predict that the two modules with $\theta = 45^\circ$ buckle first, followed by the module with $\theta = 0^\circ$, in the negative pressure regime. This sequence of events is confirmed through our experimental testing, which demonstrates that when a negative pressure pulse is provided to the robot (with magnitude $P_{source} = 50$ kPa for $t = 10$ s), we see that the first and third modules with $\theta = 45^\circ$, which are connected to the same vacuum line, buckle before the second module with $\theta = 0^\circ$ (snapshot (ii) in figure 4.5(b)). The emergence of the 3D pattern triggered by buckling leads to an increase in friction (from $\mu \approx 0.25$ to $\mu \approx 0.95$) for the first module, which becomes an anchoring point. At the same time, the third module loses its ability to grip (from $\mu \approx 0.6$ to $\mu \approx 0.2$), which facilitate its forward sliding. Finally, the second module buckles (snapshot (iii) in figure 4.5(b)). Since buckling only leads to its contraction but does not change its frictional properties, this module merely acts as a stroke amplifier and gets pulled forward. As a result, at the end of complete air evacuation the robot advances on average by 9.3 ± 0.4 mm (figure 4.5(c)).

In the second step of the gait cycle, we release the robot from the vacuum, by simultaneously opening the first and the third modules to the atmosphere. According to the pressure-volume relationship reported in figure 4.2(a) the second module (with $\theta = 0^\circ$) should unbuckle first, followed by the $\theta = 45^\circ$ samples. However, in our experiments the first and third modules (with $\theta = 45^\circ$) unbuckle immediately (snapshot (iv) in figure 4.5(b)), due to their proximity to the outlets at atmospheric pressure. The relaxing of the 3D pattern on the surface of the first module removes the anchoring point, as the friction decreases from $\mu \approx 0.95$ to $\mu \approx 0.25$. At the same time, the third module regains grip, becoming the new anchoring point. Successively, when the middle module unbuckles (snapshot (v)) the robot slides forward again, advancing on average by additional 8.7 ± 0.4 mm (figure 4.5(c)). As a result, at the end of the complete gait cycle, the crawling robot

advances on average by 18 mm (figure 4.5(c)).

To summarize, in the present work we investigated the properties of a metamaterial consisting of an elastomeric block with a square array of tilted cylindrical holes. We discovered that the hole tilting angle (θ) plays a major role in the out-of-plane buckling behavior and the emergence of 3D morphologies on the exposed surfaces of the samples. Furthermore, we demonstrated how these patterns can be utilized to control surface properties (including light reflectance and friction) by means of a simple hydraulic or pneumatic actuation.

Although throughout this study, we focused on a square array of holes, this concept can be also extended to different hole arrangements. To explore this avenue, we used Finite Element analyses to simulate metamaterials with different periodic distributions of cylindrical holes (more details of which can be found in section C.4.1). Specifically, we focused on arrangements that have been previously shown to reversibly switch between expanded (i.e. with circular holes) and compact (i.e. with elongated, almost fully closed elliptical holes) configurations for $\theta = 0^\circ$ ^[150]. In full agreement with previous studies^[150], we find that when the holes' axes are perpendicular to the top and bottom surfaces, buckling triggers a planar geometric transformation (see figure C.5). In contrast, as shown in figure 4.6, for $\theta = 45^\circ$, all geometries exhibit different buckling-induced out-of-plane deformation patterns. These results suggest that our approach can be used to achieve more complex and targeted out-of-plane buckling behaviors, providing a new modular platform that enables the design of the next generation of active and transformable surfaces.

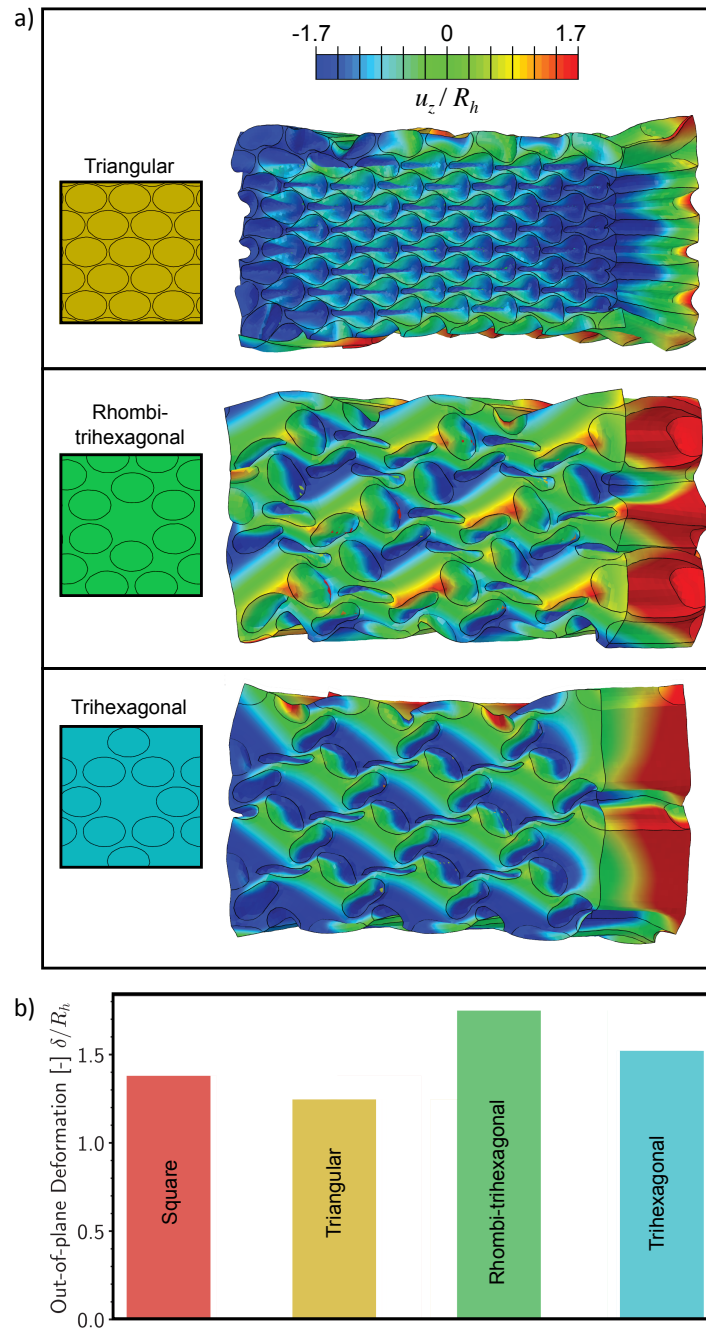


Figure 4.6: Out-of-plane buckling behaviors for different hole patterns. Post-buckling finite element results for three hole arrangements with $\theta = 45^\circ$ at $\Delta V/V_0 = -1$. For the triangular, rhombitrihexagonal, and trihexagonal holes arrays (the undeformed geometry is shown in the insets), we illustrate the normalized out-of-plane displacement, u_z/R_h . (b) Normalized out-of-plane deformation measurements obtained from Finite Element simulations at $\Delta V/V_0 = -1$ for the triangular, rhombitrihexagonal, and trihexagonal geometries, and the square arrangement from figure 4.1. Additional information on this figure can be found in [Supplementary Video 6](#).

5

Additional Work

5.1 Band Gaps in Acoustic Networks

5.1.1 Publication

Harnessing Geometric Frustration to Form Band Gaps in Acoustic Networks

Pai Wang, Yue Zheng, **Matheus C. Fernandes**, Yushen Sun, Kai Xu, Sijie Sun, Sung Hoon Kang, Vincent Tournat, Katia Bertoldi

Physical Review Letters, Volume 118, Issue 8, EID 084302, February 2017

doi:10.1103/PhysRevLett.118.084302

5.1.2 Abstract

We demonstrate both numerically and experimentally that geometric frustration in two-dimensional periodic acoustic networks consisting of arrays of narrow air channels can be harnessed to form band gaps (ranges of frequency in which the waves cannot propagate in any direction through the system). While resonant standing wave modes and interferences are ubiquitous in all the analyzed network geometries, we show that they give rise to band gaps only in the geometrically frustrated ones (i.e. those comprising of triangles and pentagons). Our results not only reveal a new mechanism based on geometric frustration to suppress the propagation of pressure waves in specific frequency ranges, but also opens avenues for the design of a new generation of smart systems that control and manipulate sound and vibrations.

5.2 Heart Valve

5.2.1 Publication

A geometrically accommodating heart valve replacement

Sophie C. Hofferberth, Mossab Y. Saeed, Lara Tomholt, **Matheus C. Fernandes**, Christopher J. Payne, Karl Price, Gerald R. Marx, Jesse J. Esch, David W. Brown, Jonathan Brown, Peter E. Hammer, Richard W. Bianco, James C. Weaver, Elazer R. Edelman, Pedro J. del Nido
Science Translational Medicine, Volume 12, Issue 531, eaay4006, February 2020

doi:10.1126/scitranslmed.aay4006

5.2.2 Abstract

While congenital heart valve disease has life-threatening consequences that warrant early valve replacement, the development of a growth-accommodating prosthetic valve has remained elusive, and as such, thousands of children continue to face multiple high-risk open-heart operations to replace outgrown valves. Here, we demonstrate a biomimetic prosthetic valve that is size-adjustable to accommodate somatic growth and structural asymmetries within the heart. Inspired by the human venous valve, whose geometry is optimized to preserve functionality across a wide range of constantly varying volume loads and diameters, our geometrically accommodating synthetic bileaflet valve analog exhibits similar adaptability to dimensional and shape changes. Benchtop and acute in vivo experiments validated design functionality, and in vivo survival studies in a growing animal model demonstrated mechanical valve expansion to accommodate growth. As

illustrated in this work, dynamic size adaptability with preservation of unidirectional flow in prosthetic valves thus offers a new paradigm of care for the treatment of heart valve disease.

5.3 Tunable Materials

5.3.1 Publication

Tunable infrared transmission for energy efficient pneumatic building façades

Lara Tomholt, Olga Geletina, Jack Alvarenga, Anna V. Shneidman, James C. Weaver, **Matheus C. Fernandes**, Santiago A. Mota, Martin Bechthold, Joanna Aizenberg

Energy and Buildings Volume 226, November 2020, 110377

doi:10.1016/j.enbuild.2020.110377

5.3.2 Abstract

Thermal regulation of buildings in climates with daily and seasonal weather changes can prove challenging and result in high building energy consumption. While adaptable façades with tunable infrared transmitting properties would be able to modulate solar transmittance through the building envelope and as such increase energy efficiency, available technologies are often expensive, relatively complicated, and challenging to implement in a lightweight form factor. Motivated by these limitations, this report presents a novel tunable light-modulating technology for energy efficient pneumatic façades in the form of polydimethylsiloxane (PDMS) film with a thin gold surface coating. Sequential stretching and relaxing of this film results in strain-induced microscale surface cracks that can significantly modulate both visible and near infrared light transmission and consequently the material's solar heat gain coefficient (SHGC). The material's tunability has shown a

significant potential to reduce building energy use, as assessed with building simulation software. The technology offers additional advantages for light modulation in pneumatic façades including real-time operation, ease of implementation and control, and predictable performance. Façade design guidelines for the integration of the infrared regulating film into ethylene tetrafluoroethylene (ETFE) building envelopes and climate suitability are described, and a critical evaluation of material durability, optical clarity, and material costs are provided.

5.4 Brittle Star Arm Kinematics

5.4.1 Publication

The structural origins of brittle star arm kinematics: An integrated tomographic, additive manufacturing, and parametric modeling-based approach

Lara Tomholt, Larry J. Friesen, Daniel Berdichevsky, **Matheus C. Fernandes**, Christoph Pierre, Robert J. Wood, James C. Weaver

Journal of Structural Biology, Volume 211, Issue 1, 107481, July 2020

doi:10.1016/j.jsb.2020.107481

5.4.2 Abstract

Brittle stars are known for the high flexibility of their arms, a characteristic required for locomotion, food grasping, and for holding onto a great diversity of substrates. Their high agility is facilitated by the numerous discrete skeletal elements (ossicles) running through the center of each arm and embedded in the skin. While much has been learned regarding the structural diversity of these ossicles, which are important characters for taxonomic purposes, their impact on the arms' range of

motion, by contrast, is poorly understood. In the present study, we set out to investigate how ossicle morphology and skeletal organization affect the flexibility of brittle star arms. Here, we present the results of an in-depth analysis of three brittle star species (*Ophioplocus esmarki*, *Ophiopteris papillosa*, and *Ophiothrix spiculata*), chosen for their different ranges of motion, as well as spine size and orientation. Using an integrated approach that combines behavioral studies with parametric modeling, additive manufacturing, micro-computed tomography, scanning electron microscopy, and finite element simulations, we present a high-throughput workflow that provides a fundamental understanding of 3D structure-kinematic relationships in brittle star skeletal systems.

5.5 Beetle Structural Color

5.5.1 Publication

Tough color: The functional hierarchy of flower beetles' cuticle prioritizes optics over mechanics

Zian Jia, **Matheus C. Fernandes**, Zhifei Deng, Ting Yang, Qiuting Zhang, Alfie Lethbridge, Jie Yin, Jae-Hwang Lee, Lin Han, James C. Weaver, Katia Bertoldi, Joanna Aizenberg, Mathias Kolle, Pete Vukusic, Ling Li

Proceedings of the National Academy of Sciences of the United States of America, Volume 118, Issue 25, June 2021

doi:10.1073/pnas.2101017118

5.5.2 Abstract

Biological systems have a remarkable capability of synthesizing multifunctional materials that are adapted for specific physiological and ecological needs. When exploring structure–function rela-

tionships related to multifunctionality in nature, it can be a challenging task to address performance synergies, trade-offs, and the relative importance of different functions in biological materials, which, in turn, can hinder our ability to successfully develop their synthetic bioinspired counterparts. Here, we investigate such relationships between the mechanical and optical properties in a multifunctional biological material found in the highly protective yet conspicuously colored exoskeleton of the flower beetle, *Torynorrhina flammea*. Combining experimental, computational, and theoretical approaches, we demonstrate that a micropillar-reinforced photonic multilayer in the beetle's exoskeleton simultaneously enhances mechanical robustness and optical appearance, giving rise to optical damage tolerance. Compared with plain multilayer structures, stiffer vertical micropillars increase stiffness and elastic recovery, restrain the formation of shear bands, and enhance delamination resistance. The micropillars also scatter the reflected light at larger polar angles, enhancing the first optical diffraction order, which makes the reflected color visible from a wider range of viewing angles. The synergistic effect of the improved angular reflectivity and damage localization capability contributes to the optical damage tolerance. Our systematic structural analysis of *T. flammea*'s different color polymorphs and parametric optical and mechanical modeling further suggest that the beetle's microarchitecture is optimized toward maximizing the first-order optical diffraction rather than its mechanical stiffness. These findings shed light on material-level design strategies utilized in biological systems for achieving multifunctionality and could thus inform bioinspired material innovations.

5.6 Soft Membrane Design via Machine Learning

5.6.1 Publication

Inverse design of soft membranes through machine learning

Antonio Elia Forte, Emilia Zaria, Lishuai Jin, Paul Hanakata, Ahmad Zareei, **Matheus C. Fernandes**, Laura Sumner, Jonathan Alvarez, Christopher Payne, and Katia Bertoldi.

Proceedings of the National Academy of Sciences of the United States of America, In Preparation

5.6.2 Abstract

Across fields of science, researchers have increasingly focused on designing soft devices that can shape-morph and achieve functionality upon actuation. However, building such tools involves understanding of complex non-linear mechanics and inverse design capabilities. A powerful method to solve the backward deformation problem can be tackled with classic machine learning tools. In this study we present a simple and efficient platform to design pre-programmed 3D shapes starting from two-dimensional planar composites membranes. By training a custom built autoencoder with a small set of finite element simulations, we are able to obtain the optimal design for a pixelated 2D elastomeric membrane, which can morph to a target shape upon inflation. We show how these devices can be used for mechanotherapy applications, by stimulating certain areas whilst avoiding prescribed locations, but the potential of the method can be employed at multiple scales and across different applications without loss of generality.

5.7 Soft Robot Sensor Using Machine Learning

5.7.1 Publication

Soft Robot Gripper with Camera-less Object Classification using Machine Learning

Matheus C. Fernandes, Andrew Gross, Kevin Li, Nikolaos Vasios, James C. Weaver, Katia Bertoldi.

Unpublished.

5.7.2 Abstract

Current automation and soft robotic arms use a collection of cameras and sensors to grab and identify inventory objects in manufacturing as well as distribution centers. However, due to sensing limitations, these systems may not be able to classify objects based on features such as compliance, texture and shape. In this project we explore a new and exciting avenue to classify gripped objects via compliance, curvature and pressure data from embedded sensors in combination with machine learning algorithms. We introduce a soft pneumatic actuator that is able to conform to a desired objects shape and size while continuously providing sensor data from multiple force sensors, curvature sensors and fluid pressure sensors. By acquiring data for multiple pre-classified objects, we develop a training database that is used in generative classification machine learning model. Using the model, we are then able to predict the classification new objects. Furthermore, we validate our model by testing a set of objects for which the classes are known and use similar untrained items to understand the limitations of the model and machinery.

6

Conclusions

“CHALLENGES ARE WHAT MAKE LIFE INTERESTING AND OVERCOMING THEM IS WHAT MAKES LIFE MEANINGFUL.”

– JOSHUA J. MARINE

This dissertation illustrates two effective approaches to designing structures and advancing material science development by observing nature and biology. In the first approach, working *in-tandem* with biology, we take inspiration from the deep-sea glass sponge *Euplectella aspergillum* to improve the efficiency of a class of truss structures used in modern engineering applications. Using a combination of numerical simulations and experiments, we found that the sponge design has a superior strength-to-weight efficiency over other comparable designs (chapter 2). Furthermore, we developed an optimization algorithm, based on our numerical models, that surveys the design space and finds the optimal geometric configuration of trusses. The results from the algorithm suggest that the sponge's skeletal architecture is nearly identical to the optimum output design. The mechanical properties of the sponge-inspired lattice thus have implications for improving the performance of a wide range of truss systems, with applications ranging from large-scale infrastructure such as bridges and buildings to small-scale medical implants. Since this improved efficiency is introduced geometrically, the structure's scale and material is unlikely to impact its performance.

Using a combination of mechanical and hydrodynamic simulations of the sponge's macro-scale geometry, my colleagues and I were able to shed light on the structure-function relationship of the different components of the sponge's structural hierarchy (chapter 3). We demonstrated that the sponge's ridge architecture offers lessons on how to effectively suppress hydrodynamic vortex shedding by using its unique and regular ridge pattern that tapers in height from the bottom (short ridge near the holdfast) to the top (tall ridge away from the holdfast) of the sponge. Furthermore, we find that although the ridge height is smaller near the holdfast apparatus, the amount of material per unit area remains constant, leading to a thicker relative strut dimension. In our structural simulations of the sponge we demonstrated that by allocating additional material to the sponge

core we are able to achieve a more efficient load-bearing structure than if allocated through the introduction of ridges. These results are consistent with the findings of chapter 2, where we show that its diagonally reinforced truss design is optimized for load-bearing capabilities.

While the findings of this study provide new insights into the multi-functionality of the complex external ridges in the skeleton of the sponge, our discoveries are also relevant for many man-made cylindrical structures where hydrodynamic shedding or structural rigidity play an important role. This study exemplifies yet another instance of working *in-tandem* with biology to improve the engineering of structures and their interaction with the natural environment.

The second approach, working *in-parallel* with nature, is illustrated in the third project of this dissertation, where we utilize porous materials, found abundantly in nature, as the means to create a metamaterial that exhibits unexpected structural properties harnessed to accomplish complex tasks (chapter 4). In this chapter, we showed that buckling generates complex 3D morphologies in a new porous metamaterial comprising a square array of tilted cylindrical holes within an elastomeric matrix. We demonstrate that such buckling-induced 3D deformations can be harnessed to actively control surface properties such as reflectance and friction, providing new opportunities for the production of tunable light-diffusion devices and the creation of a new type of locomotion for plate-shaped soft robots. These results suggest that our approach can be used to achieve more complex and targeted out-of-plane buckling behaviors, providing a new modular platform that enables the design of the next generation of active and transformable surfaces.

6.1 Outlook

We can find many examples in our daily life where human-made technology can be traced to nature's inventions that were used as inspiration. Besides stronger structures with hydrodynamic capabilities or soft robots able to induce crawling, there are numerous other inventions and mechanisms that one can be inspired to develop using the same biomimicry techniques. One may consider deployable structures that can include tents and other large surface-foldable structures as well as gossamer antenna structures and deployable living quarters for space applications.

While the concept of resilient lattice architecture is many centuries old and dates back to Alexander Graham Bell and Buckminster Fuller, today's technology allows for lattices to be made small enough to exploit their nano-scale properties, allowing humans to develop a hierarchical approaches to material science.^[151,152] Although at this scale size effects can tremendously alter mechanical, magnetic, thermal, and electrical properties of a material, nature has been found to operate at these scales thus paving potential pathways to mitigate such complications.^[153–161] There are many areas where nature is superior, and one of them is its ability to create structures that use the minimum resources to produce maximum results as to be fitted for the environment in which they need to operate, independent of scale.

The possibilities in seeking inspiration from nature and biology to solve the most complex engineering problems are endless. In order to describe a biological material, it is necessary to understand the various hierarchical levels of a structure, from the nano- and meso-scale all the way to the macro-scale. On each of these scales, within the structural hierarchy of a biological species, there are endless opportunities for discovery and inspiration to work both *in-parallel* and *in-tandem* with nature.

6.2 Personal Remarks

“I want to become a super engineer” were the opening words of my Harvard admissions personal statement. These words meant a lot to me back then, and they still mean a lot to me to this day. Years later, the experiences gained through my research have provided me the realization that the definition of a ‘super engineer’ extends beyond being technically savvy. Moreover, it also encompasses humility, the ability to convey complex ideas to a non-technical audience, effectively collaborating with others across disciplines, and, most importantly, thinking critically and asking the right questions. This skill set is something I could have never achieved had I not worked on projects at the forefront of multi-disciplinary innovation. By collaborating with a diverse and brilliant group of people, I have learned that becoming a ‘super engineer’ is not a binary achievement, but rather a lifetime purpose of learning and development.



Supplementary Information: Mechanically
Robust Lattices Inspired By Deep-Sea
Glass Sponges

BY: MATHEUS C. FERNANDES, JOANNA AIZENBERG, JAMES C. WEAVER, AND KATIA BERTOLDI. PUBLISHED IN *NATURE MATERIALS*, ON SEPT. 21 2020. [doi:10.1038/s41563-020-0798-1](https://doi.org/10.1038/s41563-020-0798-1)

A.1 Structure of the Hexactinellid sponge *Euplectella aspergillum*

The periodic structures investigated in this study are inspired by the skeleton of the hexactinellid sponge *Euplectella aspergillum*, which throughout its lifespan (figure A.1) progresses from a easily deformable skeletal lattice (flexible phase), consisting of loosely associated individual skeletal elements, through various stages of skeletal consolidation, ultimately resulting in the mature form (rigid phase), shown in figure 2.1^[7,20,110]. In this section, we provide a detailed description of the sponge's geometry and measured dimensions.

Figure 2.1 shows a photograph of the entire skeleton of a representative specimen of *E. aspergillum*, and its intricate, cylindrical cage-like structure (20 to 25 cm long, 2 to 4 cm in diameter)^[18]. The surface of the cylinder incorporates a regular square lattice composed of a series of cemented vertical and horizontal struts, consisting of bundles of individual spicules, each with a circular cross-section. The cell spacing between horizontal and vertical struts is $L \approx 2.5 \text{ mm}$ ^[6], while the diameter is $D_{nd} \approx 0.25 \text{ mm}$ ^[6]. In addition to the horizontal and vertical struts, there is an additional set of diagonal elements, intersecting in a manner that creates a series of alternating open and closed cells, reminiscent of a checkerboard pattern^[6]. Although these diagonal elements are not as ordered as the horizontal and vertical ones, they can be approximated as two diagonal struts that are offset from the nodes (vertex joints between non-diagonal elements) and form roughly octagonal openings (figure A.2). To estimate the volume ratio between diagonal and non-diagonal elements, we acquired digital photographs of the sponge skeleton and performed image segmentation to segregate the projected area of the vertical/horizontal and diagonal spicules. For these measurements, and to minimize shadowing artifacts during image thresholding, sponge skeleton regions were selected that did not contain surface ridges. In total 4 different sponge skeletons were

investigated and 25 different lattice cells from each specimen were analyzed. Using this approach, the projected area ratio of non-diagonal to diagonal elements was found to be $A_{nd}/A_d \approx 1.41 \pm 0.16$. Note that here, and in the following, the subscripts d and nd are used to indicate the diagonal and non-diagonal (i.e. horizontal and vertical) elements, respectively.

Finally, it should also be noted that the sponge is reinforced by external ridges that extend perpendicular to the surface of the cylinder and spiral the cage at an angle of $\sim 45^\circ$. However, in this paper we do not report the effects of these ridges on its mechanical performance, which will be addressed elsewhere.

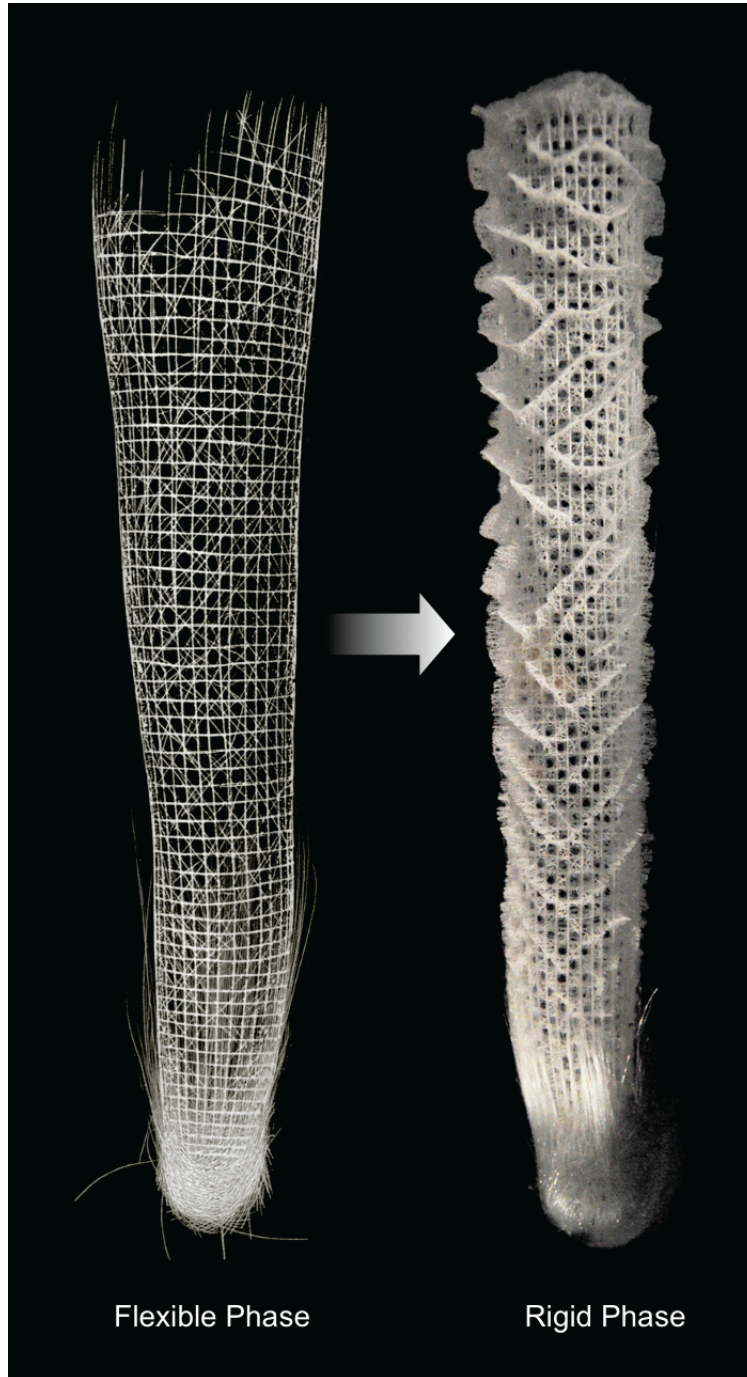


Figure A.1: Historical illustration (left) and modern photograph (right) illustrating the flexible and rigid growth stages that occur during skeletal maturation in several hexactinellid sponges in the genus *Euplectella*. Left image adapted from Schulze^[7].

A.2 Our four lattice designs

In this study, we focused on four different lattice configurations (*Designs A, B, C, and D*) constrained to deform in an in-plane setting only. In an effort to conduct a fair performance comparison between the different geometries, all four lattices were designed to contain the same total volume of material and a fixed volume ratio between non-diagonal and diagonal elements (chosen to match the sponge geometry) for *Designs A, B, and C*. Two different shapes were considered for the cross-section of the struts: circular and rectangular. For the circular cross-section case, we denoted the diameters of the non-diagonal (i.e. horizontal and vertical) and diagonal struts in the α -th design as $D_{\alpha,nd}$ and $D_{\alpha,d}$, respectively, and neglected out-of-plane buckling. For the rectangular cross-sections, we denoted the in-plane thickness of the non-diagonal (i.e. horizontal and vertical) and diagonal struts in the α -th design as $T_{\alpha,nd}$ and $T_{\alpha,d}$, respectively, and chose the depth H to avoid out-of-plane deformation (i.e. we chose the depth over thickness ratio sufficiently large to constrain in-plane deformation). Finally, it is important to note that the slenderness of the non-diagonal members in the α -th design $\in [A, B, C]$ was chosen as

$$\frac{D_{\alpha,nd}}{L} = 0.1, \quad \text{and} \quad \frac{T_{\alpha,nd}}{L} = 0.1, \quad (\text{A.1})$$

for the case of the circular and rectangular cross-section, since this was the aspect ratio measured for the sponges (section A.1).

In the subsequent sections, we describe in detail the unit cells for four different designs, and provide the derivations for the characteristics of each geometry cross-section. To derive these relations, we laid a framework of underlying assumptions, namely:

- in-plane geometry is uniform and has the same shape (allowing only either thickness or diameter to change depending on cross-sectional shape) for all elements,
- all diagonal elements have the same in-plane dimension,
- all non-diagonal elements have the same in-plane dimension, and
- area of overlapping beam crossing is negligible and unaccounted for during volume calculations.

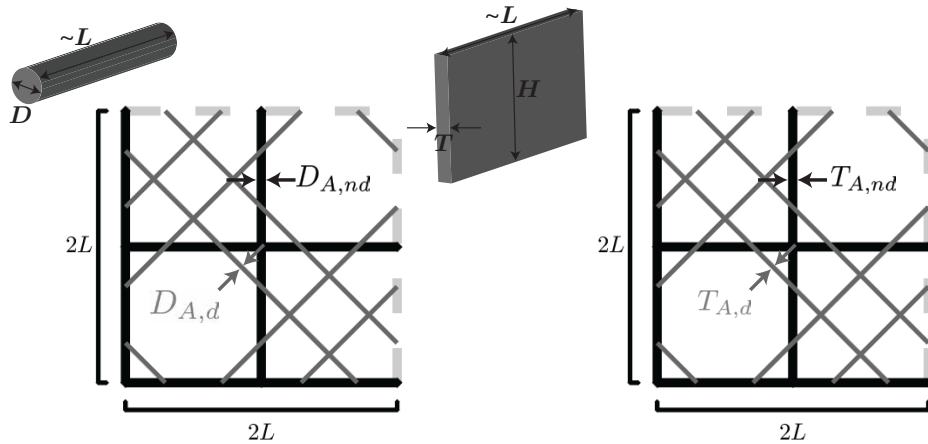


Figure A.2: Unit cell for Design A. Schematics of the unit cell for Design A (the sponge-inspired lattice). On the left, we indicate the geometric parameters of this design considering a circular cross-section, while on the right, we show the geometric parameters of this design considering a rectangular cross-section.

A.2.1 Design A

Design A was inspired by the sponge's skeletal architecture and consisted of a square grid reinforced by a double diagonal support system (figure A.2). Matching what was seen in the natural sponge, the diagonal elements were assumed to form an octagonal opening on every other cell, such that they intersect the horizontal and vertical struts at a distance $\Delta L = L/(\sqrt{2} + 2)$ from the nodes, where L denotes the length of the vertical and horizontal struts.

Circular cross-section

Assuming that the cross-section of all struts is circular, the projected area and volume for the non-diagonal ($A_{A,nd}$ and $V_{A,nd}$) and diagonal ($A_{A,d}$ and $V_{A,d}$) members are given by

$$A_{A,nd} = 8LD_{A,nd}, \quad (\text{A.2})$$

$$V_{A,nd} = 8L \left(\pi \frac{D_{A,nd}^2}{4} \right) = 2L\pi D_{A,nd}^2 \quad (\text{A.3})$$

$$A_{A,d} = 8\sqrt{2}LD_{A,d}, \quad (\text{A.4})$$

and

$$V_{A,d} = 8\sqrt{2}L \left(\pi \frac{D_{A,d}^2}{4} \right) = 2\sqrt{2}L\pi D_{A,d}^2. \quad (\text{A.5})$$

Since the projected area ratio of the non-diagonal to diagonal elements in the sponge has been measured to be

$$\frac{A_{A,nd}}{A_{A,d}} = 1.41, \quad (\text{A.6})$$

by substituting equation A.2 and equation A.4 into the equation above we find that for *Design A*

$$D_{A,nd} = 1.41\sqrt{2}D_{A,d} \approx 2D_{A,d}. \quad (\text{A.7})$$

Substitution of equation A.7 into equation A.3 and equation A.5 yields

$$\frac{V_{A,nd}}{V_{A,d}} = \frac{2L\pi D_{A,nd}^2}{2\sqrt{2}L\pi D_{A,d}^2} = 2\sqrt{2} \quad (\text{A.8})$$

and

$$V_{A,T} = V_{A,nd} + V_{A,d} = 2\pi L(D_{A,nd}^2 + \sqrt{2}D_{A,d}^2) = 2\pi L D_{A,nd}^2 \left(1 + \frac{1}{2\sqrt{2}}\right), \quad (\text{A.9})$$

where $V_{A,T}$ indicates the total volume of the unit cell for *Design A*.

Finally, it is important to note that in this study we used *Design A* as our base model, and thus constrained the total volume of all the other unit cell designs with circular cross-sections to be equal to that of *Design A*, namely,

$$V_{\alpha,d} + V_{\alpha,nd} = V_{A,T} = 2\pi L D_{A,nd}^2 \left(1 + \frac{1}{2\sqrt{2}}\right), \quad (\text{A.10})$$

with $\alpha = B, C$ and D . For *Designs B* and *C*, which comprised diagonal elements, we also constrained the volume ratio of the non-diagonal to diagonal elements to be the same as in *Design A*

$$\frac{V_{\alpha,nd}}{V_{\alpha,d}} = \frac{V_{A,nd}}{V_{A,d}} = 2\sqrt{2}, \quad (\text{A.11})$$

with $\alpha \in B$ and C .

Rectangular cross-section

Assuming that the cross-section of all struts is rectangular, the projected-area for the non-diagonal ($A_{A,nd}$) and diagonal ($A_{A,d}$) members is given by

$$A_{A,nd} = 8LT_{A,nd} \quad (\text{A.12})$$

and

$$A_{A,d} = 8\sqrt{2}LT_{A,d} \quad (\text{A.13})$$

where $T_{A,nd}$ and $T_{A,d}$ are the non-diagonal and diagonal in-plane strut thickness for *Design A*, respectively. Since for the sponge $A_{nd}/A_d \approx 1.41$, it follows that

$$T_{A,nd} = 2T_{A,d}. \quad (\text{A.14})$$

Finally, for the case of rectangular cross-section we used *Design A* as our base model, and thus constrained the total volume of all the other unit cell designs with rectangular cross-section to be equal to that of *Design A*, namely,

$$V_{A,T} = V_{\alpha,d} + V_{\alpha,nd} = 8LH(T_{A,nd} + \sqrt{2}T_{A,d}) = 8LHT_{A,nd} \left(1 + \frac{1}{\sqrt{2}}\right), \quad (\text{A.15})$$

with $\alpha \in \text{B, C and D}$. Moreover, for *Designs B-C*, which comprised diagonal elements, we also constrained the volume ratio of the non-diagonal to diagonal elements to be the same as in *Design A*,

$$\frac{V_{\alpha,nd}}{V_{\alpha,d}} = \sqrt{2}, \quad (\text{A.16})$$

with $\alpha \in B$ and C .

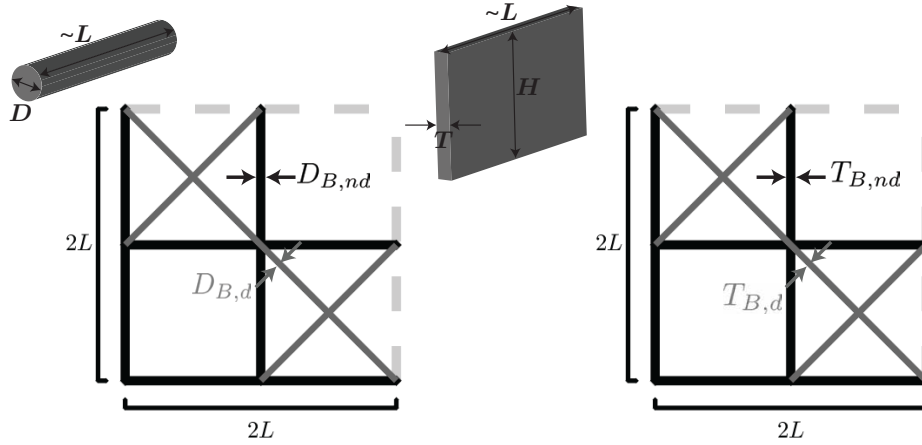


Figure A.3: Unit cell for Design B. Schematics of the unit cell for Design B (an alternating open and closed cell structure resembling the sponge and employing a single set of diagonal bracings). On the left we indicate the geometric parameters of this design considering a circular cross-section, while on the right we show the geometric parameters of this design considering a rectangular cross-section.

A.2.2 Design B

Design B was similar to the sponge design (Design A) and was likewise characterized by an alternation of open and closed cells (figure A.3). However, instead of having two diagonals offset from the nodes, in this design only one diagonal passes through the nodes crossing through every other cell.

Circular cross-section

For this design with circular cross-section, the non-diagonal and diagonal volumes are given by

$$V_{B,nd} = V_{A,nd} = 2\pi L D_{B,nd}^2 \quad (\text{A.17})$$

and

$$V_{B,d} = 2\sqrt{8}L \left(\pi \frac{D_{B,d}^2}{4} \right), \quad (\text{A.18})$$

respectively. Using the constraints provided by equation A.10 and equation A.11, as well as the above volumes, we obtain

$$D_{B,nd} = D_{A,nd} \quad (\text{A.19})$$

and

$$\frac{D_{B,d}}{D_{B,nd}} = \frac{1}{\sqrt{2}}. \quad (\text{A.20})$$

Rectangular cross-section

For this design with circular cross-section, the volume of the non-diagonal and diagonal members are given by

$$V_{B,nd} = 8LT_{B,nd}H. \quad (\text{A.21})$$

and

$$V_{B,d} = 4\sqrt{2}LT_{B,d}H. \quad (\text{A.22})$$

Using the constraints provided by equation A.15 and equation A.16, as well as the above volumes, we obtain

$$T_{B,nd} = T_{B,d} \quad (\text{A.23})$$

and

$$T_{B,nd} = T_{A,nd} \quad (\text{A.24})$$

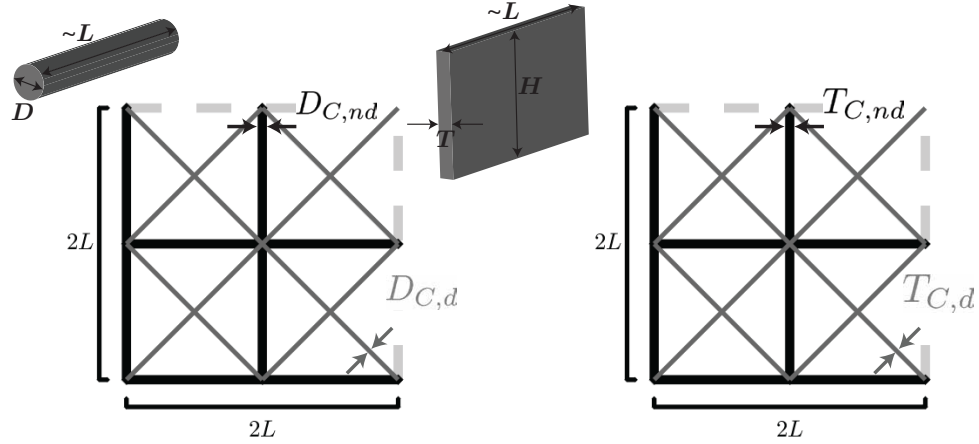


Figure A.4: Unit cell for Design C. Schematics of the unit cell for Design C (all cells filled with diagonal bracings, as is typically found in infrastructure applications). On the left we indicate the geometric parameters of this design considering a circular cross-section, while on the right we show the geometric parameters of this design considering a rectangular cross-section.

A.2.3 Design C

Design C was inspired by the Town lattice truss design introduced by architect Ithiel Town in 1820^[94,95] and consisted of every cell being reinforced by diagonal trusses passing through the nodes (figure A.4).

Circular cross-section

For this design with circular cross-section, the volume of the non-diagonal and diagonal members of the unit cell are given by

$$V_{C,nd} = V_{A,nd} = 2L\pi D_{A,nd}^2 \quad (\text{A.25})$$

and

$$V_{C,d} = V_{A,d} = 2\sqrt{2}L\pi D_{A,d}^2, \quad (\text{A.26})$$

respectively. Using the constraints provided by equation A.10 and equation A.11 we obtain

$$D_{C,nd} = D_{A,nd} \quad (\text{A.27})$$

and

$$\frac{D_{C,d}}{D_{C,nd}} = \frac{1}{2}. \quad (\text{A.28})$$

Rectangular cross-section

For this design with circular cross-section, the volume of the non-diagonal and diagonal members of the unit cell are given by

$$V_{C,nd} = 8LT_{C,nd}H \quad (\text{A.29})$$

and

$$V_{C,d} = 8\sqrt{2}LT_{C,d}H \quad (\text{A.30})$$

Using the constraints provided by equation A.15 and equation A.16, as well as the above volumes, we obtain

$$T_{C,nd} = 2T_{C,d}, \quad (\text{A.31})$$

and

$$T_{C,nd} = T_{A,nd}. \quad (\text{A.32})$$

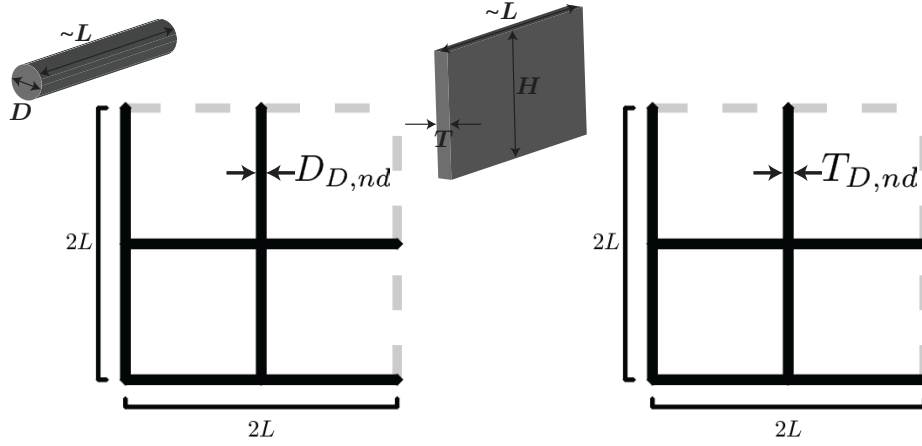


Figure A.5: Unit cell for *Design D*. Schematics of the unit cell for *Design D* (square lattice with no diagonal reinforcement). On the left we indicate the geometric parameters of this design considering a circular cross-section, while on the right we show the geometric parameters of this design considering a rectangular cross-section.

A.2.4 Design D

Design D comprised only the square grid without diagonal reinforcement (figure A.5). As such, for this design we allocated the total material volume to the non-diagonal elements. Note that this design is well known to be unstable and very limited in resisting shear forces^[103,104].

Circular cross-section

Since

$$V_{D,T} = V_{D,nd} = V_{A,nd} = 2\pi L D_{D,nd}^2, \quad (\text{A.33})$$

using the constraint provided by equation A.10 we obtain

$$D_{D,nd} = D_{A,nd} \sqrt{1 + \frac{\sqrt{2}}{4}}. \quad (\text{A.34})$$

Rectangular cross-section

Since

$$V_{D,T} = V_{D,nd} = 8LT_{D,nd}H, \quad (\text{A.35})$$

using the constraint provided by equation A.15 we obtain

$$T_{D,nd} = \left(1 + \frac{1}{\sqrt{2}}\right) T_{A,nd} \quad (\text{A.36})$$

A.3 Experimental Setup

A.3.1 Fabrication

We fabricated each of the lattice specimens with a Stratasys Connex500 multi-material 3D printer using the digital material FLX9795-DM. During the fabrication process, a photosensitive liquid precursor (the 3D printer "ink") is deposited in a voxel-by-voxel fashion. Several precursors are used to print multiple materials with different properties and the resulting modulus can be tuned by varying the concentration of photo-initiator. A UV light cross-links the liquid precursors in a layer-by-layer fashion and this process is repeated until the full 3D model is built. Each of the specimens were printed in parallel along with the print-head direction as to minimize material anisotropy between specimens. Depending on the liquid precursor composition and the degree of cross-linking, a broad range of mechanical properties can be achieved from stiff thermoplastic-like to soft rubber-like materials. For the samples fabricated for this study, we tuned the process to realize a material with an initial shear modulus $\mu = 14.5$ MPa. The dimensions of the fabricated samples (as measured with a caliper) are shown in table A.1, and all fabricated lattices had depth

(through thickness) $H = 40$ mm.

A.3.2 Testing

All samples were tested using an Instron 5969 with a compression speed of 0.2 mm/min in order to allow material viscoelastic relaxation, thus achieving the material's fully elastic behavior. Note that the specific compression speed was determined by testing similar structures at different loading rates until the stress-strain curve achieved a rate independent solution.

To test the response of the specimens under uniaxial compression, we used standard compression plates with a 50 kN load cell. The response under bending was also characterized using a 3-point bend test mount and a 500 N load cell. Three specimens of each design were tested separately. The printing accuracy is reported in table A.1 as the measured mean for all 3 specimens in each of the components of the structure. The ideal expected values for each of the respective parameters are provided in table A.1. While similar results were obtained regardless of whether the models were loaded parallel or perpendicular to the print direction, for experimental consistency all tests were performed with models oriented parallel to the print direction. All specimens used a compression speed of 0.2 mm/min in order to allow material visco-elastic portion to relax, thus achieving the material's fully elastic behavior. The specific compression speed was determined by testing various similar structures at different rates until the stress-strain curve achieves a rate independent solution.

	Design A	Design B	Design C	Design D	Optimal Design
<i>Total Length (Test Dir.)</i> [mm]	93.29 [93]	93.45 [93]	93.47 [93]	93.25 [93]	93.27 [93]
<i>Total Length (Non-Test Dir.)</i> [mm]	93.52 [93]	93.31[93]	93.55 [93]	93.19 [93]	93.54 [93]
<i>Depth H</i> [mm]	39.98 [40]	40.06 [40]	40.19 [40]	40.10 [40]	40.25 [40]
<i>Top L</i> [mm]	14.7 [15]	14.95 [15]	14.93 [15]	14.96 [15]	15.02 [15]
<i>Top $T_{a,nd}$</i> [mm]	1.48 [1.5]	1.56 [1.5]	1.51 [1.5]	2.68 [2.56]	1.11 [1.03]
<i>Top $T_{a,d}$</i> [mm]	0.86 [0.75]	1.53 [1.5]	0.78 [0.75]	N/A	1.07 [1.08]
<i>Bottom L</i> [mm]	15.04 [15]	15.01 [15]	15.01 [15]	14.96 [15]	15.05 [15]
<i>Bottom $T_{a,nd}$</i> [mm]	1.55 [1.5]	1.57 [1.5]	1.57 [1.5]	2.69 [2.56]	1.11 [1.03]
<i>Bottom $T_{a,d}$</i> [mm]	0.85 [0.75]	1.61 [1.5]	0.86 [0.75]	N/A	1.08 [1.08]
<i>Weight</i> [g]	145.2	148.4	150.8	143.36	146.36

Table A.1: 3D Printed Model Caliper Sample Measurements. This table provides the caliper measurements averaged over $n = 3$ separate specimens for each design (values in black) as well as the expected values (bracketed values in red). All measurements reported were conducted prior to testing the samples.

A.3.3 Testing Slender Structure Three Point Bend Testing

Specimens were printed as slender structures consisting of 1 by 5.5 unit cells (2 by 11 square grid) with square spacing $L = 15$ mm and extruded depth $H = 40$ mm. The 3D printed specimens were placed individually on an Instron 5969 with a 3-point bend test mount using a 500 N load cell. If applicable, the filled cells (cells containing diagonal crossings) were aligned with the force points to magnify the effects of each design. Although, similar trends persist when experiments were conducted in the inverse alignment, namely when force points are applied to non-filled cells (cells containing no diagonal bracings). All specimens used an indenter speed of 0.2 mm/min in order to allow material visco-elastic time to fully relax. This speed was specified to maintain consistency with the block uniaxial testing experiments.

A.4 Finite Element (FE) Analysis

The finite element analyses presented in this article were conducted using *ABAQUS/Standard*. All models were constructed using 1D Timoshenko beam elements (ABAQUS element type B22) and all beam crossings were assumed to be welded joints. For each instance, seeding of the mesh was chosen to be at least 1/10 of the minimum beam length. The response of the material was captured using an incompressible Neo-Hookean material model with shear modulus $\mu = 14.5$ MPa. Due to small inconsistencies in the 3D printing process (table A.1), we adjusted the dimensions of the FE models accordingly by applying a mass correction based on data derived from the 3D-printed models in Main Text Figs. 2(f) and 4(b).

To reduce the computational cost, in most of our analyses, we took advantage of the periodicity of the structures and investigated their response using the unit cells shown in figure A.6. To subject

the unit cells to a macroscopic deformation gradient $\bar{\mathbf{F}}$ periodic boundary conditions were imposed on all cell boundaries by enforcing^[106,107]

$$\mathbf{u}_\alpha^{A_i} - \mathbf{u}_\alpha^{B_i} = (\bar{\mathbf{F}}_{\alpha\beta} - \delta_{\alpha\beta})(\mathbf{X}_\beta^{A_i} - \mathbf{X}_\beta^{B_i}), \quad i = 1, 2, \dots, K \quad (\text{A.37})$$

where $\delta_{\alpha\beta}$ is the Kronecker delta, $\mathbf{u}_\alpha^{A_i}$ and $\mathbf{u}_\alpha^{B_i}$ ($\alpha = 1, 2$) are displacements of points periodically located on the boundary of the unit cell. Moreover, $\mathbf{X}_\alpha^{A_i}$ and $\mathbf{X}_\alpha^{B_i}$ ($\alpha = 1, 2$) are the initial coordinates of points periodically located on the boundary of the unit cell and K denotes the number of pairs of nodes periodically located on the boundary of the unit cell. Note that the components of $\bar{\mathbf{F}}$ can be conveniently prescribed within the finite element framework using a set of virtual nodes. The corresponding macroscopic first Piola-Kirchhoff stress is then obtained through virtual work considerations^[106,107]. To subject the structures to uniaxial compression, we prescribed

$$\bar{\mathbf{F}} = \begin{bmatrix} \text{UNSET} & 0 \\ 0 & 1 + \epsilon_y \end{bmatrix}, \quad (\text{A.38})$$

where ϵ_y is the macroscopic applied strain. Moreover, in order to investigate the structure's response for different loading directions, we rotated the unit cell model by an angle θ and re-applied the above periodic boundary conditions using the rotated geometry coordinates. To determine the linear stiffness for the infinite structures we performed a small strain linear elastic analysis. For all buckling analyses, we performed a linear stability buckling analysis (*BUCKLING command in ABAQUS input file). Since buckling may alter the periodicity of the structure, we considered super cells consisting of $M \times M$ undeformed RVEs with $M \in [1, 10]$ subjected to periodic boundary conditions and calculated the critical strain for each of them. The critical strain of the infinite pe-

periodic structure was subsequently defined as the minimum critical strain on all considered super cells. The results reported in figure A.7 show that for *Design A-C* the critical strain is identical for all considered values of M , indicating that the structure undergoes a local (microscopic) instability with wavelength corresponding to the size of the RVE. *Design D*, on the other hand, undergoes a global (macroscopic) instability, as the minimum critical strain is observed for $M = 10$ (figure A.8).

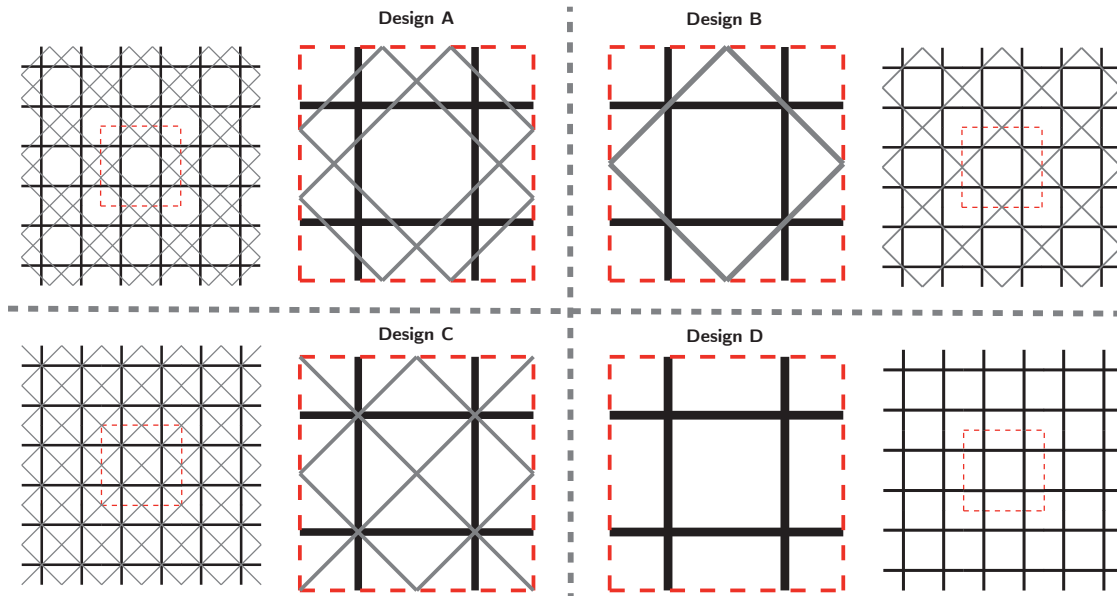


Figure A.6: RVE used for the different designs. Schematics of the RVEs used for *Design A-D*. Periodic boundary conditions are applied on the nodes that intersect with the red dashed line.

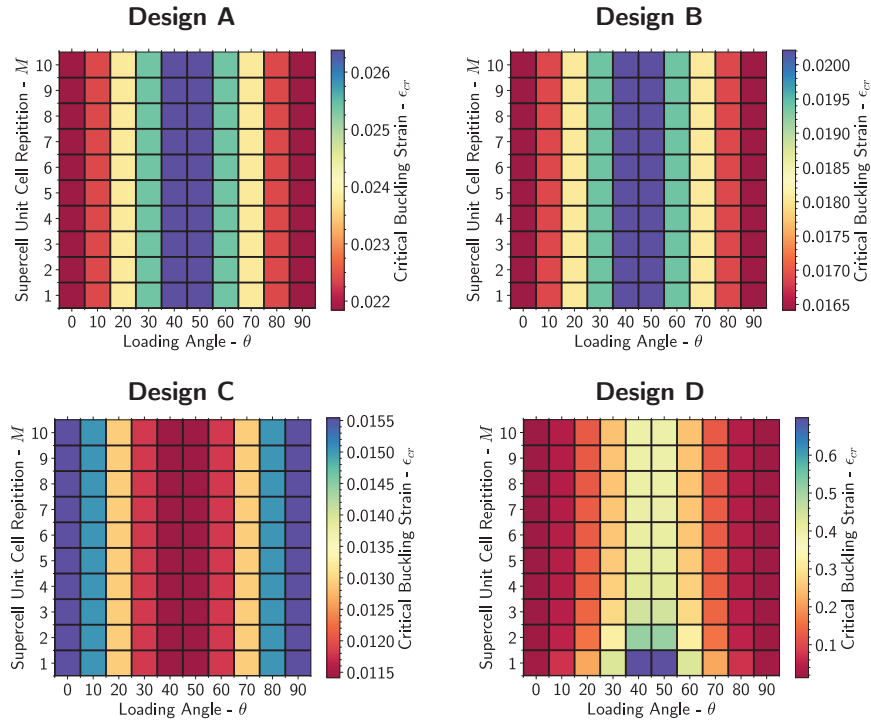


Figure A.7: Global versus local instabilities. In each contour plot, we report the critical strain as a function of θ and the size of the super cell. For each of the simulations, periodic boundary conditions are applied along the outer perimeter of the $M \times M$ structure. This plot conveys that for *Designs A-C* the prominent buckling mode is the local mode, whereas for *Design D*, the prominent mode is a global mode. Choosing a sufficiently large M allows *Design D* to converge to a finite value for each θ .

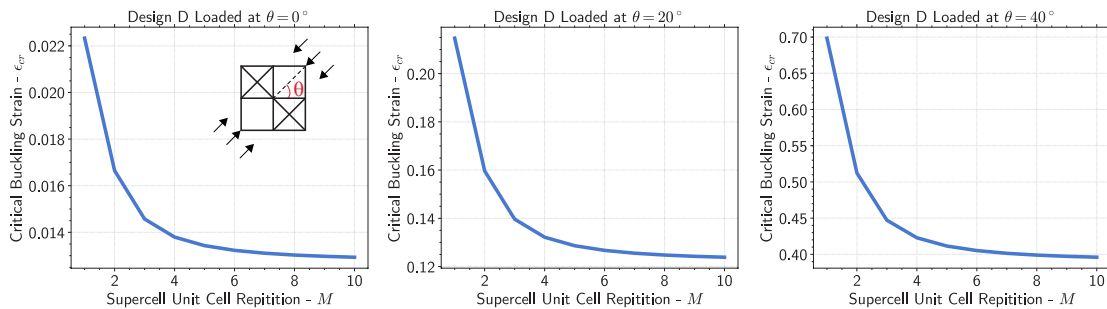


Figure A.8: Critical strain for *Design D* at three selected loading angles. As the number of minimum RVEs M considered increases, the value for the critical buckling strain asymptotically approaches a constant.

A.4.1 Local and Global Instabilities

Local versus global instabilities are driven by the fundamental wavelength of a particular structural instability. These wavelengths are typically unknown at first and can be fictitiously constrained within the length-scale of a periodic unit cell simulation. As a result, simulations typically overestimate (provide a higher than correct value) the critical buckling strength of a structure. To address this potential concern, we created simulations for each of the considered geometries where we consider an $M \times M$ minimum RVE unit cell, where M is the number of uni-cells. The results portrayed in figure A.7 show that for *Design A-C* no matter how large we make the periodic structure, we still obtain the same result, indicating that the structure undergoes a local (microscale) instability of the size of the minimum RVE unit cell. *Design D*, on the other hand, undergoes a global (macroscale) instability as evident in figure A.7 by the buckling strain dependence on the number of cells M . Therefore, to obtain the value for all θ in *Design D*, we analyze for select θ what is the value M necessary to achieve convergence in obtaining the macro-scale instability. That value as determined in figure A.8 is $M = 10$.

For infinite structures modeled using period boundary conditions, it is important to realize the distinction between local instabilities (i.e. instabilities with wavelength that are of the order of the size of the unit cell) and global instabilities (i.e. instabilities with large wavelengths in comparison to the size of the unit cell). In order to capture any global instabilities potentially missed by using the minimum RVE, we further develop our period numerical studies to include RVEs that tessellate the unit cells presented in section A.2. For all designs, we increase the domain size by tessellating up to 20×20 unit cells (creating a base grid of 40×40 square cells). For *Designs A-C*, the critical buckling strain and modes do not change for larger unit cells suggesting that there does not exist a

global instability. Whereas, for *Design D*, as we increase the domain size (add more unit cells to the tessellation), the instability wavelength continues to grow with the size of the domain, suggesting a global macroscopic instability that depends on the size of the domain. The critical buckling strain is inversely proportional with the RVE size and approaches 0 in the limit that the RVE size approaches infinity. It is well known and documented that *Design D* is unstable when loaded in uniaxial compression.

A.4.2 Additional numerical results

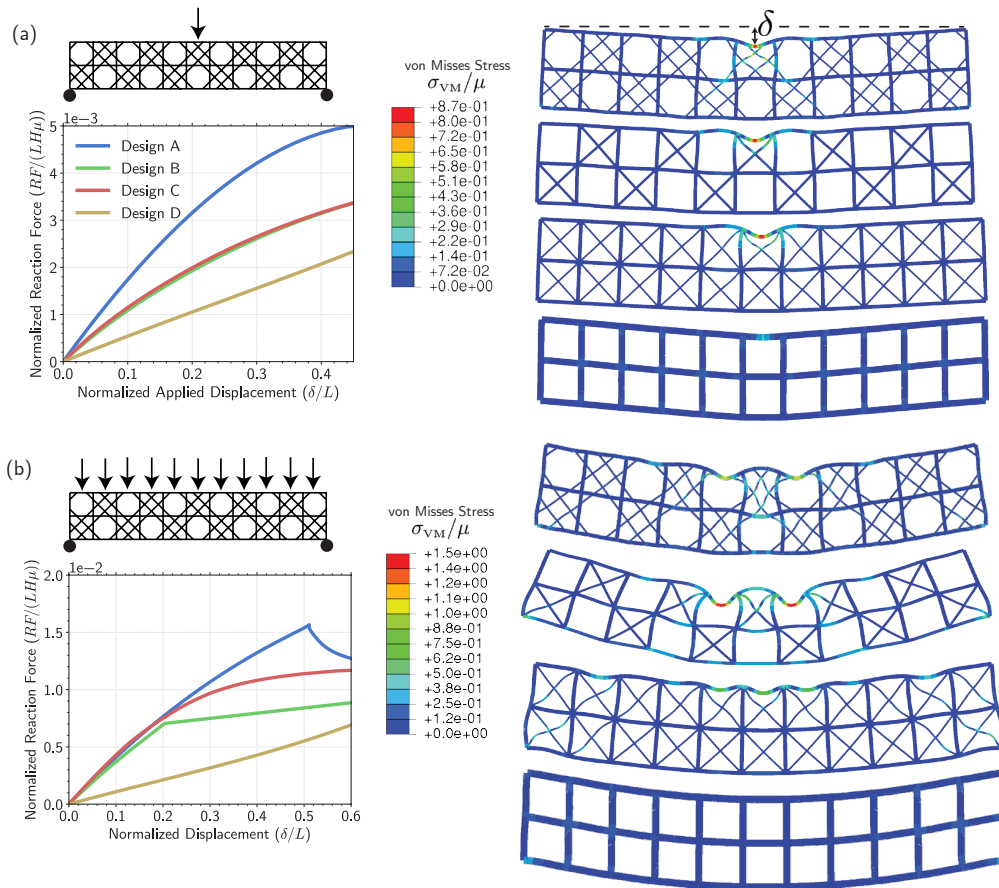


Figure A.9: Mechanical response for different loading conditions. For all cases presented in this figure, we consider a structure with 11×2 cells (5.5 RVEs) and hinged boundary conditions applied to cells *with* diagonal reinforcements. (a) In this case, a point deflection δ is applied to the top center of the structure while the bottom outside corners have constrained deflections, but unconstrained rotation. The normalized reaction force is plotted as a function of the δ for the four considered designs. Moreover, on the right we show numerical snapshots of the four designs for $\delta/L = 0.45$. The colors in these pictures provide a measure of the normalized von Mises stress. (b) In this case a distributed load is applied across the top of the structure while the bottom outside corners have constrained displacements, but unconstrained rotation. The normalized total reaction force is plotted as a function of the deflection for the four considered designs. On the right we show numerical snapshots of the four designs for $\delta/L = 0.6$, where δ is the vertical deflection of the top mid-point from the undeformed configuration. The colors in these pictures provide a measure of the normalized von Mises stress.

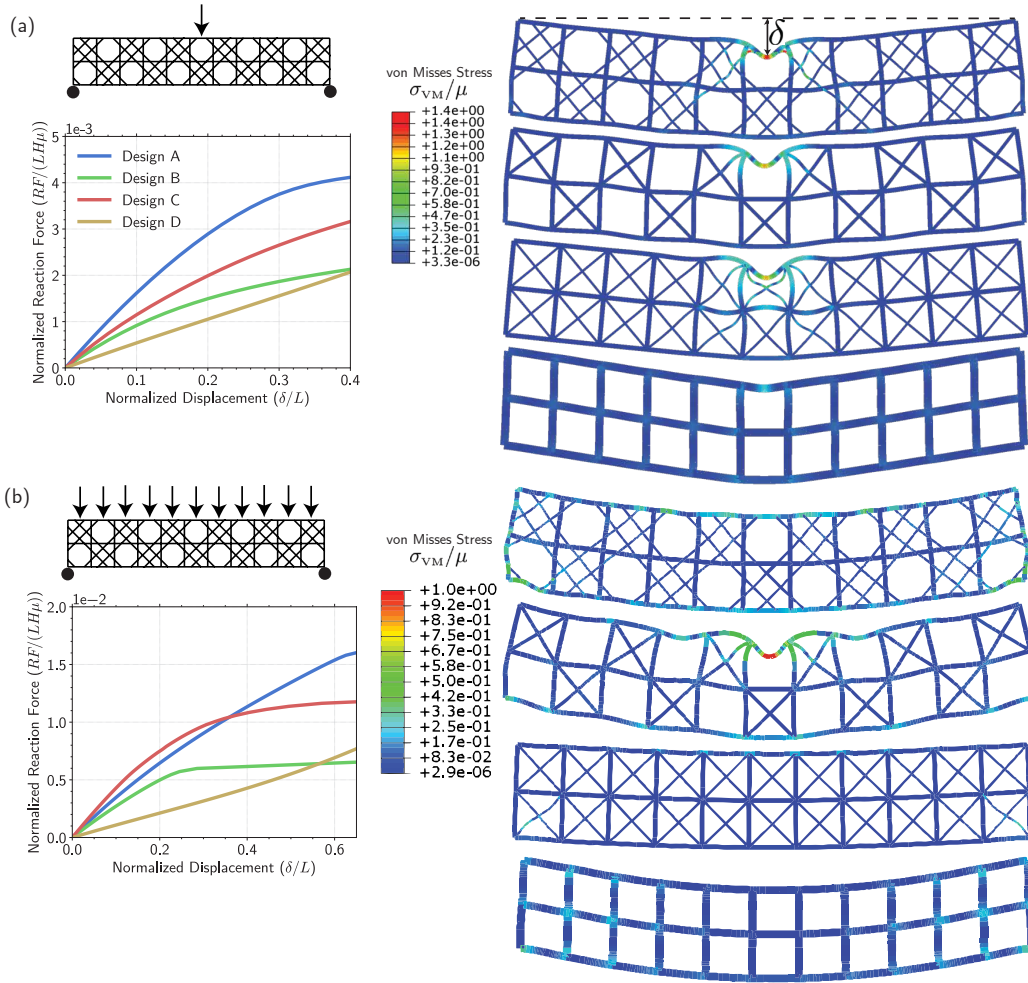


Figure A.10: Mechanical response for different loading conditions. For all cases presented in this figure, we consider a structure with 11×2 cells (5.5 RVEs) and hinged boundary conditions applied to cells *without* diagonal reinforcements. (a) In this case, a point deflection δ is applied to the top center of the structure while the bottom outside corners have constrained deflections, but unconstrained rotation. The normalized reaction force is plotted as a function of the δ for the four considered designs. Moreover, on the right we show numerical snapshots of the four designs for $\delta/L = 0.45$. The colors in these pictures provide a measure of the normalized von Mises stress. (b) In this case a distributed load is applied across the top of the structure while the bottom outside corners have constrained displacements, but unconstrained rotation. The normalized total reaction force is plotted as a function of the deflection for the four considered designs. On the right we show numerical snapshots of the four designs for $\delta/L = 0.6$, where δ is the vertical deflection of the top mid-point from the undeformed configuration. The colors in these pictures provide a measure of the normalized von Mises stress.

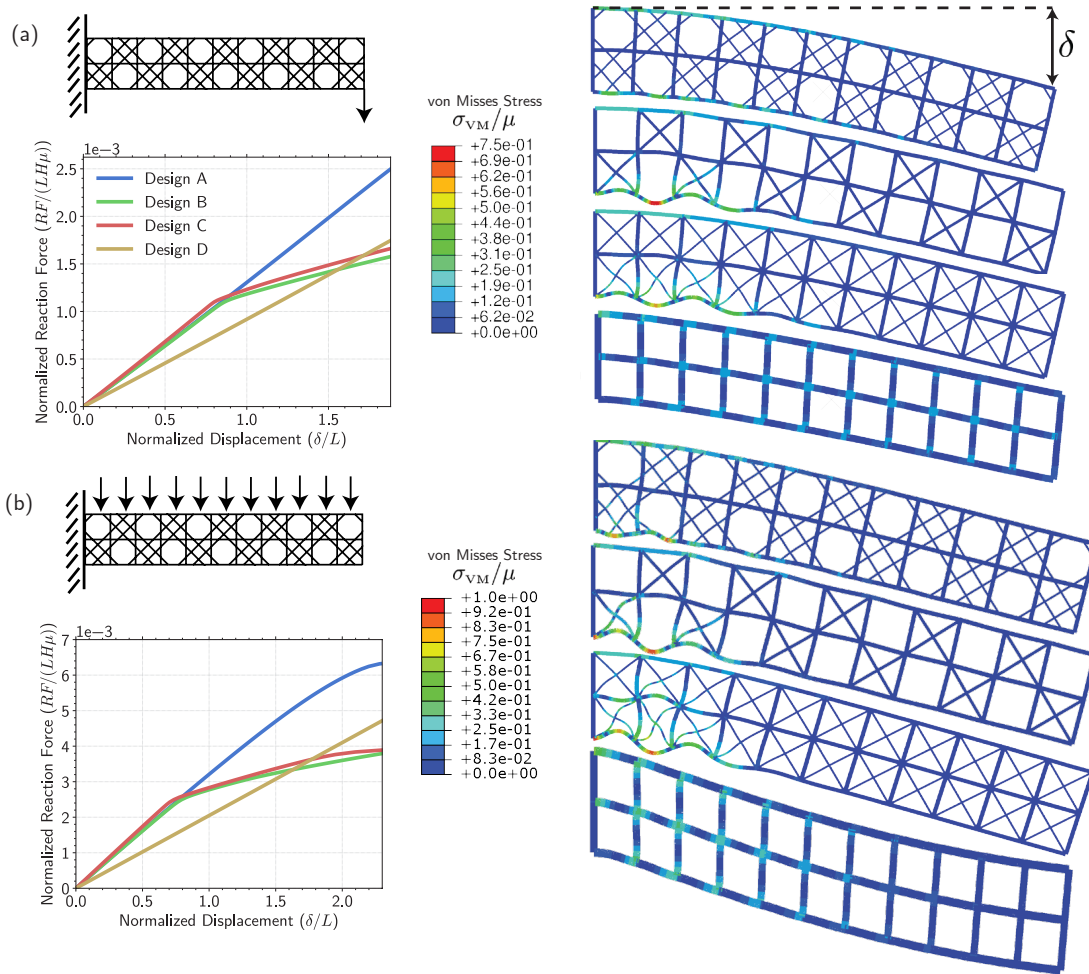


Figure A.11: Mechanical response for different loading conditions. For all cases presented in this figure, we consider a long slender realization of each design consisting of 11×2 cells (5.5 RVEs). (a) In this case, a point deflection δ is applied to the bottom right of the structure while the left edge of the structure is fixed. The normalized total reaction force is plotted as a function of the deflection for the four considered designs. Moreover, on the right we show numerical snapshots of the four designs for $\delta/L = 1.9$. The colors in these pictures provide a measure of the normalized von Mises stress. (b) In this case a distributed load is applied across the top of the structure while the left edge of the structure is fixed. The normalized total reaction force is plotted as a function of the deflection for the four considered designs. On the right we show numerical snapshots of the four designs for $\delta/L = 2.3$, where δ is the vertical deflection of the top right edge-point from the undeformed configuration. The colors in these pictures provide a measure of the normalized von Mises stress.

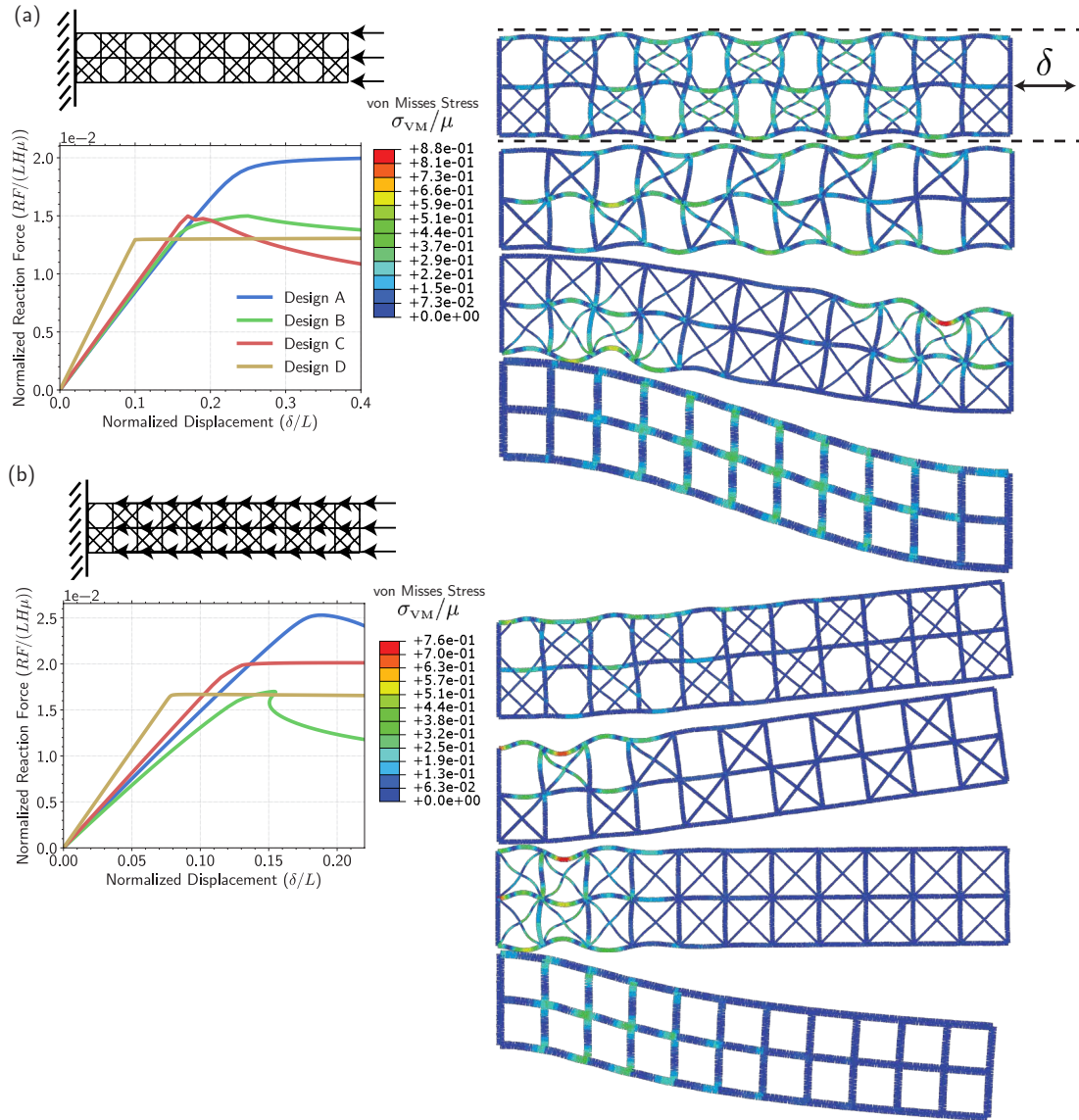


Figure A.12: Mechanical response for different loading conditions. For all cases presented in this figure, we consider a long slender realization of each design consisting of 11×2 cells (5.5 RVEs). (a) In this case a deflection δ is applied to the right edge of the structure while the left edge of the structure is fixed. The normalized total reaction force is plotted as a function of the applied deflection for the four considered designs. Moreover, on the right we show numerical snapshots of the four designs for $\delta/L = 0.4$. The colors in these pictures provide a measure of the normalized von Mises stress. (b) In this case a distributed load is applied across each level of the structure while the left edge of the structure is fixed. The normalized total reaction force is plotted as a function of the deflection for the four considered designs. On the right we show numerical snapshots of the four designs for $\delta/L = 0.22$, where δ is the horizontal deflection of the right mid-point from the undeformed configuration. The colors in these pictures provide a measure of the normalized von Mises stress.

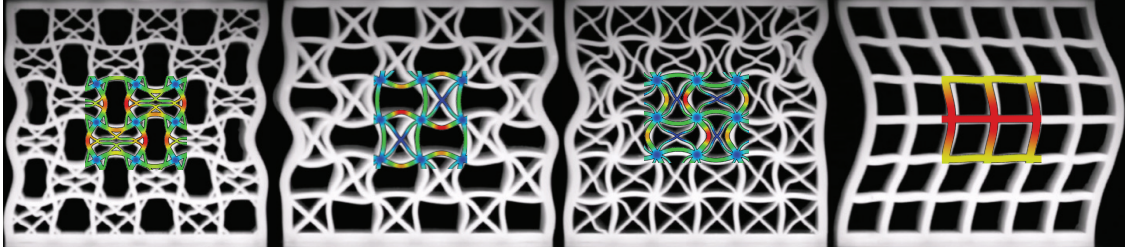


Figure A.13: Comparison between experimental and numerical results. This figure shows experimental snapshots of the experimental specimens at an applied 8% compressive strain overlaid with a cutout of the representative deformation predicted by our FE analyses. The close agreement between the experiments and simulations suggests that the FE simulations are accurately capturing the physical deformation of the specimens.

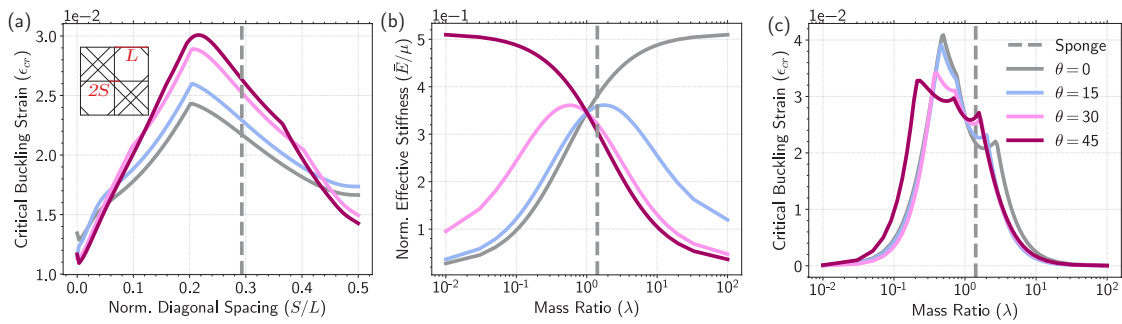


Figure A.14: Effect of diagonal spacing and mass ratio on the response of *Design A* with rectangular cross-section. (a) Evolution of the critical strain as function of the spacing between diagonals. (b) Evolution of structural stiffness as a function of the mass ratio $\lambda = V_{nd}/V_d$. (c) Evolution of critical strain as a function of the mass ratio λ . For each of the plots, the gray dashed vertical line indicates the parameter of *Design A*. These results demonstrate that *Design A*, the sponge design, is very close to the optimal one, when considering each parameter individually. All designs are characterized by the same total volume.

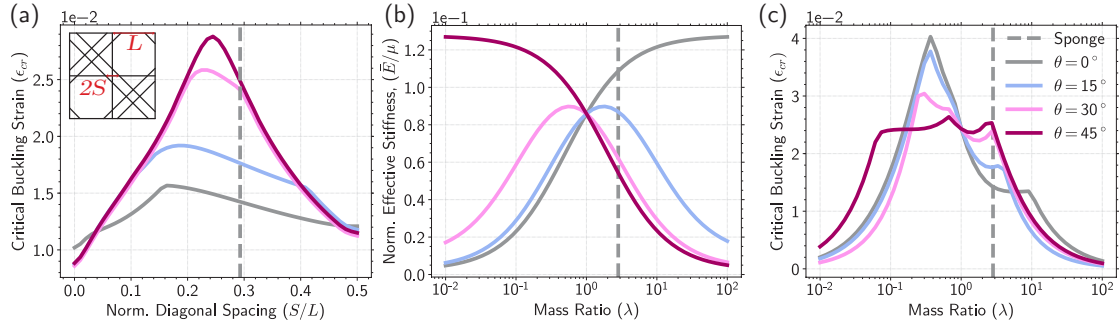


Figure A.15: Effect of diagonal spacing and mass ratio on the response of *Design A* with circular cross-section. (a) Evolution of critical strain as function of the spacing between diagonals. (b) Evolution of structural stiffness as a function of the mass ratio $\lambda = V_{nd}/V_d$. (c) Evolution of critical strain as a function of the mass ratio λ . For each of the plots, the gray dashed vertical line indicates the parameter of *Design A*. These results demonstrate that the shape of the cross-section does not have a significant role, as these results are similar to those presented in figure A.14 for a lattice with rectangular cross-section. All designs are characterized by the same total volume.

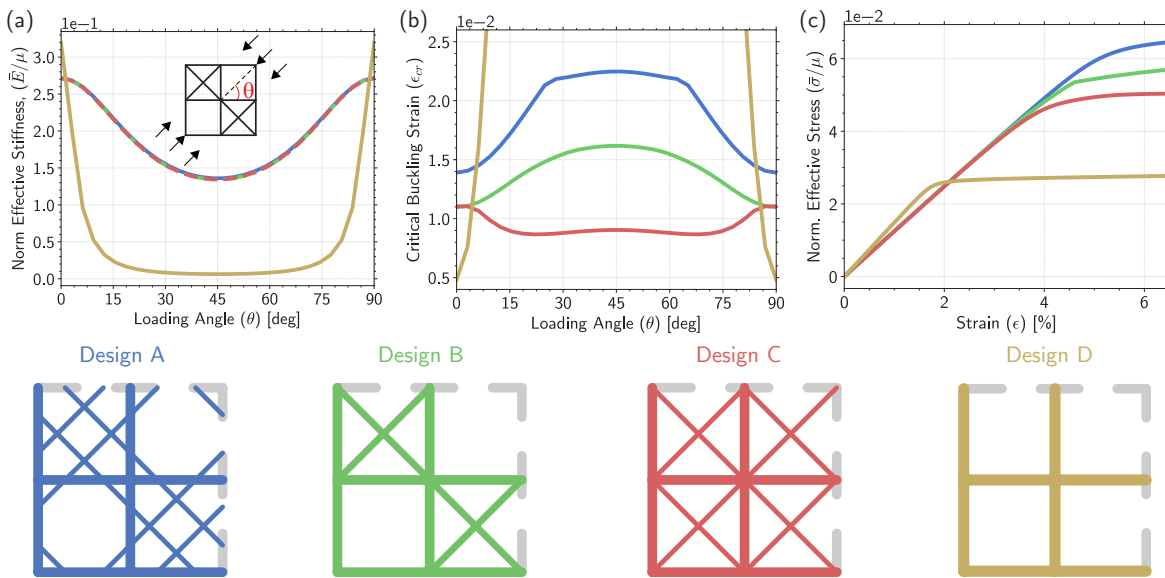


Figure A.16: Response of *Design A-D* with circular cross-section. (a) Evolution of the structural stiffness as a function of loading angle θ for lattices of infinite size. (b) Evolution of the effective buckling stress for the different lattice designs as a function of loading angle θ . Results are obtained by simulating a super-cell with 10 by 10 units and periodic boundary conditions. (c) Numerically predicted stress-strain curves for the 4 considered lattices when compressed with $\theta = 0$. For all plots, the color of the line corresponds to the respective design color depicted on the bottom.

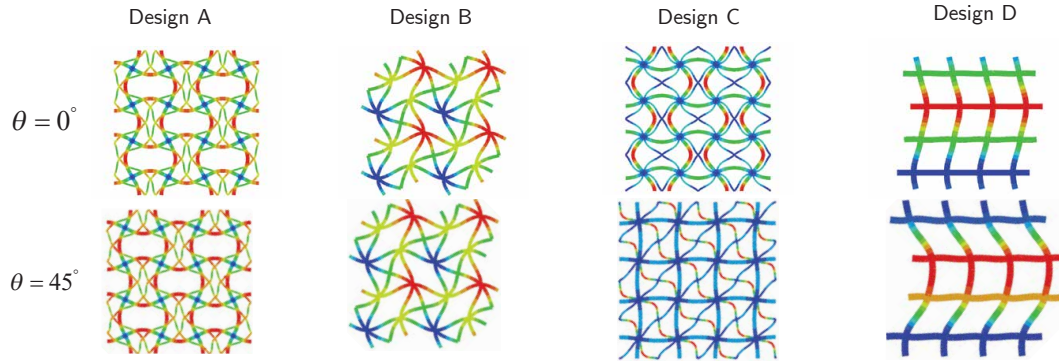


Figure A.17: Critical modes of *Design A-D* at $\theta = 0^\circ$ and $\theta = 45^\circ$. These critical buckling modes were calculated using a 10 by 10 super-cell and the snapshots shown here are the center 2x2 cells of the full 10x10 model. *Designs A-B* in this figure exhibit a similar deformation pattern when loaded at 0° or 45° . However, for *Design C-D*, different buckling patterns are triggered when loaded at 0° and 45° .

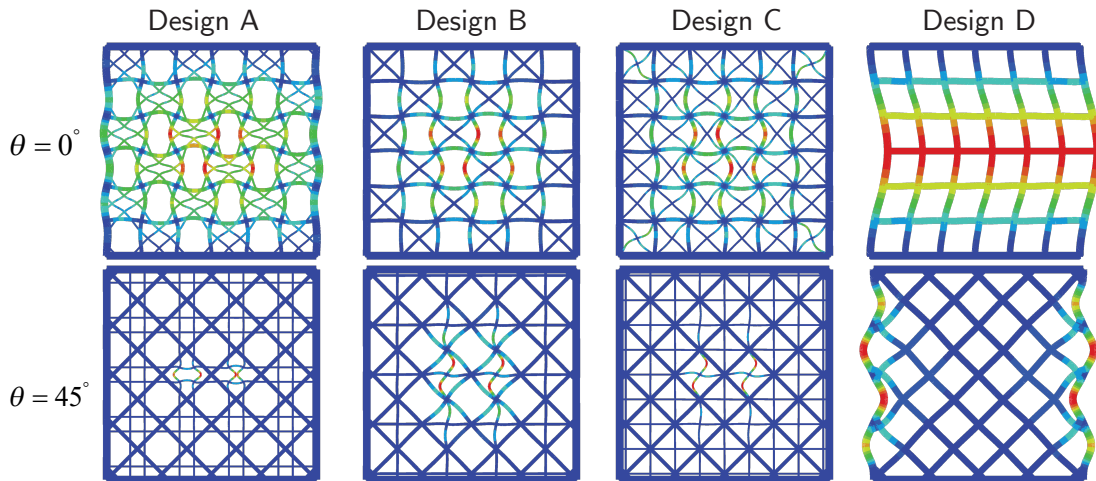


Figure A.18: Modes of finite size structure comprised of 3x3 unit cells. This figure shows the critical buckling modes obtained for finite geometries for *Design A-D* loaded in uniaxial compression. The top row corresponds to a structure angled at 0° , as in the experiments *A-D*. The second row corresponds to the same structure however rotated by 45° and cut to maintain the same size as the row above. Each column in this figure corresponds to a different design. For each of the geometries, a slightly thicker frame is constructed to localize most of deformation away from the edges of the structure. These results convey that the diagonally reinforced geometries are not susceptible to edge effects when using at least 3 unit cells, whereas the non-diagonally reinforced structure is more susceptible to edge effects.

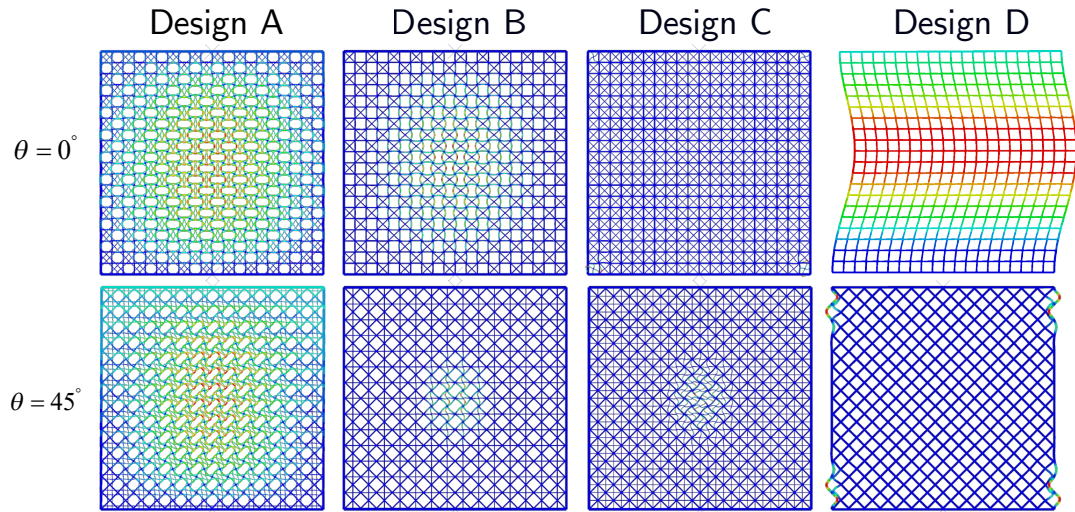


Figure A.19: Modes of finite size structure comprised of 10x10 unit cells. This figure shows the critical buckling modes obtained for finite geometries of *Design A-D* loaded in uniaxial compression. The top row corresponds to a structure angled at 0° , as considered in the experiments. The second row corresponds to the same structure however rotated by 45° and cut to maintain the same size as the row above. Each column in this figure corresponds to a different design. For each of the geometries, a slightly wider frame is constructed to minimize edge effects.

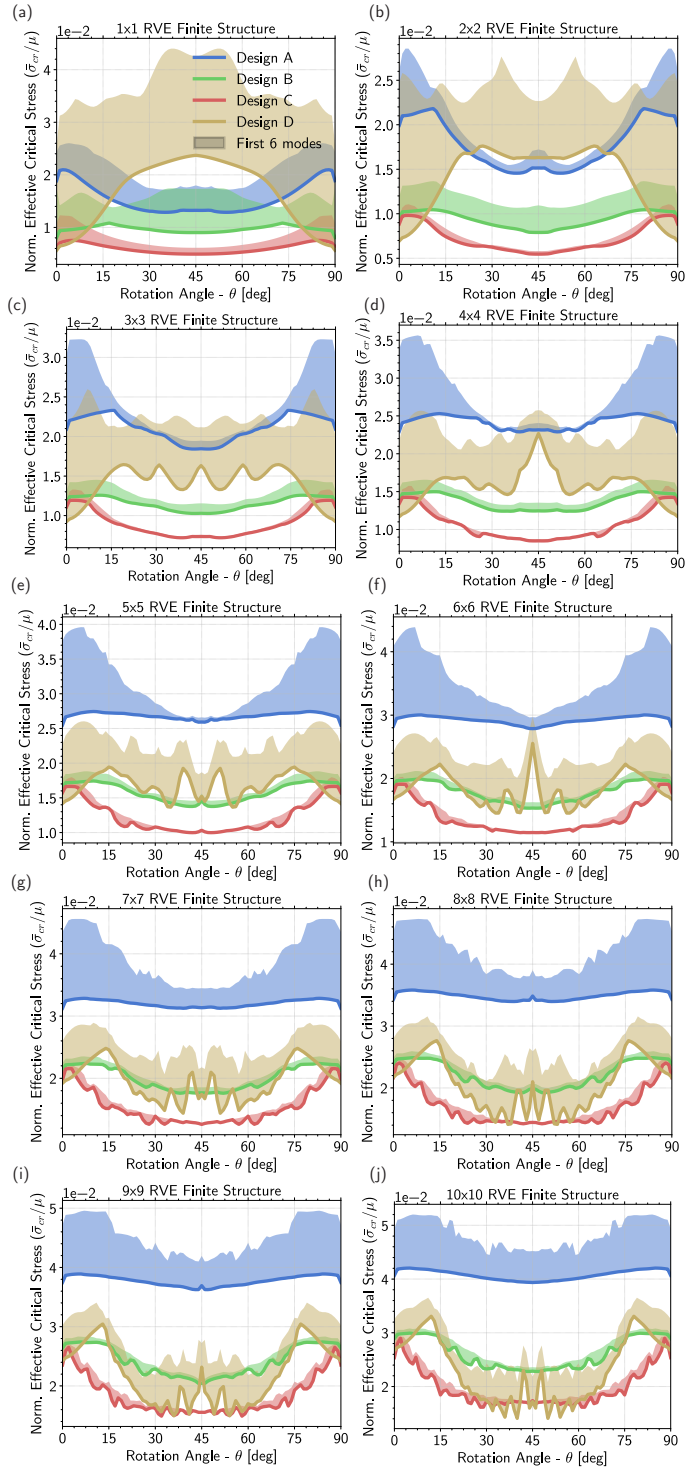


Figure A.20: Effect of sample size on critical stress. Evolution of the effective buckling stress as a function of the loading angle θ for finite-size lattice structures comprising M by M unit cells, where M ranges from (a) 1 to (j) 10. The shaded parts in (a) - (j) represent the lowest six buckling modes range. All plots provide a clear indication on the superior performance of *Design A* when comparing to *Designs C-D*, when $M > 2$.

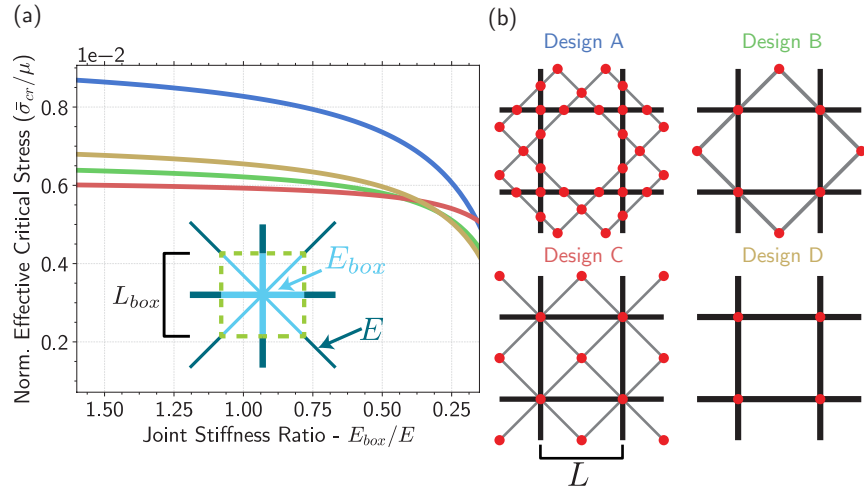


Figure A.21: Effect of joint stiffness analysis on critical stress. To evaluate the influence of the joints on the effective buckling stress of Designs A-D we conduct FE analysis on a period unit cell with modified stiffness on elements near the joints. In particular, we set the material stiffness to E_{box} for the elements within a box of edge length $L_{box} = 0.02L$ (see inset schematic in (a)). (a) Evolution of the normalized effective critical stress for varying the joint stiffness ratio E_{box}/E . (b) Schematic of Design A-D unit cells with the location of the joints highlighted by red dots.

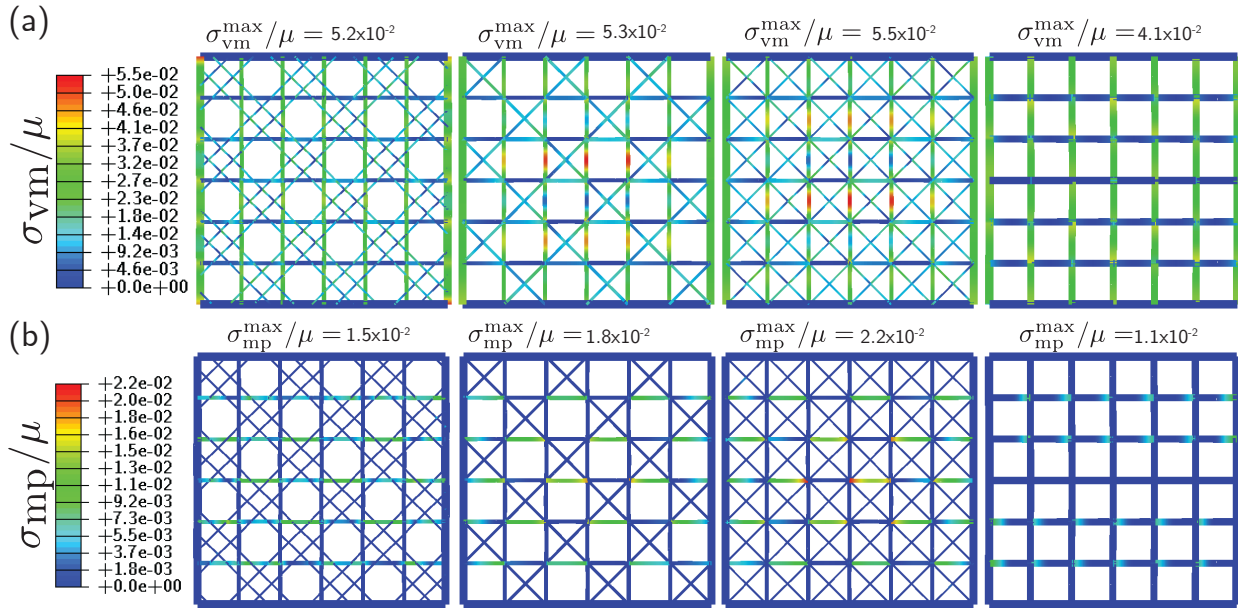


Figure A.22: Stress Analysis. Numerical snapshots extracted from non-linear FE analysis (with first mode imposed imperfection) at an imposed strain $\varepsilon = 0.001$. (a) The color indicates the normalized von Mises stress σ_{vm} with the maximum value for each structure indicated above each figure. (b) The color indicates the normalized maximum principle stress σ_{mp} with the maximum value for each structure indicated above each figure.

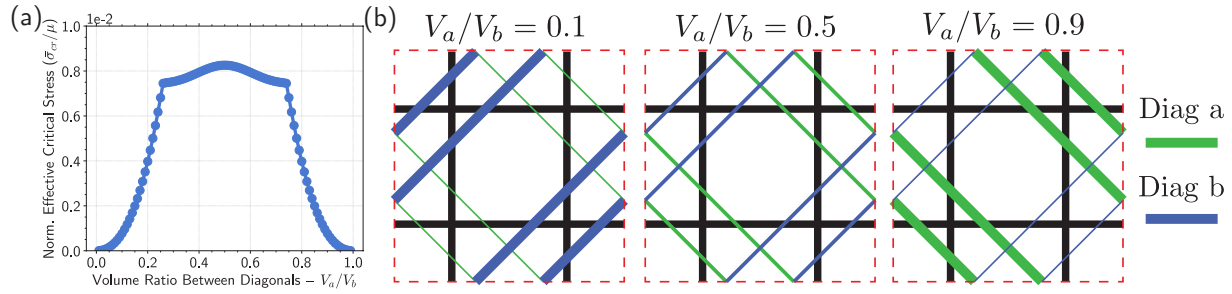


Figure A.23: Effect of disorder on critical stress. To evaluate the influence of disorder on the effective buckling stress of *Design A*, we conduct FE analysis on a period unit cell on which we vary the mass allocated between diagonals going in different directions. For all analysis presented, the total volume allocated between diagonals and non-diagonals remains constant, namely $\lambda = \sqrt{2}$. V_a/V_b defines the ratio between the volume allocated to the two families of diagonals (with $V_a + V_b = V_{nd}/\sqrt{2}$). (a) Evolution of the effective buckling stress as a function of V_a/V_b for $\theta = 0$. We find that for $0.25 < V_a/V_b < 0.75$ disorder has a minor effect on the effective buckling stress. (b) Schematics of selected unit cell with different diagonal volume allocations V_a/V_b .

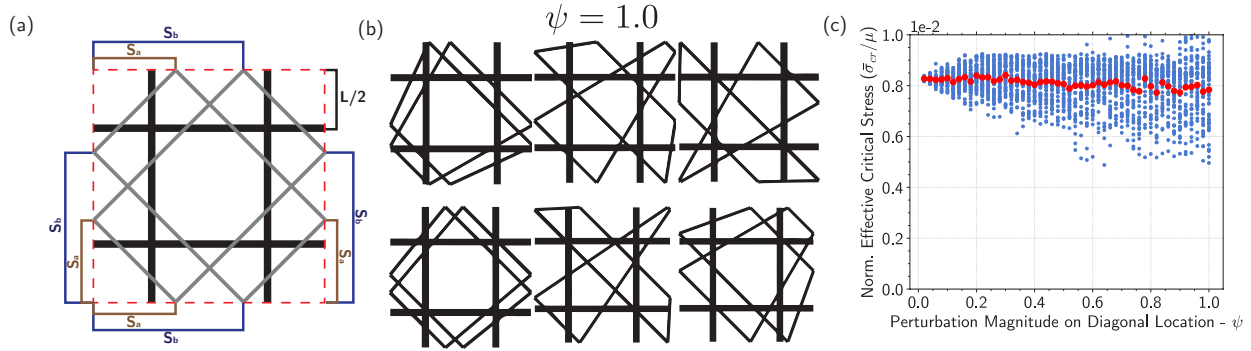


Figure A.24: Effect of disorder on critical stress. To evaluate the influence of disorder on the effective buckling stress of *Design A* we conduct FE simulations on a periodic unit cell in which we vary the location and orientation of individual diagonals, while maintaining periodicity of the structure. For all analysis presented, the total volume of the diagonals remains constant and equal to $V_{nd}/\sqrt{2}$. (a) Schematic illustrating the spacing S_a and S_b , defining the position of each diagonal. (b) Schematics of unit cell with varying S_a and S_b (with $S_a, S_b \in [0, 2L]$). (c) Effective buckling stress for 2,500 unit cell simulations, in which we perturb the sponge strut spacings S_a and S_b using a Gaussian \mathcal{N} with mean $\mu = 0$, standard deviation $\sigma = 0.3$ and magnitude ψ , namely, $S_a/L = 1 - 1/(\sqrt{2} + 2) + \psi\mathcal{N}(0, 0.3)$ and $S_b/L = 1 + 1/(\sqrt{2} + 2) + \psi\mathcal{N}(0, 0.3)$. The red markers indicate the mean for each considered ψ containing $n = 50$ simulations per discrete value of ψ . We find that the applied perturbation does not alter the mean effective critical stress and that the variation of $\bar{\sigma}_{cr}$ is bounded between $0.6 \times 10^{-2}\mu$ and $1.0 \times 10^{-2}\mu$.

A.5 Optimization Analysis

In an effort to identify the diagonal reinforcement resulting in a square lattice with the highest critical load, we used a Python implementation of the Covariance Matrix Adaptation Evolution

Strategy (CMA-ES)^[162]. CMA-ES is an evolutionary algorithm that is used to solve optimization problems by iteratively solving several forward problems to adjust a covariance matrix of the solution. Since it is a derivative free algorithm, CMA-ES is well suited for optimization problems of high dimensionality and non-linear parameter topology. In this study we used CMA-ES to identify

- the number of diagonals, N
- the volume ratio of non-diagonal to diagonal members, $\lambda = V_{nd}/V_d$. Note that, since for a lattice with N diagonal members

$$V_{nd} = 8T_{nd}LH, \quad (\text{A.39})$$

$$V_d = 4\sqrt{2}NT_dLH, \quad (\text{A.40})$$

for a given λ T_{nd} and T_d are given by

$$T_{nd} = \frac{1}{2} \frac{\lambda}{1+\lambda} (0.2L + 0.1\sqrt{2}L), \quad (\text{A.41})$$

$$T_d = \frac{1}{\sqrt{2}} \frac{1}{N(1+\lambda)} (0.2L + 0.1\sqrt{2}L), \quad (\text{A.42})$$

where we have enforced equation A.1 and equation A.9.

- the separation between each even set of diagonals, S_i for $i \in [1, 7]$ (figure A.25)

resulting in a lattice structure with the largest critical load. For such an optimization problem, the number of optimization variables increased with the number of diagonals incorporated in the model (i.e. the total number of parameters are $1 + \frac{1}{2}(N - (N \bmod 2))$ for a given optimization instance with N number of diagonals). In all of the runs we assumed that all diagonals are oriented at 45° with respect to the non-diagonal members and that V_d and V_{nd} were distributed equally among the diagonal and non-diagonal elements, respectively. Furthermore, to ensure the symmetry, we assumed that $S_{2i-1} = S_{2i}$ ($i = 1, 2, \dots, N/2$) if N is an even number and $S_1 = 0$ and $S_{2i-1} = S_{2i}$ ($i = 2, 3, \dots, (N-1)/2$) for odd values of N (figure A.25).

The algorithm's initial values were chosen to be in the center of the design space, namely, $\lambda = 1$ and diagonal separation for the even set of diagonals $S_i = 0.5L$. The covariance matrix was initialized uniformly with a standard deviation half of the domain space, which was normalized and constrained to remain between 0 and 1. The optimization was evaluated in a uniaxial loading condition aligned parallel to the vertical elements with a population size of 30.

For the optimization results presented in the Main Text, we sought to maximize the critical buckling load of a finite size structure using a single objective target function. The resultant parameter values from the optimization can be found in table A.2 and a convergence analysis for the case of $N = 2$ can be found in figure A.26. Note that we also performed the same optimization analysis on an infinite periodic structure and the obtained results are shown in figure A.27, and table A.3.

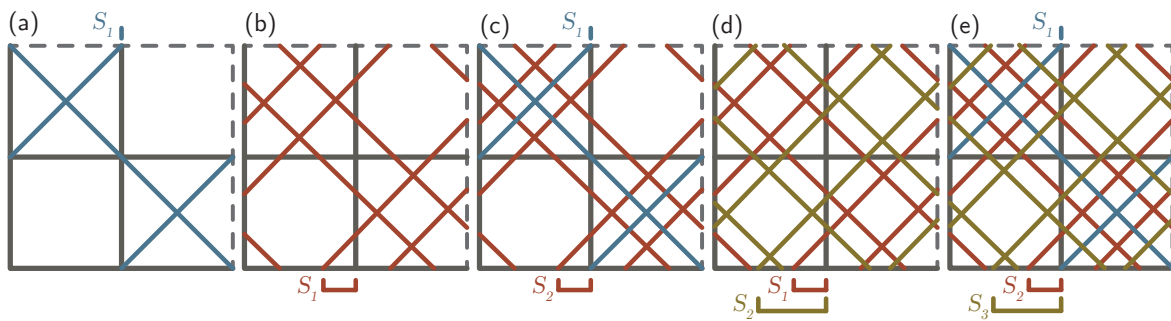


Figure A.25: Schematic. Schematics highlighting the geometric parameters considered in our optimization analysis.

	λ	S_1	S_2	S_3	S_4
$N = 1$	3.1890	0			
$N = 2$	0.6778	0.1800			
$N = 3$	0.8028	0	0.3044		
$N = 4$	0.7640	0.1912	0.3720		
$N = 5$	0.3874	0	0.3881	0.7811	
$N = 6$	0.5036	0.1910	0.5189	0.8712	
$N = 7$	0.3561	0	0.2899	0.5512	0.8779

Table A.2: Optimal 3×3 finite-sized structures. Geometric parameters defining the 3×3 structures with highest critical stress identified by CMA-ES for different numbers of diagonals. In each row we report the optimal parameter identified for a given number of diagonals N . For odd N , S_1 is constrained to 0, meaning it is not allowed to move from the non-diagonal elements junction. As the number of diagonals is increased λ decreases, indicating that the algorithm allocates more mass to the diagonal elements.

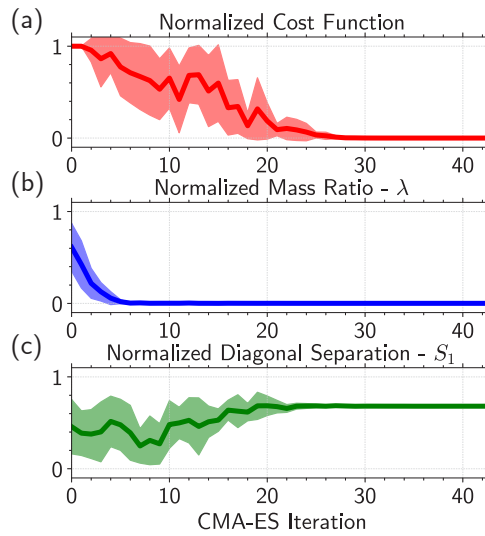


Figure A.26: Evolution of the objective function and design parameters during CMA-ES iterations. This figure shows the evolution of (a) the cost function, (b) the normalized mass ratio λ , and (c) the normalized diagonal separation S_1 over the course of each iteration of the optimization analysis for a lattice with $N = 2$. The solid line represents the mean value for the evolutionary optimization iteration (with population size $n = 30$ samples per iteration) and the shaded bounds represent the standard deviation from the mean. In this figure, it is apparent that the optimal value for λ is quickly identified by the algorithm.

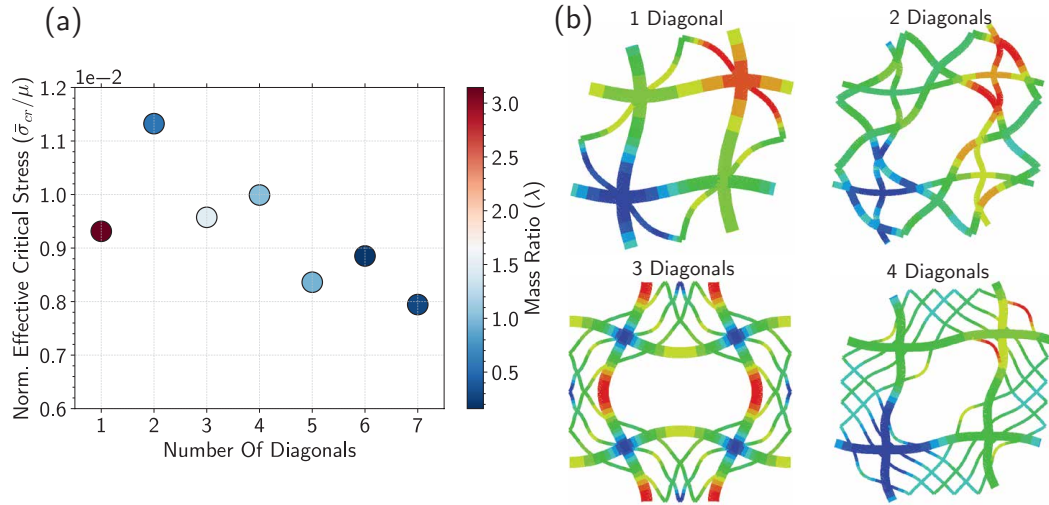


Figure A.27: Optimization analysis for infinite periodic structures. (a) Optimal value of critical buckling stress for varying number of diagonals. The color of each point represents the optimal mass ratio λ . (b) Optimal deformed geometries for designs including one to four diagonals. The color in each structure represents the magnitude of the displacement.

	λ	S_1	S_2	S_3	S_4
$N = 1$	3.1454	0			
$N = 2$	0.5614	0.3390			
$N = 3$	1.4784	0	0.2440		
$N = 4$	1.0151	0.0989	0.3358		
$N = 5$	0.9509	0	0.1733	0.3260	
$N = 6$	0.2009	0.2628	0.5827	0.8881	
$N = 7$	0.2962	0	0.4197	0.6917	0.9126

Table A.3: Optimal structures of infinite extent. Geometric parameters defining the infinite structures with highest critical stress identified by CMA-ES for different numbers of diagonals. Each column of the table corresponds to the optimal value of a parameter. Each row corresponds a determined N number of diagonals. For odd N , S_1 is constrained to 0, meaning it is not allowed to move from the non-diagonal elements junction. λ on average decreases as a function of N , which as expected, means the algorithm is allocating more volume to the diagonals as they are being spread too thin. The distribution of S as a function of N shows that the algorithm is attempting to evenly distribute the diagonal spacing, such that the length of the vertical elements without diagonal bracing is kept the shortest.

B

Supplementary Information: Mechanical and Hydrodynamic Analyses of Helical Strakes in the Skeletons of Glass Sponges

BY: MATHEUS C. FERNANDES, MEHDI SAADAT, PATRICK CAUCHI-DUBOIS, CHIKARA INAMURA, TED SIROTA, HOSSEIN HAJ-HARIRI, GEORGE LAUDER, KATIA BERTOLDI, JAMES C. WEAVER. SUBMITTED TO *ROYAL SOCIETY INTERFACE*, JULY 2021.

B.1 Porosity Definitions

B.1.1 Small Pores

For the calculations presented in this section, we assume the geometry description outlined in figure B.1. However, for this case, we do not have a relationship between L and S_o and thus we require obtaining these measurements from a biological specimen of the sponge. As in the previous section, the calculation here entails the following equations:

$$A_o = 2(1 + \sqrt{2})S_o^2 \quad (\text{B.1})$$

$$A_f = 4L^2 \quad (\text{B.2})$$

The effective surface porosity is given by

$$\varphi_s = \frac{\text{Area of Void}}{\text{Total Area}} = \frac{2A_o}{A_f} = \frac{4(1 + \sqrt{2})S_o^2}{4L^2} = (1 + \sqrt{2}) \left(\frac{S_o}{L} \right)^2 \quad (\text{B.3})$$

Where obtaining $S_o/L = 0.15703$, yields

$$\varphi_s = (1 + \sqrt{2}) (0.15703)^2 = 0.05953 \quad (\text{B.4})$$

In other words, this geometry provides 5.953% void and $(100\% - 5.953\%) = 94.047\%$ solid

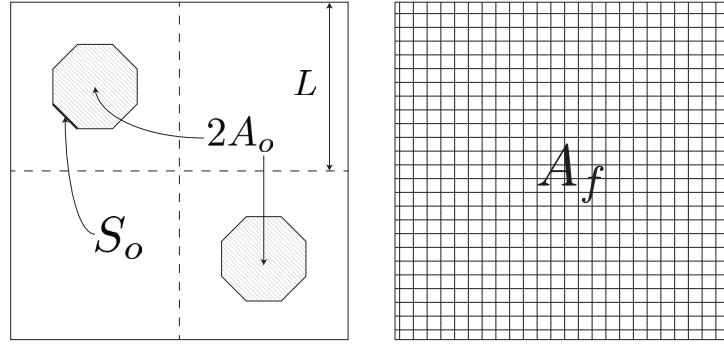


Figure B.1: Schematic of central cylinder of a living sponge (lower porosity). The figure on the left shows the calculation for the area of the voids and the figure on the right shows the total area.

B.1.2 Large Pores

For the calculations presented in this section, we assume the geometry description outlined in figure B.2. In order to compute the effective surface porosity of the sponge, we first account for the surface area of the voids, namely, $A_{void} = 2 * A_o$, where A_o is given by the are of a hexagon:

$$A_o = 2(1 + \sqrt{2})S_o^2 \quad (\text{B.5})$$

where we can obtain S_o as a function of L , namely,

$$S_o = L(\sqrt{2} - 1) \quad (\text{B.6})$$

such that A_o becomes,

$$A_o = 2(1 + \sqrt{2})L^2(\sqrt{2} - 1)^2 = L^2(2\sqrt{2} - 2) \quad (\text{B.7})$$

The are of the total area, which we call the area of the frame is denoted by A_f and is given by

$$A_f = 4L^2 \quad (\text{B.8})$$

The effective surface porosity is given by

$$\varphi_s = \frac{\text{Area of Void}}{\text{Total Area}} = \frac{2A_o}{A_f} = \frac{4\sqrt{2} - 4}{4} = 0.4142 \quad (\text{B.9})$$

In other words, this geometry provides 41.42% void and (100%-41.42 %)=58.58% solid

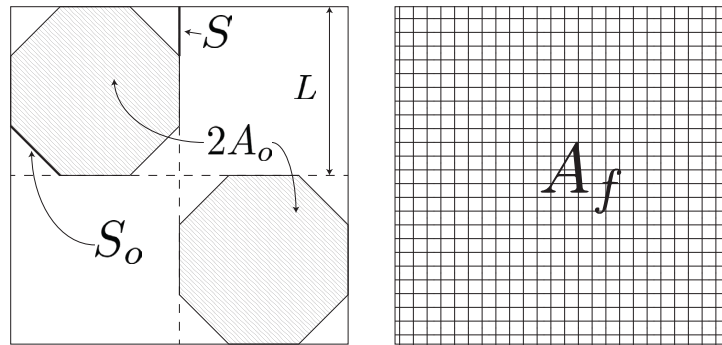


Figure B.2: Schematic of central cylinder of a deceased sponge (higher porosity). The figure on the left shows the calculation for the area of the voids and the figure on the right shows the total area.

B.2 Hydrodynamic CFD Model Details

B.2.1 Model Construction

All hydrodynamic models presented in this study were conducted using *Ansys[®] Academic Research CFX, Release 2019 R3*. The results were also post-processed using the *Academic Research CFX-Post, Release 2019 R3*. The CAD models were created as surfaces in *Rhinoceros 3D 6[®] SR13 2019-2-27* (by *Robert McNeel & Associates*) with *Grasshopper* and converted to the solid domain

used in the hydrodynamic model using *Solidworks*[®] 2018 (by *Simulia*[®]).

All cylindrical models were constructed to have an outer diameter D , outer diameter with ridges D_r , inner diameter D_i , and height H defined by:

$$D = 47 \text{ mm}; \quad D_r = 60 \text{ mm}; \quad D_i = 42.3 \text{ mm}; \quad H = 146 \text{ mm}. \quad (\text{B.10})$$

Non-porous Geometries

The considered domain for the non-porous geometries is defined as an elongated rectangular cuboid fully encapsulating the cylindrical geometry. The cuboid domain is constructed around the geometry such that its top and bottom faces match the height H of the cylindrical geometry as seen in figure B.3. The remaining four faces of the cuboid domain are aligned away from the central axis of the cylinder defined by the following length scales:

- Inlet face: $20D$
- Outlet face: $40D$
- Left face: $20D$
- Right face: $20D$

where D represents the outer diameter of the cylinder geometry. These dimensions were defined exceeding literature suggestions^[163] to minimize computational edge effects on the flow profile near the cylindrical geometry.

Porous Geometries

The considered domain for the porous geometries is defined as a less elongated and much larger cuboid than that of the non-porous case. Here, the cuboid domain is constructed to align with the

bottom of the cylindrical geometry, but allowing a large gap exists between the top of the cylindrical geometry and top face of the domain to account for flow above and through the cylindrical structure (as seen in figure B.4). Therefore, for all porous geometry cases, we account for one additional dimension to define the total height of the cuboid domain, namely:

- Top face: $20H$

where H represents the height of the porous cylinder geometry. Likewise, this additional dimension is defined exceeding recommendations in^[163] to minimize computational edge effects on the flow profile near the tip of the cylindrical geometry.

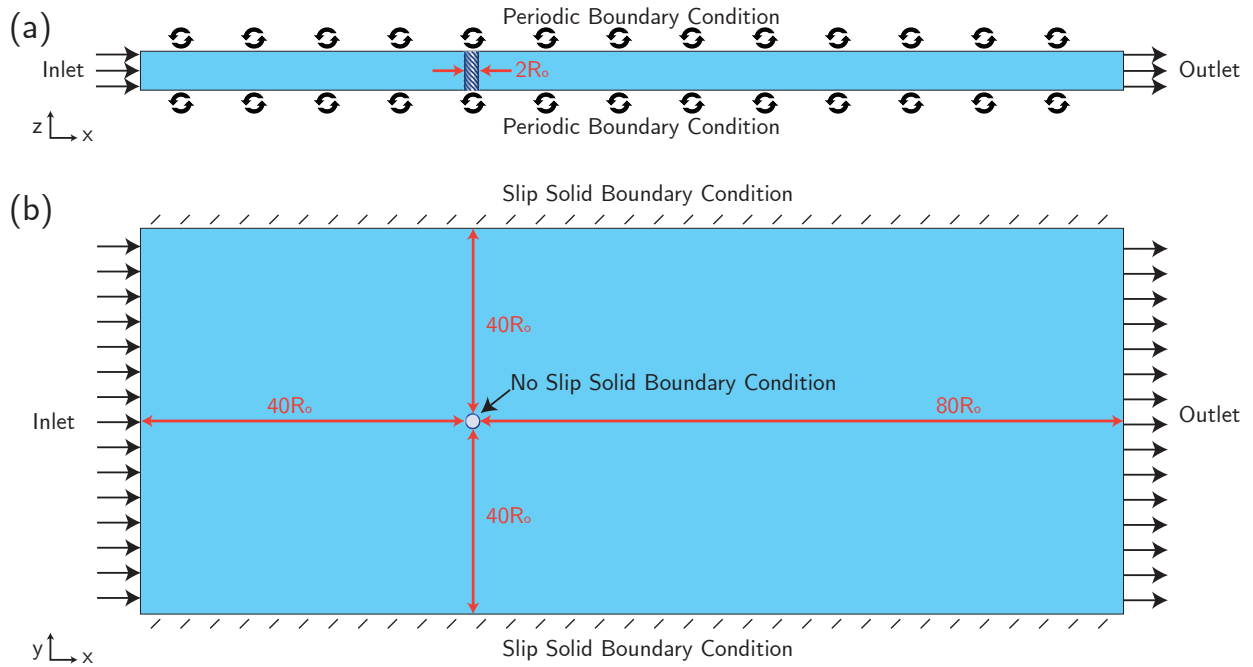


Figure B.3: CFD domain illustration for solid models simulations. Illustration showing (a) sideways and (b) top view of the considered CFD domain. This illustration shows respective boundary conditions and is drawn to scale.

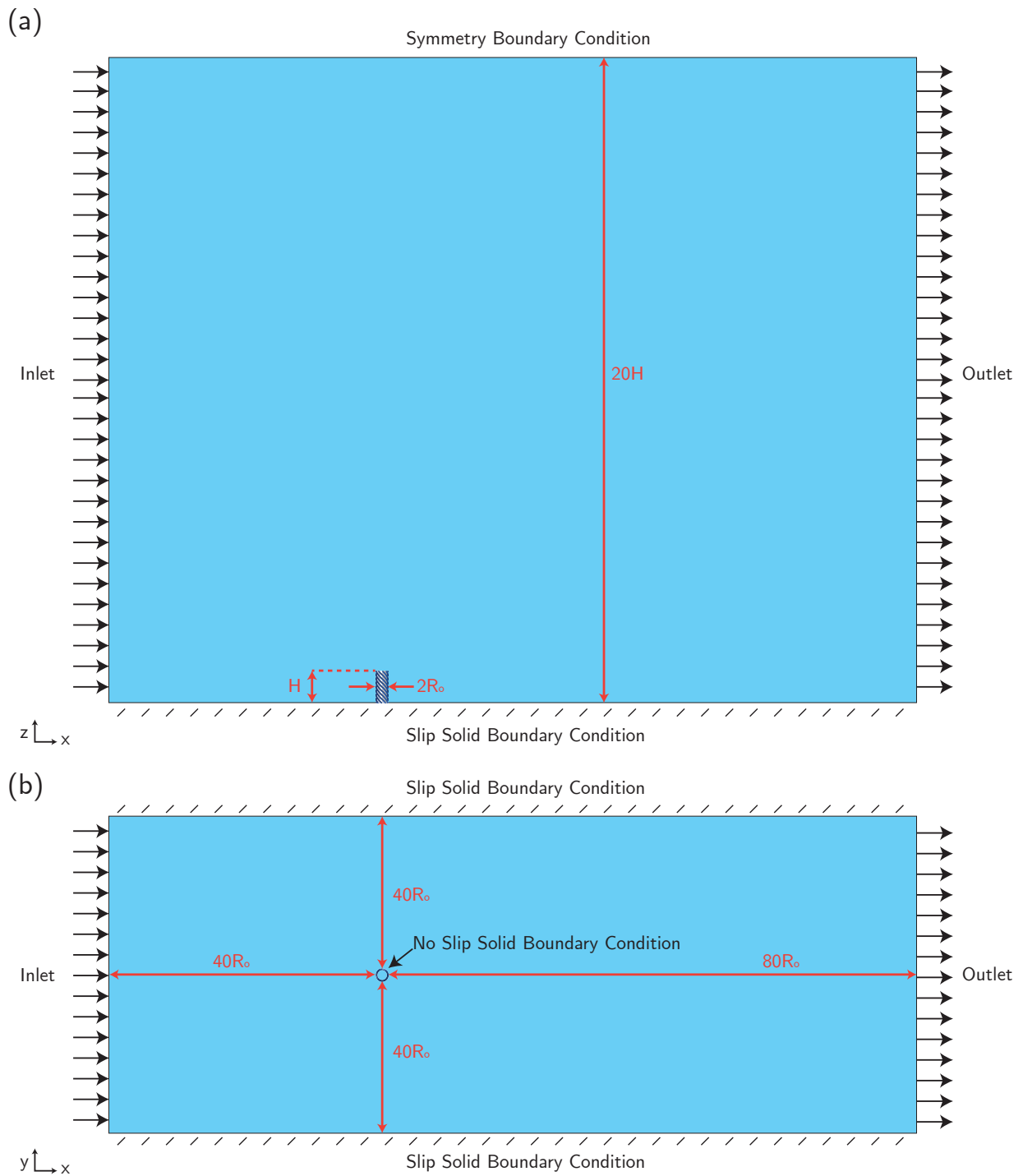


Figure B.4: CFD domain illustration for porous models simulations. Illustration showing (a) sideways and (b) top view of the considered CFD domain. This illustration shows respective boundary conditions and is drawn to scale.

B.2.2 Model Validation

The CFD model is validated for a flow past the most simple model, namely, the solid cylinder. Here, we obtain both the Strouhal number and drag coefficient and compare it to established empirical data for a flow passed a bluff cylinder^[8,9]. The comparison between empirical data and numerical results can be found in figure B.5. Figure B.5(a) and (b) show empirical data from Anderson Jr^[8], Blevins^[9], respectively. By inspection results obtained from the CFD, as shown in figure B.5 (c) and (d), closely match the empirical data for a flow passed a cylinder with a margin of error under 2%. For the drag coefficient measurements shown in figure B.5(c) it is important to note that to obtain a comparable measure we must average over the shedding oscillation to obtain a mean drag coefficient measurement.

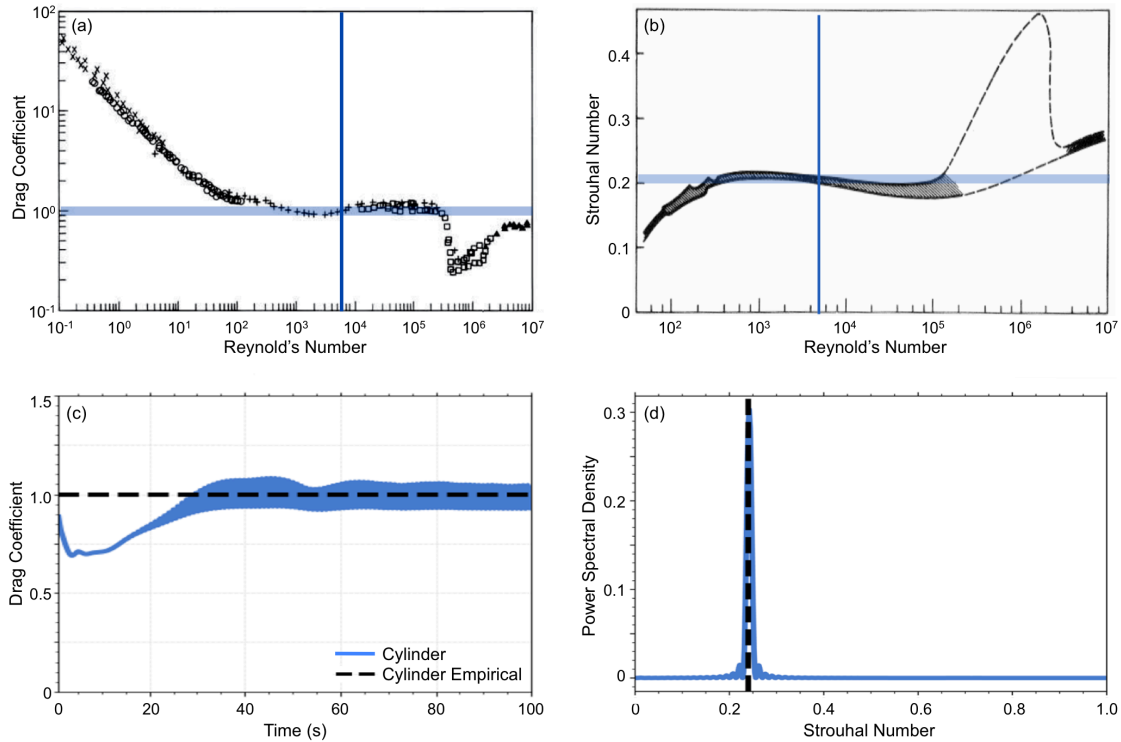


Figure B.5: Empirical data for CFD Validation. Established empirical data for flow past a bluff cylinder. (a) Shows measurements for drag coefficient as a function of Reynolds number^[8] with blue region indicating the measurements for $Re \approx 5, 500$ and (b) shows measurements for Strouhal number as a function of Reynolds number^[9] with blue region also indicating measurements for $Re \approx 5, 500$. (c) Shows the simulation results for the drag coefficient over time and (d) for the PSD spectrum as function of Strouhal number. For both (c) and (d) the simulation results are shown in blue and the empirical data comparison in black dashed lines.

B.2.3 Model Meshing

The discretization for the model was performed using *Ansys® Academic Research ICEM-CFD, Release 2019 R3*. The model mesh is defined to refine the number of elements at the region of interest, near and behind the cylinder in order to accurately capture the shear layer separation as well as the vortex shedding formation. Maximum node separation at the surface of the cylinder and ridges are defined as 5×10^{-4} [m] with a high density region around and behind the cylinder with maximum node separation 5×10^{-3} [m] with transition ratio coarsening parameter of 0.5.

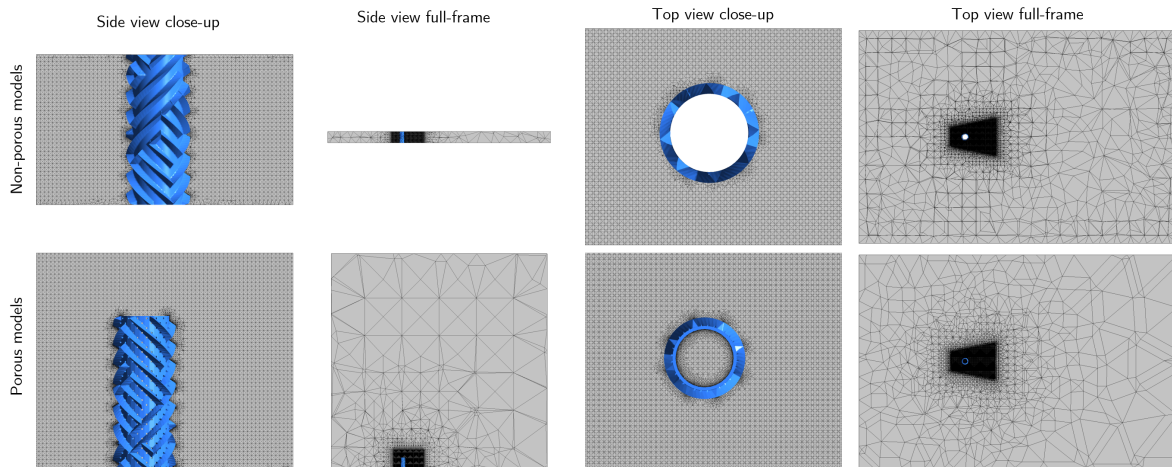


Figure B.6: CFD meshing technique. Image obtained from Ansys® showing the meshing technique employed for the CFD model. Top row shows the mesh employed for the non-porous models and bottom row shows the mesh for the porous models.

B.3 Additional Information

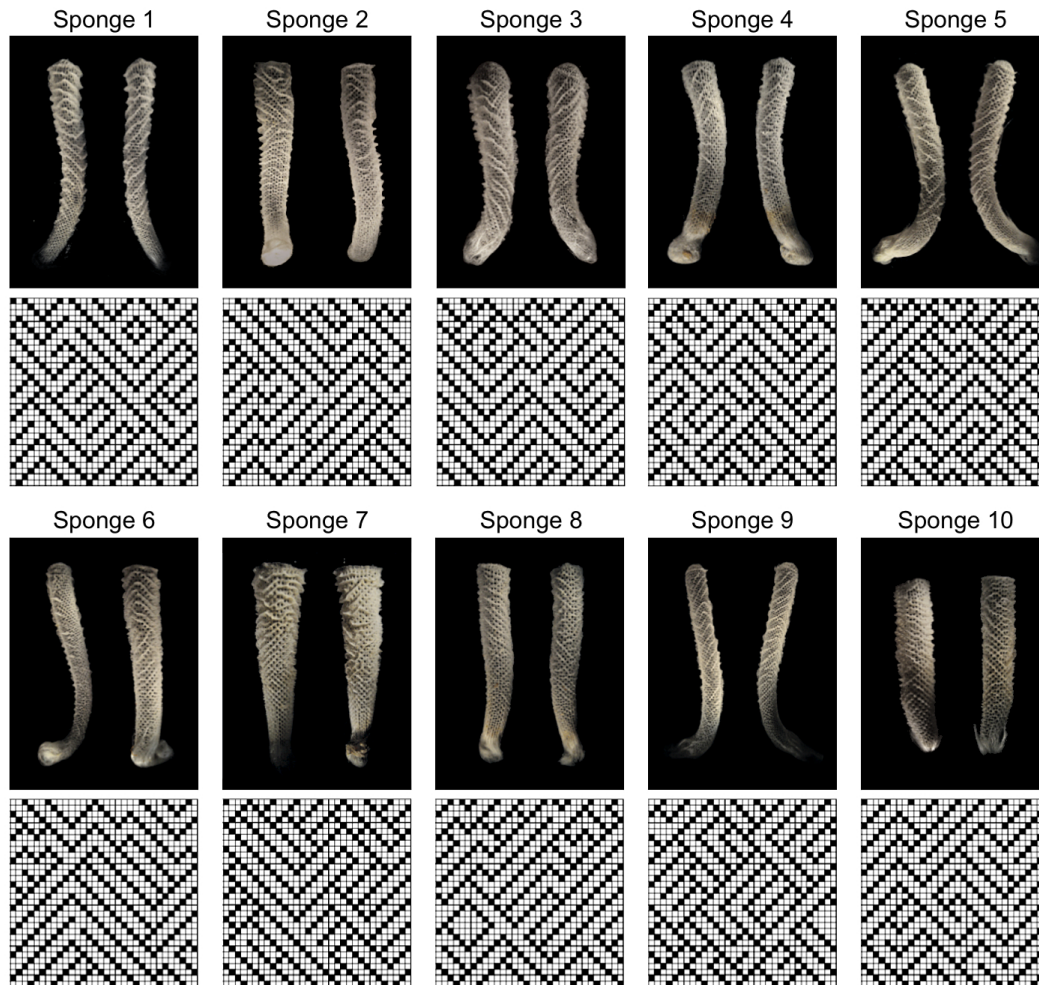


Figure B.7: Sponge Photos and Interpreted Designs. (a)-(j) shows pictures of sponge (top) and its corresponding interpreted design (bottom) . (a)-(j) correspond to Designs 1-10, respectively.

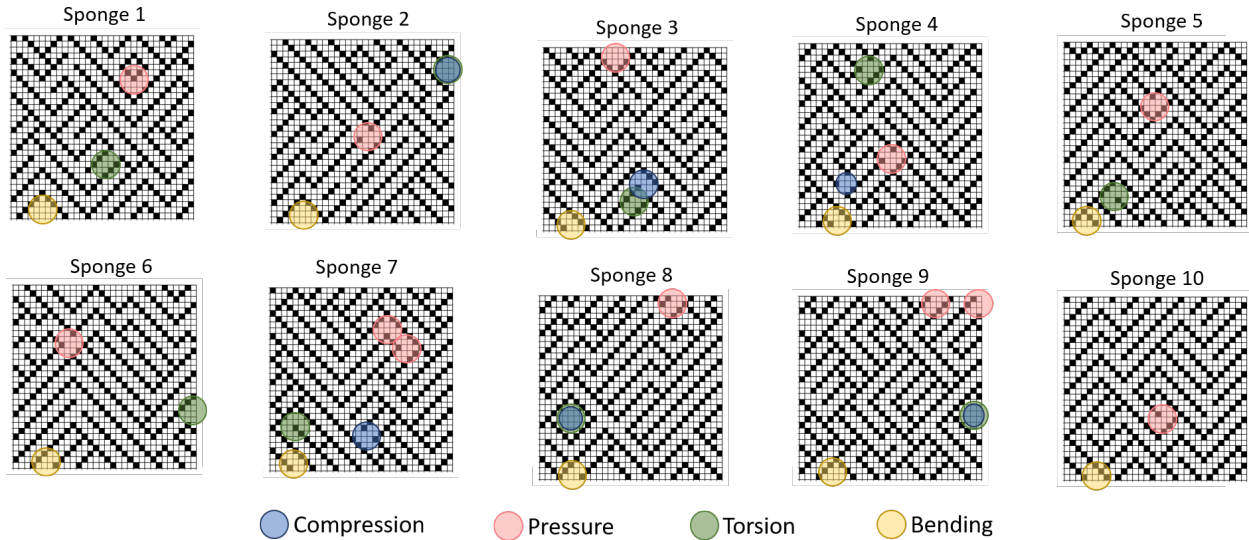


Figure B.8: Structural Buckling Locations. FE model predictions of the locations of failures for each of the considered designs for various boundary conditions. Circles denote the location of the deformation. For the bending case, one direction was chosen and shown in the diagram. If circle is missing for a particular structure it is indicative of a global deformation for that particular structure under that particular loading condition.

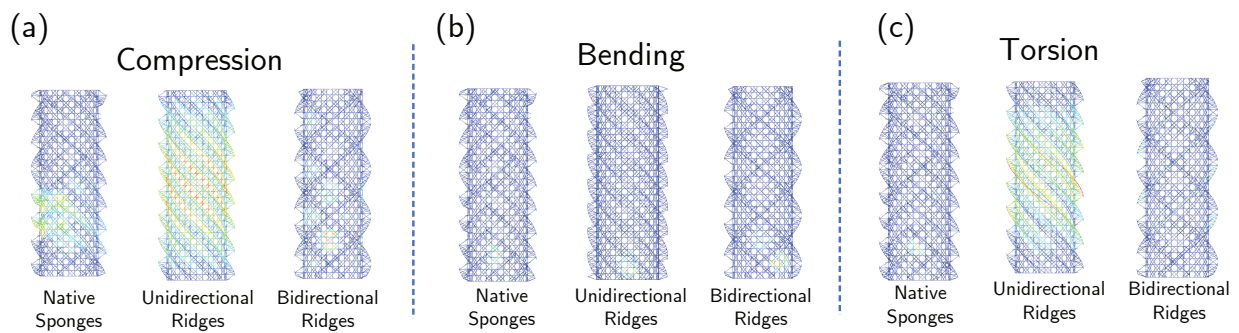


Figure B.9: Structural Buckling Deformations. This plot shows the buckling modes for the sponge, unidirectional and bidirectional ridge geometries. (a) Highlights the buckling mode for the geometries under uniaxial compression loading. Additional modes for more sponges are outlined in figure B.8. (b) Highlights the buckling modes for the geometries under cantilever bending loading. (c) Highlights the buckling modes for the geometries under torsion. These boundary conditions follow the loading described in main paper.

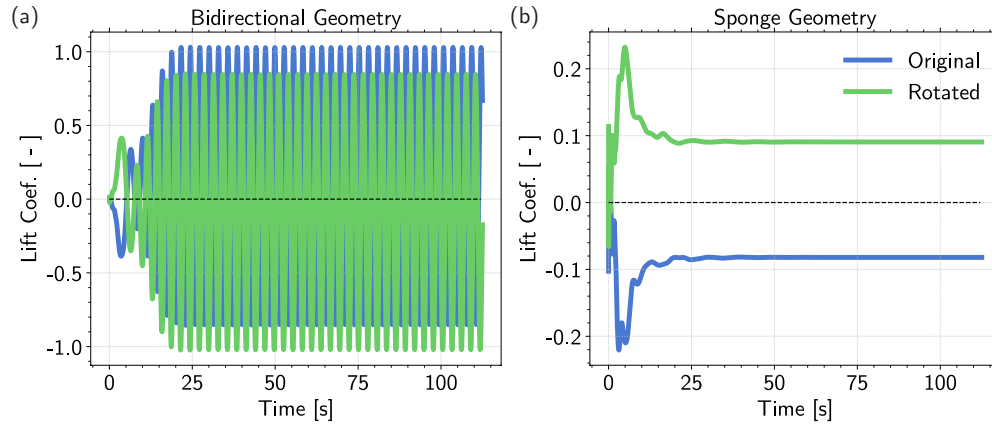


Figure B.10: Lift coefficient changes as result of rotated geometry. This figure shows the time series of the lift coefficient for geometries in their original configuration with respect to the flow (blue line) and rotated 180° with respect to the flow (green line). Results are shown for (a) *Bidirectional* and (b) *Sponge* designs. Black dashed line shows the $y = 0$ axis of symmetry. Here we see that when we rotate the geometry by 180° the average lift is approximately flipped across the $y = 0$ axis line indicating that the non-symmetric ridge configuration breaks the flow symmetry and biases the lift to a particular direction.



Supplementary Information: Surface
Texture Modulation via Buckling in
Porous Inclined Mechanical Metamaterials

BY: MATHEUS C. FERNANDES, SAURABH MHATRE, ANTONIO E. FORTE, BING ZHAO, OLGA MESA,
JAMES C. WEAVER, MARTIN BECHTHOLD, KATIA BERTOLDI. UNDER REVIEW IN *ADVANCED MATERIALS*,
SUBMITTED APRIL 2021.

C.1 Geometry

Conceptually, our metamaterial is generated from slicing a block, containing a square array of cylindrical holes, at an angle θ (figure C.1). The cylindrical holes have radius $R_h = 5.83$ mm and center-to-center distance $d_h = 13.41$ mm, such that the porosity of the structure in the undeformed configuration is $\varphi_0 = \pi R_h^2/d_h^2 = 0.59$. The resulting metamaterial has an out-of-plane thickness $T = 23.32$ mm and elliptical holes on its top and bottom faces with major and minor axis of length $R_h/\cos\theta$ and R_h , respectively.

In this study, we consider finite size samples comprising an array of 6×6 holes in the center, flanked by a column of half holes on all sides to alleviate boundary effects. These samples have size $X_f \times X_f/\cos\theta \times T$, where $X_f = 7d_h = 93.78$ mm.

Our metamaterial is activated through hydraulic or pneumatic actuation, and as such, the samples were made water/air-tight by covering their top and bottom faces with a thin elastomeric layer (with thickness of $T_{layer} \sim 0.5$ mm). A single pressure input actuation was achieved by connecting the cylindrical cavities together via a series of rectangular channels. The channels are shown in figure C.1 and have a height $H_c = 4.5$ mm, and in the final molded form, had a width of 2 mm.

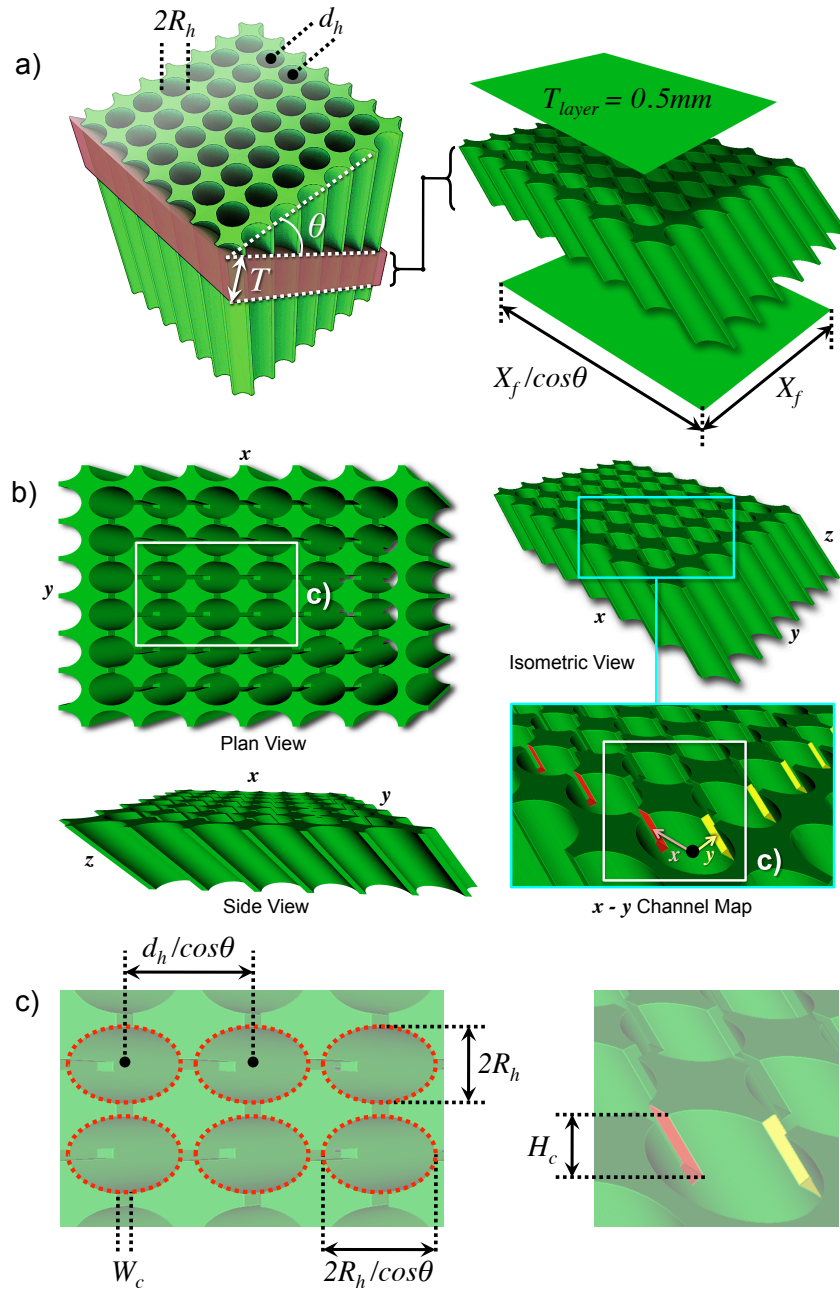


Figure C.1: Design elements of our inclined metamaterial. (a) Shows the inclined cut of our metamaterial from a square block of elastomeric matrix and its respective dimensions. On right is the exploded view of the assembly that includes the cut metamaterial and the films with its respective dimensions. (b) Shows the construction of the channel that are located along the top and bottom surfaces of the matamaterial. (c) Outlines the dimensions of the cut metamaterials in addition to the dimensions necessary to reconstruct the experimental sample.

C.2 Fabrication

To fabricate the samples, we first produced molds using a Stratasys Objet30 3D printer from VerobBlue (RGD840) material (figure C.2(a)). Before casting, releasing agent (Easy Release 200, Smooth-On, Inc.) was sprayed on the mold surfaces to further facilitate the de-molding process, and the samples were then cast using a silicone elastomer material (Zhermack Elite Double 32) (figure C.2(b)). Once the silicon elastomer was poured, the mold was quickly placed in a degassing chamber (vacuum chamber) for approximately 8 minutes. This process ensured that any remaining air was removed from the elastomer material prior to curing. Once the degassing process was completed, the cast mixture was allowed to cure at room temperature and atmospheric pressure for approximately four hours. After de-molding the planar structure (figure C.2(c)), two thin sheets were fabricated using the same silicone elastomer material by pouring the uncured rubber onto an inclined acrylic sheet (figure C.2(d)). The sheets were left to cure for 4 hours. Once cured, the thin sheets, each measuring $\approx 0.5\text{mm}$ in thickness were glued to the top and bottom surface of the metamaterial using the same silicone elastomer (figure C.2(e)). In figure C.2(f) the channels and the thin sheet are visible. The same gluing process was also used to attach the two molded halves of the metamaterial to each other (figure C.2(g and h)). As a final step, tubes were punctured into the center of the ends (the short edge) of the planar structure and sealed with the same silicone elastomer (figure C.2(i)). The final assembly was left to cure and seal for an additional 4 hours.

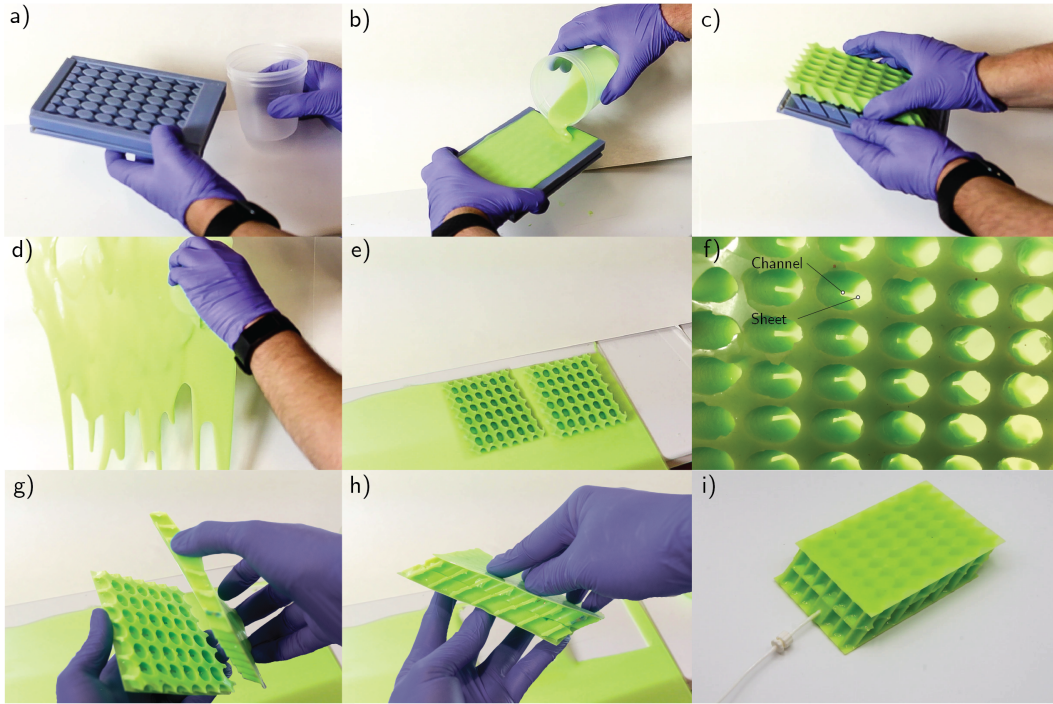


Figure C.2: Metamaterial fabrication. (a) The elastomer mixing cup and 3D-printed mold used for creating the sample. (b) Uncured elastomer is poured into the mold. (c) After allowing the elastomer to fully cure, the sample is removed from the mold. (d) Uncured elastomer is evenly poured on top of an acrylic sheet to create a thin film to be used as top and bottom sheets. (e) Two de-molded components are placed with channels face down on top of the cured thin sheet. (f) The thin sheets are glued to the samples using the same uncured silicone elastomer that was used for the other stages of the casting process. (g) The two structures are aligned, and (h) the two structures are glued together with the same elastomer. (i) A tube is punctured into the short edge and sealed with the same elastomer.

C.3 Experiments

C.3.1 Pressure-Volume Curve

To obtain the pressure-volume data, the test specimens were filled with water, while ensuring that all of the air was removed from its internal cavities. Once each specimen was filled, a volume-controlled syringe pump (Standard Infuse/Withdraw PHD Ultra Syringe Pump by Harvard Apparatus) was used to withdraw the fluid from the cavities while a pressure sensor (MPX5050DP, NXP USA Inc.) attached to the withdrawal line measured the pressure inside the sample cavities. The

withdrawal process was performed slowly, at 100 ml/min, to ensure the pressure reading obtained on the vacuum line corresponded to the pressure inside of the cavities – avoiding any viscous constrictions from the fluid flow in the tube connecting to the sample. Utilizing water allowed us to understand the pressure-volume relationship of each structure avoiding any spurious effects due to air compressibility.

For the water experiments, we measured the pressure-volume relationship of each water-filled specimen in a water tank. This allowed us to characterize the true pressure-volume relationship of the structure avoiding any spurious effects due to air compressibility. However, since our ultimate goal is to operate the metamaterial in an environment using an air controlled vacuum source, we also characterized the pressure-volume relationship of the samples using air as the driving fluid.

Because air is considered a compressible fluid, our volume readings needed to be corrected for compressibility. To do so, we used the Ideal Gas Law to build a relationship between the compressible pressure-volume curve and the compressibility-corrected pressure-volume curve. We then compare our air compressibility-corrected pressure-volume curve to that obtained using water as a the driving fluid. In particular, this correction is achieved by computing the density of air for a given pressure using:

$$\rho = (P + P_{\text{atm}})M/(RT) \quad (\text{C.1})$$

where P is the pressure gauge reading, P_{atm} is the atmospheric pressure, R is the universal gas constant, M is the molar mass of air, and T is the air temperature. Using the same information in addition to the volume of the undeformed cavities in the actuator V_{actuator} we can also compute the total mass in the system,

$$m_{\text{total}} = (V_{\text{actuator}})P_{\text{atm}}M/(RT). \quad (\text{C.2})$$

The mass in the syringe is therefore computed using the prescribed syringe volume V_{syringe}

$$m_{\text{syringe}} = \rho(V_{\text{syringe}}). \quad (\text{C.3})$$

The mass in the actuator during actuation is obtained through mass conservation as

$$m_{\text{actuator}} = m_{\text{total}} - m_{\text{syringe}}. \quad (\text{C.4})$$

Then, the mass in the actuator can be converted back to obtain the corrected volume, namely,

$$V_{\text{actuator}}^* = m_{\text{actuator}}/\rho. \quad (\text{C.5})$$

Close agreement was found when comparing the pressure-volume results utilizing water with the that of utilizing air as can be seen in figure C.3.

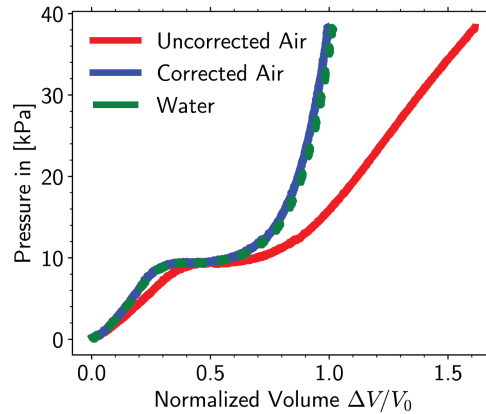


Figure C.3: Volume Correction Plot for $\theta = 45^\circ$. This figure compares the pressure volume relationship between air and water as well as with air by correcting the compressibility effects using ideal gas law.

Each specimen was actuated by extracting air from the structure through the tubes placed at the end. The tubes were attached to a volume controlled syringe pump (Standard Infuse/Withdraw

PHD Ultra Syringe Pump by Harvard Apparatus) to withdraw the fluid from the cavities

To understand the pressure-volume relationship of the structure, we placed the structure in a water tank and evacuated all air from the structure by pushing water through one tube and opening the tube on the other side. Once all air was removed, we closed one end of the specimen and utilized the syringe pump to evacuate the water at a constant rate while concurrently measuring the cavity pressure using a pressure gauge.

C.3.2 Measuring out-of-plane displacement

To measure the out-of-plane deformation of each structure, the specimen was painted white with spray chalk to minimize the reflective index of its surface, and a hand-held 3D scanner (Artec Space Spider, Artec Studio 14.1.1.75) was used to obtain the full deformation profile of the structure (figure C.4(a)-(b)). Once the scan was obtained (figure C.4(c)), a Python script was used to detect the out-of-plane deformation magnitude at the center of each structure in order to capture the deformation, while avoiding edge effects. The center of the structure was divided into four regions, with each region being sampled independently to measure the deformations around the different adjacent hole locations. In each region, we measured δ by taking the highest z -point on the face and subtracting the lowest z -point on the face, namely $\delta = \max(u_z) - \min(u_z)$.

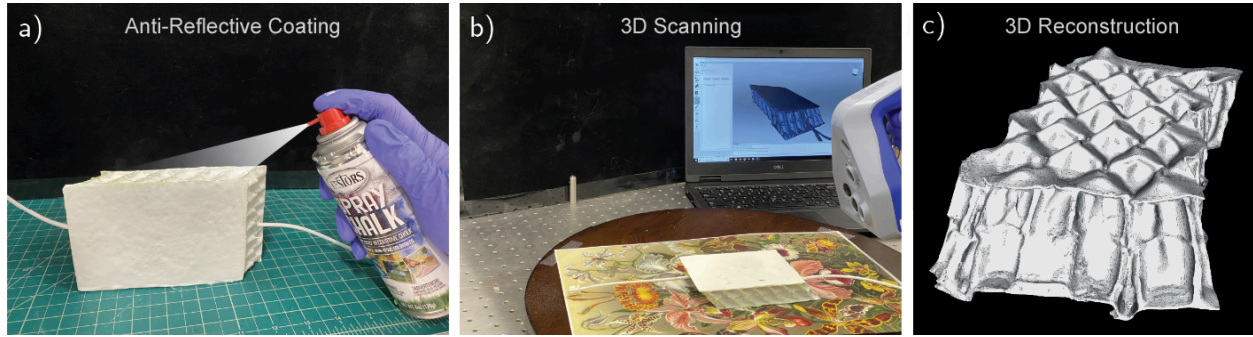


Figure C.4: Out-of-plane displacement-3D reconstructions. (a) The elastomeric sample was coated with white spray chalk to give it a non-reflective surface. (b) A 3D scanner (Artec Space Spider) was used to obtain the full deformation profile of the structure. (c) 3D computer model of the structure after post-processing.

C.3.3 Light Reflection Experiments

To understand how these structures could be employed to control light reflection, we created a simple experimental setup that captured the specular light reflection from the surface of the $\theta = 0^\circ$ and $\theta = 45^\circ$ samples onto a vertical projection screen. In this setup, we placed each of the specimens in the center of a dark room and projected a goose-neck halogen light at a 45° angle from the surface of the specimen at a distance of 9.5 cm behind the sample. A black wall, located 9.5 cm in front of the sample, contained an attached letter-sized screen onto which the specular reflection pattern from the sample was projected (as shown in fig. 3 of the main manuscript). A video camera was placed perpendicular to the screen and recorded the projected reflection pattern. As water was removed from the holes using the syringe pump, the reflection pattern was captured by the camera. The pattern information collected by the camera was then post-processed using a custom Python script. In this code, each frame was processed independently by systematically converting the color scale into gray scale. For each frame, the directional mean reflectance, R_Ω , was measured by averaging the brightness of all gray scale pixels contained on the pattern collection screen.

C.4 Numerical Simulations

C.4.1 Finite Element Simulations

The finite element analyses presented in this article were conducted using *ABAQUS/Explicit* (SIMULIA, Providence, RI). The model geometry was constructed using solid 8-node linear brick, reduced integration 3D elements (*ABAQUS* element code C3D8R) for the porous metamaterial. The top and bottom films used to seal the porous metamaterial were meshed using 4-node doubly curved thin shell elements with reduced integration (*ABAQUS* element code S4R). It is important to note that in these models, we did not incorporate the geometry of the channels as we defined a fluid filled cavity model comprising all of the holes. Actuation of the models was achieved by shrinking the volume of the fluid filled cavity. In all our simulations, the response of the elastomeric material was captured using an incompressible Neo-Hookean material model with normalized shear modulus μ .

In figure C.5 we present numerical snapshots for five different hole arrangements: (i) square array; (ii) triangular array; (iii) hexagonal array; (iv) rhombitrihexagonal array; (v) trihexagonal array. In full agreement with previous studies^[150], we found that when the holes' axes are perpendicular to the top and bottom surfaces (i.e. $\theta = 0$), buckling triggers a planar geometric transformation. For $\theta = 45^\circ$, all geometries exhibited different buckling-induced out-of-plane deformation patterns. Finally, the numerical results for the metamaterial with a square array of holes closely match the experimental data reported in Fig. 1 of the main text, confirming the validity of our simulations.

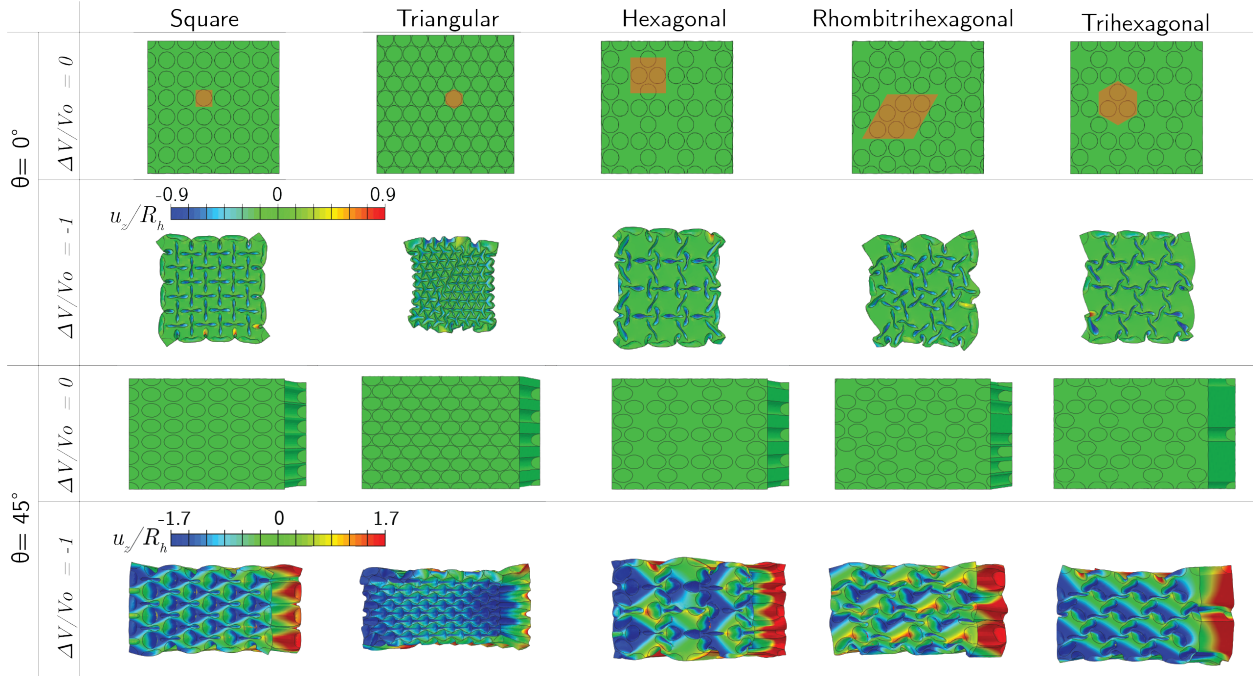


Figure C.5: Buckling-induced surface geometries for different hole patterns. Finite Element results for five hole arrangements with $\theta = 0^\circ$ (top) and $\theta = 45^\circ$ (bottom) at $\Delta V/V_0 = 0$ and $\Delta V/V_0 = -1$, for square, triangular, hexagonal, rhombitrihexagonal, and trihexagonal arrays of holes. In the images, we show the normalized out-of-plane displacement, u_z/R_h .

C.4.2 Ray Tracing Simulations

To investigate the underlying physics driving the scattering of light for the deformed 45° sample and not the deformed 0° sample, we developed a ray tracing simulation using COMSOL Multiphysics 5.0 (COMSOL Inc., Burlington, MA) Ray Tracing Module. To create the geometry for the COMSOL model, we exported the deformed/undeformed finite metamaterial geometry from ABAQUS and boolean subtracted it from an equilateral cube with edges approximately three times the length of the metamaterial length X_f . This subtracted cube, containing a void in the shape of the metamaterial, served as the underlying geometry for the light medium in the geometric optics module with a material refractive index of $n = 1$. To solve for the ray tracing, in this module, the algorithm obtains the time-dependent ray trajectory through solving the six coupled first-order

ordinary differential equations

$$\frac{d\mathbf{k}}{dt} = -\frac{\partial\omega}{\partial\mathbf{q}} \quad \text{and} \quad \frac{d\mathbf{q}}{dt} = -\frac{\partial\omega}{\partial\mathbf{k}} \quad (\text{C.6})$$

where \mathbf{k} is the wave vector, \mathbf{q} is the position vector, ω is the angular frequency, and t is time. A release grid of 9 by 9 rays was initialized on the boundary of the meshed medium and was propagated onto the surface of the deformed and undeformed samples. The surface of each sample was defined to specularly reflect from the wall (i.e. bounce condition). This conditions is dictated by

$$\mathbf{n}_r = \mathbf{n}_i - 2 \cos(\psi_i) \mathbf{n}_s \quad (\text{C.7})$$

where \mathbf{n}_r is the direction vector of the reflected ray, \mathbf{n}_i is direction of the incoming ray, ψ_i is the angle of the incoming ray, and \mathbf{n}_s is the surface normal vector. Furthermore, we defined a freeze wall condition, dictated by $k = k_c$ with k_c being the ray wave vector at the time of striking the wall, along the boundaries of optics medium cube to ensure finite time convergence. We defined a physics controlled 'extra fine' free tetrahedral mesh for the domain and utilized a time-depended solver (Generalized-alpha, backward Euler) to solve for the time evolution of the ray tip location.

C.5 Additional Results

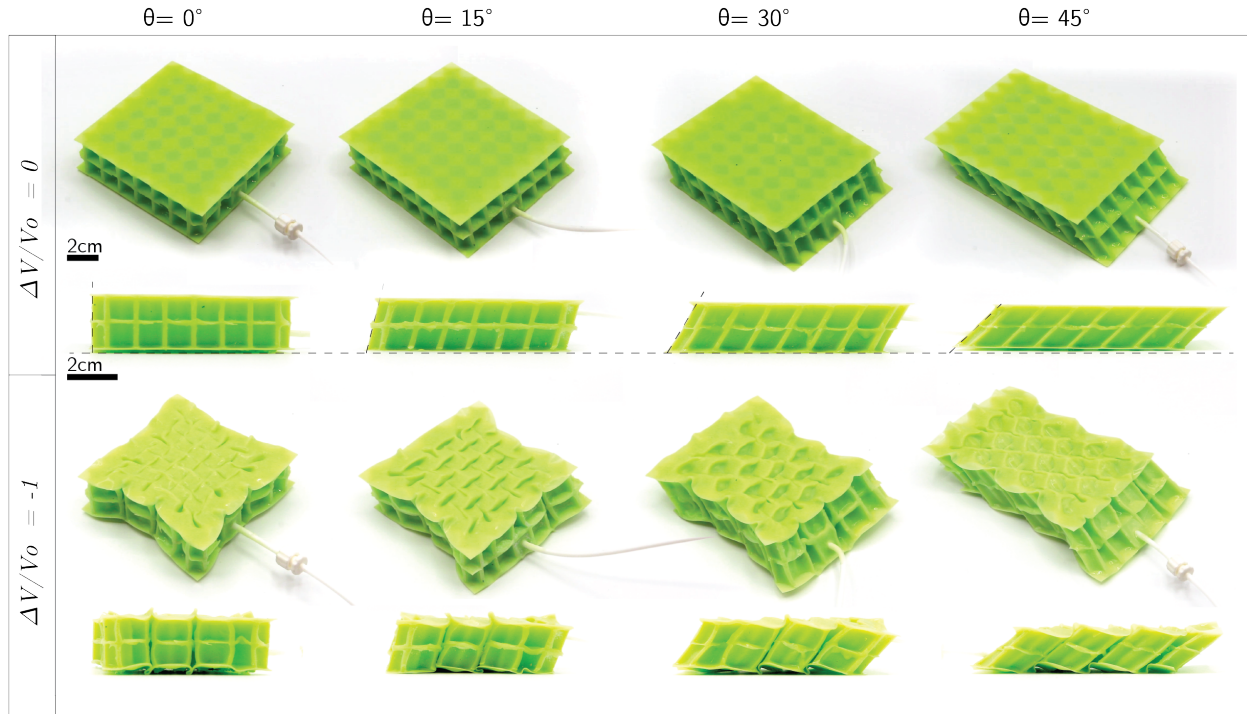


Figure C.6: Deformation for samples with $\theta = 0^\circ, 15^\circ, 30^\circ$ and 45° . Photos of the metamaterial at $\Delta V/V_0 = 0$ (top) and at $\Delta V/V_0 = -1$ configurations for samples with $\theta = 0^\circ, 15^\circ, 30^\circ$ and 45° . Both top and side views are shown.

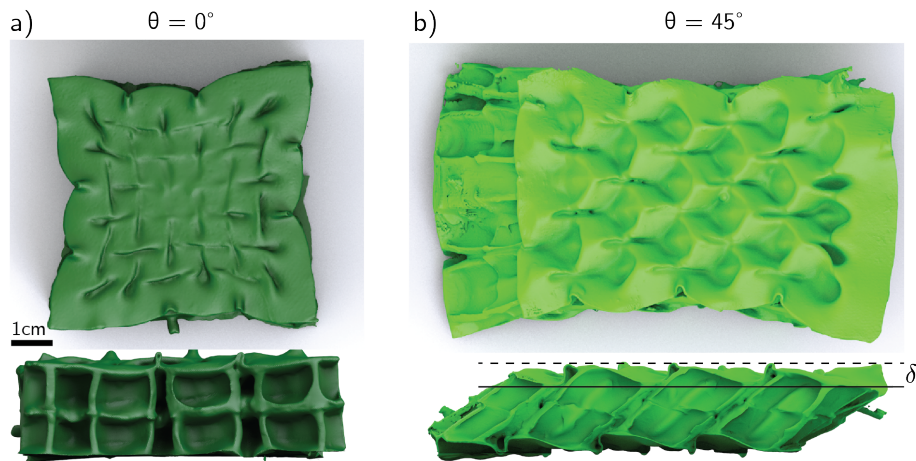


Figure C.7: 3D scans of the buckled samples. Top and side view of the scanned profile of samples with (a) $\theta = 0^\circ$ and (b) $\theta = 45^\circ$ at $\Delta V/V_0 = -1$.

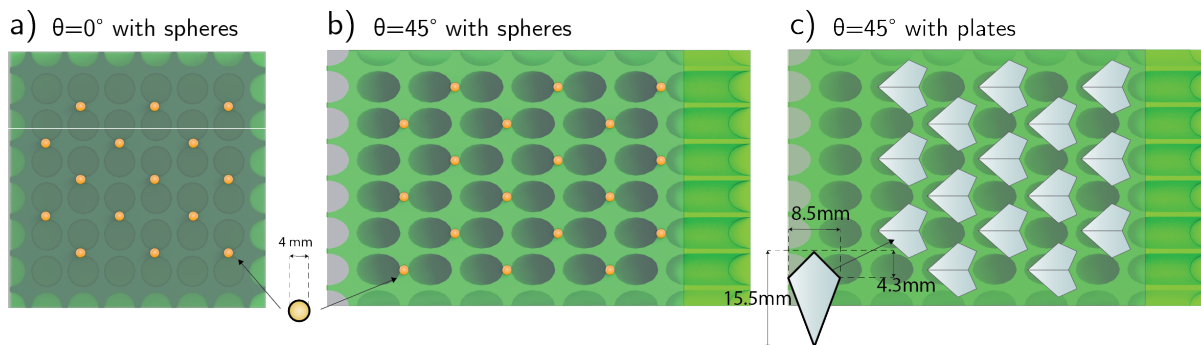


Figure C.8: Sphere and plate placement. (a) Schematics showing the placement locations of the acrylic spheres on the bottom surface of $\theta = 0^\circ$ sample. In this configuration, the sample always has the same coefficient of friction independent of $\Delta V/V_0$. (b) Schematics showing the placement locations of the acrylic spheres on the bottom surface of $\theta = 45^\circ$ sample. In this configuration, the sample has low friction at $\Delta V/V_0 = 0$ and high friction at $\Delta V/V_0 = -1$. (c) Schematics showing the placement locations of the acrylic plates on the bottom surface of $\theta = 45^\circ$ sample. In this configuration, the sample has high friction at $\Delta V/V_0 = 0$ and low friction at $\Delta V/V_0 = -1$.

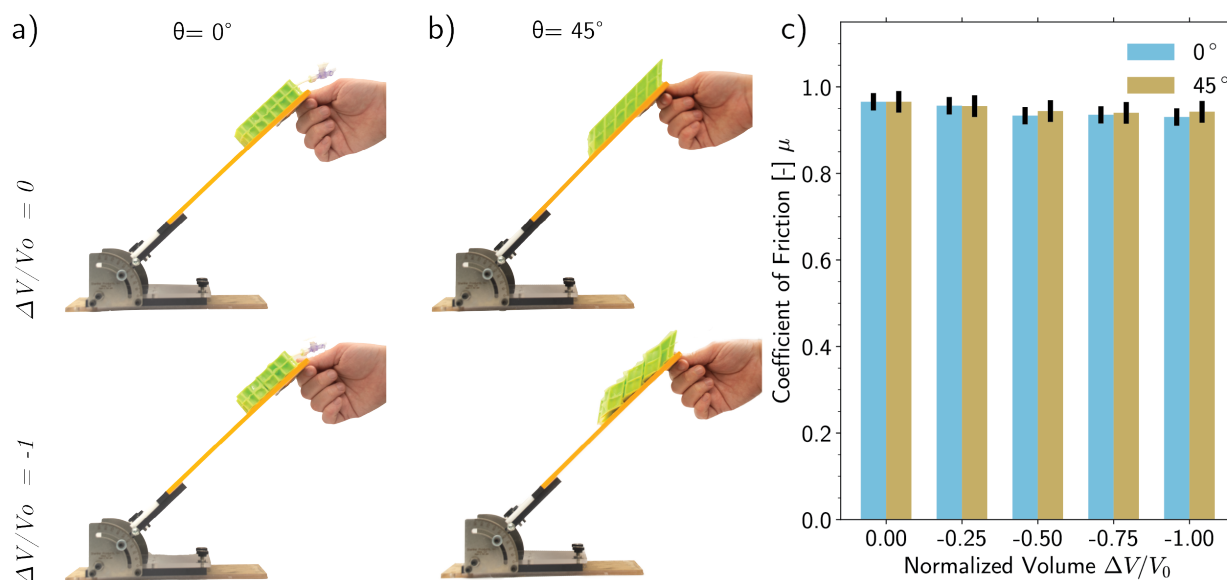


Figure C.9: Frictional properties of the metamaterial without acrylic features. (a) Photographs qualitatively showing the effect of the buckling-induced morphology on the tilting angle ϕ_{cr} for which samples with (a) $\theta = 0^\circ$ and (b) $\theta = 45^\circ$ and no acrylic feature attached to their bottom surface, began to slide. We find that for both samples, ϕ_{cr} is not affected by ΔV . (c) Coefficient of friction for the two samples as a function of $\Delta V/V_0$.

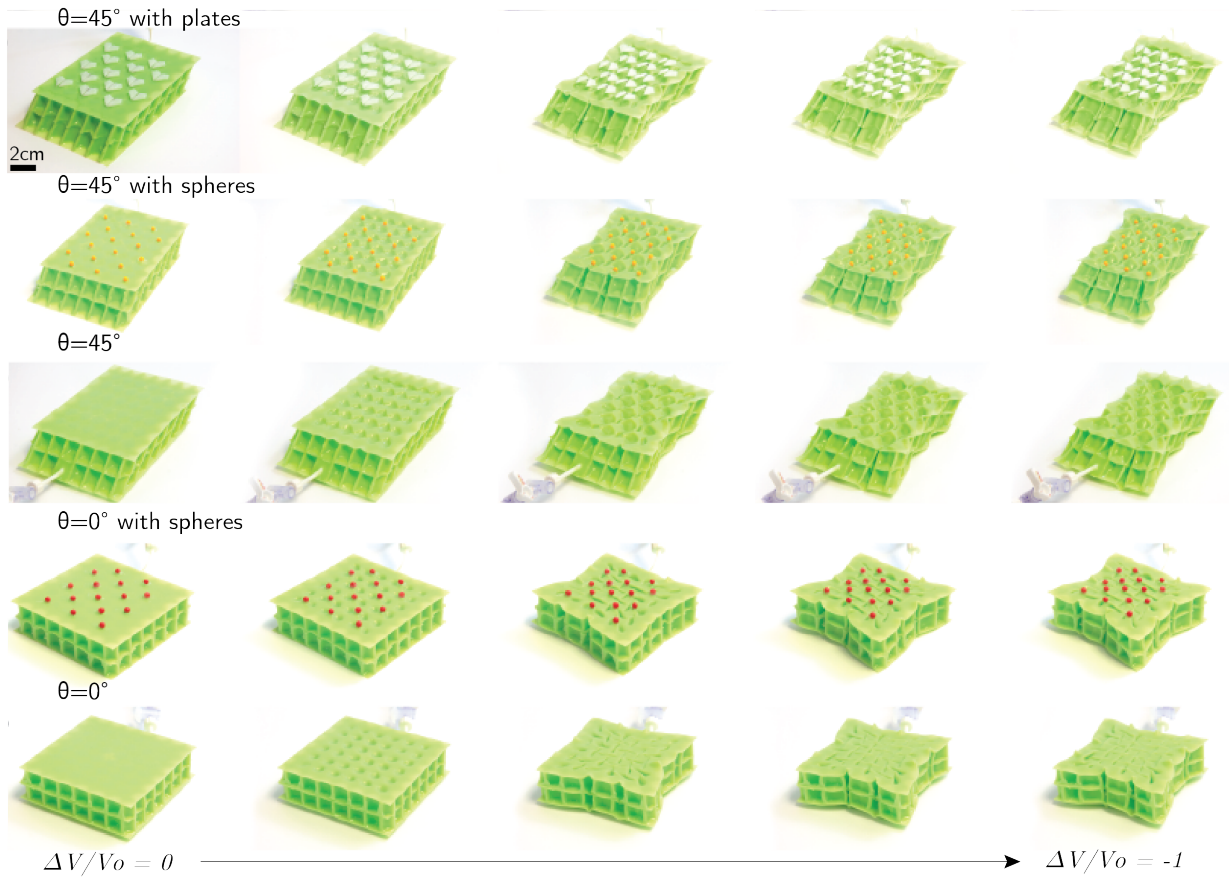


Figure C.10: Deformation for samples with acrylic features attached to their surface. Photos at decreasing values of $\Delta V/V_0$ of the metamaterials with (i) $\theta = 45^\circ$ and acrylic plates; (ii) $\theta = 45^\circ$ and acrylic spheres; (iii) $\theta = 45^\circ$ and no acrylic features; (iv) $\theta = 0^\circ$ and acrylic spheres; (v) $\theta = 0^\circ$ and no acrylic features.

References

- [1] Meyers, M. A. and Chen, P.-Y. (2014). *Biological Materials science: Biological materials, Bioinspired materials and biomaterials*. Cambridge University Press.
- [2] Sullivan, T. N., Wang, B., Espinosa, H. D., and Meyers, M. A. (2017). Extreme lightweight structures: avian feathers and bones. *Materials Today*, 20(7):377–391.
- [3] Evans, A., Hutchinson, J., Fleck, N., Ashby, M., and Wadley, H. (2001). The topological design of multifunctional cellular metals. *Progress in Materials Science*, 46(3):309 – 327.
- [4] Fratzl, P. (2005). Secrets of the Venus’ Flower Basket. *Colloids and Interfaces*.
- [5] Keable, S. (2018). Deepsea Glass Sponge. *Australian Museum Learn*.
- [6] Weaver, J. C., Aizenberg, J., Fantner, G. E., Kisailus, D., Woesz, A., Allen, P., Fields, K., Porter, M. J., Zok, F. W., Hansma, P. K., et al. (2007). Hierarchical assembly of the siliceous skeletal lattice of the hexactinellid sponge *Euplectella aspergillum*. *Journal of Structural Biology*, 158(1):93–106.
- [7] Schulze, F. (1904). *Hexactinellida, in Scientific Results of the German Deep-Sea Expedition with the Steamboat, Valdivia 1898–1899*. C. Chun (Ed.) Verlag Gustav Fischer, Jena, Germany.
- [8] Anderson Jr, J. D. (2010). *Fundamentals of aerodynamics*. Tata McGraw-Hill Education.
- [9] Blevins, R. D. (1986). *Flow-Induced Vibration*. Rebert E. Kridger Publishing Co.
- [10] Bar-Cohen, Y. (2005). *Biomimetics: biologically inspired technologies*. CRC Press.
- [11] Armstrong, W. (1979). Nature’s hitchhikers [Seeds and fruits]. *Environment Southwest*.
- [12] Wahl, L., Maas, S., Waldmann, D., Zürbes, A., and Frères, P. (2012). Shear stresses in honeycomb sandwich plates: Analytical solution, finite element method and experimental verification. *Journal of Sandwich Structures & Materials*, 14(4):449–468.
- [13] Ashby, M., Seymour, C., and Cebon, D. (1997). *Metal Foams and Honeycombs Database*.
- [14] Yang, J., Xiang, F., Guo, H., Wang, L., and Niu, X. (2020). Honeycomb-like porous carbon with N and S dual-doping as metal-free catalyst for the oxygen reduction reaction. *Carbon*, 156:514–522.

- [15] Dumont, E. R. (2010). Bone density and the lightweight skeletons of birds. *Proceedings of the Royal Society B: Biological Sciences*, 277(1691):2193–2198.
- [16] Evans, K. E. and Alderson, A. (2000). Auxetic materials: functional materials and structures from lateral thinking! *Advanced Materials*, 12(9):617–628.
- [17] Evans, A. G., Hutchinson, J., and Ashby, M. (1998). Multifunctionality of cellular metal systems. *Progress in Materials Science*, 43(3):171–221.
- [18] Aizenberg, J., Weaver, J. C., Thanawala, M. S., Sundar, V. C., Morse, D. E., and Fratzl, P. (2005). Skeleton of *Euplectella* sp.: structural hierarchy from the nanoscale to the macroscale. *Science*, 309(5732):275–278.
- [19] Aizenberg, J., Sundar, V. C., Yablon, A. D., Weaver, J. C., and Chen, G. (2004). Biological glass fibers: correlation between optical and structural properties. *Proceedings of the National Academy of Sciences*, 101(10):3358–3363.
- [20] Schulze, F. (1887). Report on the Hexactinellida collected by HMS “Challenger” during the years 1873–1876. *HMS Challenger Sci Results Zool*, 21:1–513.
- [21] Taylor, J. R. (1848). *Proceedings of the Zoological Society of London*. Longmans, Greens.
- [22] Havens, B. T., Klaiber, F. W., Lohnes, R. A., and Zachary, L. W. (1995). Longitudinal strength and stiffness of corrugated steel pipe. *Transportation Research Record*, pages 1–9.
- [23] Kang, J., Stuart, S., and Davidson, J. (2013). Analytical evaluation of maximum cover limits for thermoplastic pipes used in highway construction. *Structure and Infrastructure Engineering*, 9(7):667–674.
- [24] Yazdani, M. and Rahimi, G. (2010). The Effects of Helical Ribs’ Number and Grid Types on the Buckling of Thin-walled GFRP-stiffened Shells under Axial Loading. *Journal of Reinforced Plastics and Composites*, 29:2568–2575.
- [25] Lakes, R. (1987). Foam structures with a negative Poisson’s ratio. *Science*, 235:1038–1041.
- [26] Lakes, R. (1991). Deformation mechanisms in negative Poisson’s ratio materials: structural aspects. *Journal of Materials Science*, 26(9):2287–2292.
- [27] Milton, G. W. (1992). Composite materials with Poisson’s ratios close to -1 . *Journal of the Mechanics and Physics of Solids*, 40(5):1105–1137.
- [28] Milton, G. W. and Cherkaev, A. V. (1995). Which elasticity tensors are realizable?
- [29] Kadic, M., Bückmann, T., Stenger, N., Thiel, M., and Wegener, M. (2012). On the practicality of pentamode mechanical metamaterials. *Applied Physics Letters*, 100(19):191901.

- [30] Nicolaou, Z. G. and Motter, A. E. (2012). Mechanical metamaterials with negative compressibility transitions. *Nature Materials*, 11(7):608–613.
- [31] Bückmann, T., Thiel, M., Kadic, M., Schittny, R., and Wegener, M. (2014). An elasto-mechanical unfeelability cloak made of pentamode metamaterials. *Nature Communications*, 5(1):1–6.
- [32] Schenk, M. and Guest, S. D. (2013). Geometry of Miura-folded metamaterials. *Proceedings of the National Academy of Sciences*, 110(9):3276–3281.
- [33] Yasuda, H. and Yang, J. (2015). Reentrant origami-based metamaterials with negative Poisson's ratio and bistability. *Physical Review Letters*, 114(18):185502.
- [34] Gatt, R., Mizzi, L., Azzopardi, J. I., Azzopardi, K. M., Attard, D., Casha, A., Briffa, J., and Grima, J. N. (2015). Hierarchical auxetic mechanical metamaterials. *Scientific Reports*, 5(1):1–6.
- [35] Babaei, S., Shim, J., Weaver, J. C., Chen, E. R., Patel, N., and Bertoldi, K. (2013). 3D soft metamaterials with negative Poisson's ratio. *Advanced Materials*, 25(36):5044–5049.
- [36] Christensen, J., Kadic, M., Kraft, O., and Wegener, M. (2015). Vibrant times for mechanical metamaterials. *MRS Communications*, 5(3):453–462.
- [37] Süssstrunk, R. and Huber, S. D. (2015). Observation of phononic helical edge states in a mechanical topological insulator. *Science*, 349(6243):47–50.
- [38] Pai, P. F., Peng, H., and Jiang, S. (2014). Acoustic metamaterial beams based on multi-frequency vibration absorbers. *International Journal of Mechanical Sciences*, 79:195–205.
- [39] Bertoldi, K., Vitelli, V., Christensen, J., and Van Hecke, M. (2017). Flexible mechanical metamaterials. *Nature Reviews Materials*, 2(11):1–11.
- [40] Miura, K. (1985). Method of packaging and deployment of large membranes in space. *The Institute of Space and Astronautical Science Report*, (618):1–9.
- [41] Hawkes, E., An, B., Benbernou, N. M., Tanaka, H., Kim, S., Demaine, E. D., Rus, D., and Wood, R. J. (2010). Programmable matter by folding. *Proceedings of the National Academy of Sciences*, 107(28):12441–12445.
- [42] Tachi, T. and Miura, K. (2012). Rigid-foldable cylinders and cells. *Journal of the International Association for Shell and Spatial Structures*, 53(4):217–226.
- [43] Wei, Z. Y., Guo, Z. V., Dudte, L., Liang, H. Y., and Mahadevan, L. (2013). Geometric mechanics of periodic pleated origami. *Physical Review Letters*, 110(21):215501.

- [44] Lv, C., Krishnaraju, D., Konjevod, G., Yu, H., and Jiang, H. (2014). Origami based mechanical metamaterials. *Scientific Reports*, 4(1):1–6.
- [45] Lechenault, F., Thiria, B., and Adda-Bedia, M. (2014). Mechanical response of a creased sheet. *Physical Review Letters*, 112(24):244301.
- [46] Cheung, K. C., Tachi, T., Calisch, S., and Miura, K. (2014). Origami interleaved tube cellular materials. *Smart Materials and Structures*, 23(9):094012.
- [47] Cho, Y., Shin, J.-H., Costa, A., Kim, T. A., Kunin, V., Li, J., Lee, S. Y., Yang, S., Han, H. N., Choi, I.-S., et al. (2014). Engineering the shape and structure of materials by fractal cut. *Proceedings of the National Academy of Sciences*, 111(49):17390–17395.
- [48] Waitukaitis, S., Menaut, R., Chen, B. G.-g., and Van Hecke, M. (2015). Origami multistability: From single vertices to metasheets. *Physical Review Letters*, 114(5):055503.
- [49] Shyu, T. C., Damasceno, P. F., Dodd, P. M., Lamoureux, A., Xu, L., Shlian, M., Shtein, M., Glotzer, S. C., and Kotov, N. A. (2015). A kirigami approach to engineering elasticity in nanocomposites through patterned defects. *Nature Materials*, 14(8):785–789.
- [50] Filipov, E. T., Tachi, T., and Paulino, G. H. (2015). Origami tubes assembled into stiff, yet reconfigurable structures and metamaterials. *Proceedings of the National Academy of Sciences*, 112(40):12321–12326.
- [51] Coulais, C., Teomy, E., De Reus, K., Shokef, Y., and Van Hecke, M. (2016). Combinatorial design of textured mechanical metamaterials. *Nature*, 535(7613):529–532.
- [52] Isobe, M. and Okumura, K. (2016). Initial rigid response and softening transition of highly stretchable kirigami sheet materials. *Scientific Reports*, 6(1):1–6.
- [53] Dudte, L. H., Vouga, E., Tachi, T., and Mahadevan, L. (2016). Programming curvature using origami tessellations. *Nature Materials*, 15(5):583–588.
- [54] Haghpanah, B., Salari-Sharif, L., Pourrajab, P., Hopkins, J., and Valdevit, L. (2016). Multistable shape-reconfigurable architected materials. *Advanced Materials*, 28(36):7915–7920.
- [55] Overvelde, J. T., De Jong, T. A., Shevchenko, Y., Becerra, S. A., Whitesides, G. M., Weaver, J. C., Hoberman, C., and Bertoldi, K. (2016). A three-dimensional actuated origami-inspired transformable metamaterial with multiple degrees of freedom. *Nature Communications*, 7(1):1–8.
- [56] Overvelde, J. T., Weaver, J. C., Hoberman, C., and Bertoldi, K. (2017). Rational design of reconfigurable prismatic architected materials. *Nature*, 541(7637):347–352.

- [57] Prodan, E. and Prodan, C. (2009). Topological phonon modes and their role in dynamic instability of microtubules. *Physical Review Letters*, 103(24):248101.
- [58] Kane, C. and Lubensky, T. (2014). Topological boundary modes in isostatic lattices. *Nature Physics*, 10(1):39–45.
- [59] Chen, B. G.-g., Upadhyaya, N., and Vitelli, V. (2014). Nonlinear conduction via solitons in a topological mechanical insulator. *Proceedings of the National Academy of Sciences*, 111(36):13004–13009.
- [60] Vitelli, V., Upadhyaya, N., and Chen, B. G.-g. (2014). Topological mechanisms as classical spinor fields. *arXiv preprint arXiv:1407.2890*, 10.
- [61] Paulose, J., Meeussen, A. S., and Vitelli, V. (2015). Selective buckling via states of self-stress in topological metamaterials. *Proceedings of the National Academy of Sciences*, 112(25):7639–7644.
- [62] Nash, L. M., Kleckner, D., Read, A., Vitelli, V., Turner, A. M., and Irvine, W. T. (2015). Topological mechanics of gyroscopic metamaterials. *Proceedings of the National Academy of Sciences*, 112(47):14495–14500.
- [63] Khanikaev, A. B., Fleury, R., Mousavi, S. H., and Alu, A. (2015). Topologically robust sound propagation in an angular-momentum-biased graphene-like resonator lattice. *Nature Communications*, 6(1):1–7.
- [64] Meeussen, A. S., Paulose, J., and Vitelli, V. (2016). Geared topological metamaterials with tunable mechanical stability. *Physical Review X*, 6(4):041029.
- [65] Rocklin, D. Z., Chen, B. G.-g., Falk, M., Vitelli, V., and Lubensky, T. (2016). Mechanical Weyl modes in topological Maxwell lattices. *Physical Review Letters*, 116(13):135503.
- [66] Kariyado, T. and Hatsugai, Y. (2015). Manipulation of dirac cones in mechanical graphene. *Scientific Reports*, 5(1):1–8.
- [67] Chen, B. G.-g., Liu, B., Evans, A. A., Paulose, J., Cohen, I., Vitelli, V., and Santangelo, C. (2016). Topological mechanics of origami and kirigami. *Physical Review Letters*, 116(13):135501.
- [68] Mousavi, S. H., Khanikaev, A. B., and Wang, Z. (2015). Topologically protected elastic waves in phononic metamaterials. *Nature Communications*, 6(1):1–7.
- [69] Xiao, M., Chen, W.-J., He, W.-Y., and Chan, C. T. (2015). Synthetic gauge flux and Weyl points in acoustic systems. *Nature Physics*, 11(11):920–924.

- [70] Rocklin, D. Z., Zhou, S., Sun, K., and Mao, X. (2017). Transformable topological mechanical metamaterials. *Nature Communications*, 8(1):1–9.
- [71] Yang, Z., Gao, F., Shi, X., Lin, X., Gao, Z., Chong, Y., and Zhang, B. (2015). Topological acoustics. *Physical Review Letters*, 114(11):114301.
- [72] Süsstrunk, R. and Huber, S. D. (2016). Classification of topological phonons in linear mechanical metamaterials. *Proceedings of the National Academy of Sciences*, 113(33):E4767–E4775.
- [73] Deymier, P. A., Runge, K., Swintek, N., and Muralidharan, K. (2015). Torsional topology and fermion-like behavior of elastic waves in phononic structures. *Comptes Rendus Mécanique*, 343(12):700–711.
- [74] Bi, R. and Wang, Z. (2015). Unidirectional transport in electronic and photonic Weyl materials by Dirac mass engineering. *Physical Review B*, 92(24):241109.
- [75] Berg, N., Joel, K., Koolyk, M., and Prodan, E. (2011). Topological phonon modes in filamentary structures. *Physical Review E*, 83(2):021913.
- [76] Peano, V., Brendel, C., Schmidt, M., and Marquardt, F. (2015). Topological phases of sound and light. *Physical Review X*, 5(3):031011.
- [77] Wang, Y.-T., Luan, P.-G., and Zhang, S. (2015a). Coriolis force induced topological order for classical mechanical vibrations. *New Journal of Physics*, 17(7):073031.
- [78] Wang, P., Lu, L., and Bertoldi, K. (2015b). Topological phononic crystals with one-way elastic edge waves. *Physical Review Letters*, 115(10):104302.
- [79] Po, H. C., Bahri, Y., and Vishwanath, A. (2016). Phonon analog of topological nodal semimetals. *Physical Review B*, 93(20):205158.
- [80] Coullais, C., Sounas, D., and Alù, A. (2017). Static non-reciprocity in mechanical metamaterials. *Nature*, 542(7642):461–464.
- [81] Mullin, T., Deschanel, S., Bertoldi, K., and Boyce, M. C. (2007). Pattern transformation triggered by deformation. *Physical Review Letters*, 99(8):084301.
- [82] Bertoldi, K., Reis, P. M., Willshaw, S., and Mullin, T. (2010). Negative Poisson’s ratio behavior induced by an elastic instability. *Advanced Materials*, 22(3):361–366.
- [83] Shim, J., Perdigou, C., Chen, E. R., Bertoldi, K., and Reis, P. M. (2012). Buckling-induced encapsulation of structured elastic shells under pressure. *Proceedings of the National Academy of Sciences*, 109(16):5978–5983.

- [84] Florijn, B., Coulais, C., and van Hecke, M. (2014). Programmable mechanical metamaterials. *Physical Review Letters*, 113(17):175503.
- [85] Coulais, C., Overvelde, J. T., Lubbers, L. A., Bertoldi, K., and van Hecke, M. (2015). Discontinuous buckling of wide beams and metabeams. *Physical Review Letters*, 115(4):044301.
- [86] Fargette, A., Neukirch, S., and Antkowiak, A. (2014). Elastocapillary snapping: Capillarity induces snap-through instabilities in small elastic beams. *Physical Review Letters*, 112(13):137802.
- [87] Silverberg, J. L., Evans, A. A., McLeod, L., Hayward, R. C., Hull, T., Santangelo, C. D., and Cohen, I. (2014). Using origami design principles to fold reprogrammable mechanical metamaterials. *Science*, 345(6197):647–650.
- [88] Kang, S. H., Shan, S., Košmrlj, A., Noorduin, W. L., Shian, S., Weaver, J. C., Clarke, D. R., and Bertoldi, K. (2014). Complex ordered patterns in mechanical instability induced geometrically frustrated triangular cellular structures. *Physical Review Letters*, 112(9):098701.
- [89] Shan, S., Kang, S. H., Raney, J. R., Wang, P., Fang, L., Candido, F., Lewis, J. A., and Bertoldi, K. (2015). Multistable architected materials for trapping elastic strain energy. *Advanced Materials*, 27(29):4296–4301.
- [90] Silverberg, J. L., Na, J.-H., Evans, A. A., Liu, B., Hull, T. C., Santangelo, C. D., Lang, R. J., Hayward, R. C., and Cohen, I. (2015). Origami structures with a critical transition to bistability arising from hidden degrees of freedom. *Nature Materials*, 14(4):389–393.
- [91] Zhang, Y., Yan, Z., Nan, K., Xiao, D., Liu, Y., Luan, H., Fu, H., Wang, X., Yang, Q., Wang, J., et al. (2015). A mechanically driven form of Kirigami as a route to 3D mesostructures in micro/nanomembranes. *Proceedings of the National Academy of Sciences*, 112(38):11757–11764.
- [92] Raney, J. R., Nadkarni, N., Daraio, C., Kochmann, D. M., Lewis, J. A., and Bertoldi, K. (2016). Stable propagation of mechanical signals in soft media using stored elastic energy. *Proceedings of the National Academy of Sciences*, 113(35):9722–9727.
- [93] Rafsanjani, A., Akbarzadeh, A., and Pasini, D. (2015). Snapping mechanical metamaterials under tension. *Advanced Materials*, 27(39):5931–5935.
- [94] Seymour, G. (1928). Ithiel town. *Dictionary of American Biography, American Council of Learned Societies*, 1936.
- [95] Waddell, J. A. L. (1916). *Bridge Engineering*, volume 1. J. Wiley.

- [96] Weaver, J. C., Milliron, G. W., Allen, P., Miserez, A., Rawal, A., Garay, J., Thurner, P. J., Seto, J., Mayzel, B., Friesen, L. J., et al. (2010). Unifying design strategies in demosponge and hexactinellid skeletal systems. *The Journal of Adhesion*, 86(1):72–95.
- [97] Miserez, A., Weaver, J. C., Thurner, P. J., Aizenberg, J., Dauphin, Y., Fratzl, P., Morse, D. E., and Zok, F. W. (2008). Effects of laminate architecture on fracture resistance of sponge biosilica: lessons from nature. *Advanced Functional Materials*, 18(8):1241–1248.
- [98] Monn, M. A., Weaver, J. C., Zhang, T., Aizenberg, J., and Kesari, H. (2015). New functional insights into the internal architecture of the laminated anchor spicules of *Euplectella aspergillum*. *Proceedings of the National Academy of Sciences*, 112(16):4976–4981.
- [99] Schaedler, T. A., Jacobsen, A. J., Torrents, A., Sorensen, A. E., Lian, J., Greer, J. R., Valdevit, L., and Carter, W. B. (2011). Ultralight Metallic Microlattices. *Science*, 334(6058):962–965.
- [100] Ashby, M. (2006). The properties of foams and lattices. *Philosophical Transactions of the Royal Society of London A: Mathematical, Physical and Engineering Sciences*, 364(1838):15–30.
- [101] Phani, A. S., Woodhouse, J., and Fleck, N. (2006). Wave propagation in two-dimensional periodic lattices. *The Journal of the Acoustical Society of America*, 119(4):1995–2005.
- [102] Lu, T., Stone, H., and Ashby, M. (1998). Heat transfer in open-cell metal foams. *Acta Materialia*, 46(10):3619–3635.
- [103] Deshpande, V., Ashby, M., and Fleck, N. (2001). Foam topology: bending versus stretching dominated architectures. *Acta Materialia*, 49(6):1035–1040.
- [104] Gibson, L. J. and Ashby, M. F. (1999). *Cellular solids: structure and properties*. Cambridge university press.
- [105] Phani, A. S. and Hussein, M. I. (2017). *Dynamics of Lattice Materials*. John Wiley & Sons.
- [106] Danielsson, M., Parks, D. M., and Boyce, M. C. (2002). Three-dimensional micromechanical modeling of voided polymeric materials. *Journal of Mechanics Physics of Solids*, 50:351–379.
- [107] Bertoldi, K. and Boyce, M. C. (2008). Mechanically triggered transformations of phononic band gaps in periodic elastomeric structures. *Phys. Rev. B*, 77:052105.
- [108] Hansen, N., Akimoto, Y., and Baudis, P. (2019). CMA-ES/pycma on Github. Zenodo, DOI:10.5281/zenodo.2559634.
- [109] Horne, M. R. and Merchant, W. (1965). *The stability of frames*. Elsevier.

- [110] Saito, T., Uchida, I., and Takeda, M. (2002). Skeletal growth of the deep-sea Hexactinellid sponge *Euplectella oweni*, and host selection by the symbiotic shrimp *Spongiicola japonica* (Crustacea: Decapoda: Spongiicolidae). *Journal of Zoology*, 258(4):521–529.
- [111] Walter, S., Flinn, B., and Mayer, G. (2007). Mechanisms of toughening of a natural rigid composite. *Materials Science and Engineering: C*, 27(3):570–574.
- [112] Monn, M. A., Vijaykumar, K., Kochiyama, S., and Kesari, H. (2020). Lamellar architectures in stiff biomaterials may not always be templates for enhancing toughness in composites. *Nature Communications*, 11(1):1–12.
- [113] Woesz, A., Weaver, J. C., Kazanci, M., Dauphin, Y., Aizenberg, J., Morse, D. E., and Fratzl, P. (2006). Micromechanical properties of biological silica in skeletons of deep-sea sponges. *Journal of Materials Research*, 21(8):2068–2078.
- [114] Monn, M. A., Ferreira, J., Yang, J., and Kesari, H. (2017). A Millimeter Scale Flexural Testing System for Measuring the Mechanical Properties of Marine Sponge Spicules. *Journal of Visualized Experiments*, (128):e56571–e56571.
- [115] Fernandes, M. C., Aizenberg, J., Weaver, J. C., and Bertoldi, K. (2021). Mechanically robust lattices inspired by deep-sea glass sponges. *Nature Materials*, 20(2):237–241.
- [116] Quen, L. K., Abu, A., Kato, N., Muhamad, P., Tan, L. K., and Kang, H. S. (2018). Performance of two-and three-start helical strakes in suppressing the vortex-induced vibration of a low mass ratio flexible cylinder. *Ocean Engineering*, 166:253–261.
- [117] ER, R., Sunil, A., and Pauly, L. (2016). Analysis of flow over a circular cylinder fitted with helical strakes. *Procedia Technology*, 24:452–460.
- [118] Williamson, C. H. (1996). Vortex dynamics in the cylinder wake. *Annual Review of Fluid Mechanics*, 28(1):477–539.
- [119] Gao, Y., Yang, J., Xiong, Y., Wang, M., and Peng, G. (2016). Experimental investigation of the effects of the coverage of helical strakes on the vortex-induced vibration response of a flexible riser. *Applied Ocean Research*, 59:53–64.
- [120] Kármán, T. v. (1911). Über den Mechanismus des Widerstandes, den ein bewegter Körper in einer Flüssigkeit erfährt. *Nachrichten von der Gesellschaft der Wissenschaften zu Göttingen, Mathematisch-Physikalische Klasse*, 1911:509–517.
- [121] Kármán, T. v. (1912). Über den Mechanismus des Widerstandes, den ein bewegter Körper in einer Flüssigkeit erfährt. *Nachrichten von der Gesellschaft der Wissenschaften zu Göttingen, Mathematisch-Physikalische Klasse*, 1912:547–556.

- [122] Hooper, J. N. and Van Soest, R. W. (2002). Systema Porifera. A guide to the classification of sponges. In *Systema porifera*, pages 1–7. Springer.
- [123] ANSYS©(2020). Academic Research, Release 14.0 Help Systems. *ANSYS CFX-Solver Theory Guide*.
- [124] Stastna, M. and Lamb, K. G. (2002). Vortex shedding and sediment resuspension associated with the interaction of an internal solitary wave and the bottom boundary layer. *Geophysical Research Letters*, 29(11):7–1.
- [125] Davies, A. and Thorne, P. (2005). Modeling and measurement of sediment transport by waves in the vortex ripple regime. *Journal of Geophysical Research: Oceans*, 110(C5).
- [126] Reis, P. M. (2015). A perspective on the revival of structural (in) stability with novel opportunities for function: from buckliphobia to buckliphilia. *Journal of Applied Mechanics*, 82(11).
- [127] Kochmann, D. M. and Bertoldi, K. (2017). Exploiting microstructural instabilities in solids and structures: from metamaterials to structural transitions. *Applied Mechanics Reviews*, 69(5).
- [128] Rafsanjani, A. and Pasini, D. (2016). Bistable auxetic mechanical metamaterials inspired by ancient geometric motifs. *Extreme Mechanics Letters*, 9:291–296.
- [129] Bertoldi, K., Boyce, M. C., Deschanel, S., Prange, S., and Mullin, T. (2008). Mechanics of deformation-triggered pattern transformations and superelastic behavior in periodic elastomeric structures. *Journal of the Mechanics and Physics of Solids*, 56(8):2642–2668.
- [130] Zhang, Y., Matsumoto, E. A., Peter, A., Lin, P.-C., Kamien, R. D., and Yang, S. (2008). One-step nanoscale assembly of complex structures via harnessing of an elastic instability. *Nano Letters*, 8(4):1192–1196.
- [131] Liu, J., Gu, T., Shan, S., Kang, S. H., Weaver, J. C., and Bertoldi, K. (2016). Harnessing buckling to design architected materials that exhibit effective negative swelling. *Advanced Materials*, 28(31):6619–6624.
- [132] Wang, P., Casadei, F., Shan, S., Weaver, J. C., and Bertoldi, K. (2014). Harnessing buckling to design tunable locally resonant acoustic metamaterials. *Physical Review Letters*, 113(1):014301.
- [133] Shan, S., Kang, S. H., Wang, P., Qu, C., Shian, S., Chen, E. R., and Bertoldi, K. (2014). Harnessing multiple folding mechanisms in soft periodic structures for tunable control of elastic waves. *Advanced Functional Materials*, 24(31):4935–4942.

- [134] Krishnan, D. and Johnson, H. (2009). Optical properties of two-dimensional polymer photonic crystals after deformation-induced pattern transformations. *Journal of the Mechanics and Physics of Solids*, 57(9):1500–1513.
- [135] Li, J., Shim, J., Deng, J., Overvelde, J. T., Zhu, X., Bertoldi, K., and Yang, S. (2012). Switching periodic membranes via pattern transformation and shape memory effect. *Soft Matter*, 8(40):10322–10328.
- [136] Yang, S., Khare, K., and Lin, P.-C. (2010). Harnessing surface wrinkle patterns in soft matter. *Advanced Functional Materials*, 20(16):2550–2564.
- [137] Bowden, N., Brittain, S., Evans, A. G., Hutchinson, J. W., and Whitesides, G. M. (1998). Spontaneous formation of ordered structures in thin films of metals supported on an elastomeric polymer. *Nature*, 393(6681):146–149.
- [138] Wagner, S., Lacour, S. P., Jones, J., Pai-hui, I. H., Sturm, J. C., Li, T., and Suo, Z. (2004). Electronic skin: architecture and components. *Physica E: Low-dimensional Systems and Nanostructures*, 25(2-3):326–334.
- [139] Khang, D.-Y., Jiang, H., Huang, Y., and Rogers, J. A. (2006). A stretchable form of single-crystal silicon for high-performance electronics on rubber substrates. *Science*, 311(5758):208–212.
- [140] Harrison, C., Stafford, C. M., Zhang, W., and Karim, A. (2004). Sinusoidal phase grating created by a tunably buckled surface. *Applied Physics Letters*, 85(18):4016–4018.
- [141] Lin, P.-C., Vajpayee, S., Jagota, A., Hui, C.-Y., and Yang, S. (2008). Mechanically tunable dry adhesive from wrinkled elastomers. *Soft Matter*, 4(9):1830–1835.
- [142] Khare, K., Zhou, J., and Yang, S. (2009). Tunable open-channel microfluidics on soft poly (dimethylsiloxane)(PDMS) substrates with sinusoidal grooves. *Langmuir*, 25(21):12794–12799.
- [143] Yan, Z., Zhang, F., Wang, J., Liu, F., Guo, X., Nan, K., Lin, Q., Gao, M., Xiao, D., Shi, Y., et al. (2016). Controlled mechanical buckling for origami-inspired construction of 3D microstructures in advanced materials. *Advanced Functional Materials*, 26(16):2629–2639.
- [144] Neville, R. M., Scarpa, F., and Pirrera, A. (2016). Shape morphing Kirigami mechanical metamaterials. *Scientific Reports*, 6(1):1–12.
- [145] Ahn, C., Liang, X., and Cai, S. (2019). Bioinspired design of light-powered crawling, squeezing, and jumping untethered soft robot. *Advanced Materials Technologies*, 4(7):1900185.

- [146] Rafsanjani, A., Zhang, Y., Liu, B., Rubinstein, S. M., and Bertoldi, K. (2018). Kirigami skins make a simple soft actuator crawl. *Science Robotics*, 3(15).
- [147] Yang, Y. and You, Z. (2018). 3D Construction of a Tilted Cuboid Mechanical Metamaterial. In *ASME 2018 International Mechanical Engineering Congress and Exposition*, pages 1–8. American Society of Mechanical Engineers Digital Collection.
- [148] Chandra, D., Yang, S., and Lin, P.-C. (2007). Strain responsive concave and convex microlens arrays. *Applied Physics Letters*, 91(25):251912.
- [149] Kim, P., Hu, Y., Alvarenga, J., Kolle, M., Suo, Z., and Aizenberg, J. (2013). Rational Design of Mechano-Responsive Optical Materials by Fine Tuning the Evolution of Strain-Dependent Wrinkling Patterns. *Advanced Optical Materials*, 1(5):381–388.
- [150] Shim, J., Shan, S., Košmrlj, A., Kang, S. H., Chen, E. R., Weaver, J. C., and Bertoldi, K. (2013). Harnessing instabilities for design of soft reconfigurable auxetic/chiral materials. *Soft Matter*, 9(34):8198–8202.
- [151] Bell, A. G. (1903). The tetrahedral principle in kite structure. *National Geographic Magazine*.
- [152] Baldwin, J. (1997). *BuckyWorks: Buckminster Fuller's ideas for today*. John Wiley & Sons.
- [153] Bauer, J., Meza, L. R., Schaedler, T. A., Schwaiger, R., Zheng, X., and Valdevit, L. (2017). Nanolattices: an emerging class of mechanical metamaterials. *Advanced Materials*, 29(40):1701850.
- [154] Girault, B., Schneider, A. S., Frick, C. P., and Arzt, E. (2010). Strength effects in micropillars of a dispersion strengthened superalloy. *Advanced Engineering Materials*, 12(5):385–388.
- [155] Gao, H., Ji, B., Jäger, I. L., Arzt, E., and Fratzl, P. (2003). Materials become insensitive to flaws at nanoscale: lessons from nature. *Proceedings of the National Academy of Sciences*, 100(10):5597–5600.
- [156] Kraft, O., Gruber, P. A., Mönig, R., and Weygand, D. (2010). Plasticity in confined dimensions. *Annual Review of Materials Research*, 40:293–317.
- [157] Greer, J. R. and De Hosson, J. T. M. (2011). Plasticity in small-sized metallic systems: Intrinsic versus extrinsic size effect. *Progress in Materials Science*, 56(6):654–724.
- [158] Wang, C. and Zhang, L. (2006). Surface-layer effect in $\text{Ca Cu}_3 \text{Ti}_4 \text{O}_{12}$. *Applied Physics Letters*, 88(4):042906.

- [159] Balandin, A. A., Ghosh, S., Bao, W., Calizo, I., Teweldebrhan, D., Miao, F., and Lau, C. N. (2008). Superior thermal conductivity of single-layer graphene. *Nano Letters*, 8(3):902–907.
- [160] Josell, D., Brongersma, S. H., and Tókei, Z. (2009). Size-dependent resistivity in nanoscale interconnects. *Annual Review of Materials Research*, 39:231–254.
- [161] Dresselhaus, M. S., Chen, G., Tang, M. Y., Yang, R., Lee, H., Wang, D., Ren, Z., Fleurial, J.-P., and Gogna, P. (2007). New directions for low-dimensional thermoelectric materials. *Advanced Materials*, 19(8):1043–1053.
- [162] Hansen, N., Müller, S. D., and Koumoutsakos, P. (2003). Reducing the Time Complexity of the Derandomized Evolution Strategy with Covariance Matrix Adaptation (CMA-ES). *Evolutionary Computation*, 11(1):1–18.
- [163] Haroutunian, V. (1995). Progress in simulating industrial flows using two-equation models: Can more be achieved with further research? *NASA Technical Reports*, pages 155–155.

List of Publications/Patents

Peer Reviewed Journals

1. Pai Wang, Yue Zheng, **Matheus C. Fernandes**, Yushen Sun, Kai Xu, Sijie Sun, Sung Hoon Kang, Vincent Tournat, Katia Bertoldi (2017). Harnessing Geometric Frustration to Form Band Gaps in Acoustic Networks. *Physical Review Letters*, Volume 118, Issue 8, EID 084302. [doi:10.1103/PhysRevLett.118.084302](https://doi.org/10.1103/PhysRevLett.118.084302)
2. Sophie C. Hofferberth, Mossab Y. Saeed, Lara Tomholt, **Matheus C. Fernandes**, Christopher J. Payne, Karl Price, Gerald R. Marx, Jesse J. Esch, David W. Brown, Jonathan Brown, Peter E. Hammer, Richard W. Bianco, James C. Weaver, Elazer R. Edelman, Pedro J. del Nido (2020). A geometrically accommodating heart valve replacement. *Science Translational Medicine*, Volume 12, Issue 531, eaay4006. [doi:10.1126/scitranslmed.aay4006](https://doi.org/10.1126/scitranslmed.aay4006)
3. Lara Tomholt, Olga Geletina, Jack Alvarenga, Anna V. Shneidman, James C. Weaver, **Matheus C. Fernandes**, Santiago A. Mota, Martin Bechthold, Joanna Aizenberg (2020). Tunable infrared transmission for energy efficient pneumatic building façades. *Energy and Buildings* Volume 226, 110377. [doi:10.1016/j.enbuild.2020.110377](https://doi.org/10.1016/j.enbuild.2020.110377)
4. Lara Tomholt, Larry J. Friesen, Daniel Berdichevsky, **Matheus C. Fernandes**, Christoph Pierre, Robert J. Wood, James C. Weaver (2020). The structural origins of brittle star arm kinematics: An integrated tomographic, additive manufacturing, and parametric modeling-based approach. *Journal of Structural Biology*, Volume 211, Issue 1, 107481. [doi:10.1016/j.jsb.2020.107481](https://doi.org/10.1016/j.jsb.2020.107481)
5. **Matheus C. Fernandes**, Joanna Aizenberg, James C. Weaver, Katia Bertoldi (2020). Mechanically robust lattices inspired by deep-sea glass sponges. *Nature Materials*, Volume 20, Issue 2. [doi:10.1038/s41563-020-0798-1](https://doi.org/10.1038/s41563-020-0798-1)
6. Zian Jia, **Matheus C. Fernandes**, Zhifei Deng, Ting Yang, Qiuting Zhang, Alfie Lethbridge, Jie Yin, Jae-Hwang Lee, Lin Han, James C. Weaver, Katia Bertoldi, Joanna Aizenberg, Mathias Kolle, Pete Vukusic, Ling Li (2021). Tough color: The functional hierarchy of flower beetles' cuticle prioritizes optics over mechanics. *Proceedings of the National Academy of Sciences of the United States of America*, Volume 118, Issue 25. [doi:10.1073/pnas.2101017118](https://doi.org/10.1073/pnas.2101017118)

7. **Matheus C. Fernandes**, Saurabh Mhatre, Antonio E. Forte, Bing Zhao, Olga Mesa, James C. Weaver, Martin Bechthold, Katia Bertoldi (2021). Surface Texture Modulation via Buckling in Porous Inclined Mechanical Metamaterials. *Advanced Materials, Under Review*.
8. **Matheus C. Fernandes**, Mehdi Saadat, Patrick Cauchi-DuBois, Chikara Inamura, Ted Sirota, Hossein Haj-Hariri, George Lauder, Katia Bertoldi, James C. Weaver (2021). *Royal Society Interface, Under Review*.
9. Antonio Elia Forte, Emilia Zaria, Lishuai Jin, Paul Hanakata, Ahmad Zareei, **Matheus C. Fernandes**, Laura Sumner, Jonathan Alvarez, Christopher Payne, and Katia Bertoldi (2021). Inverse design of soft membranes through machine learning. *Proceedings of the National Academy of Sciences of the United States of America, In Preparation*.

Patents

1. Katia Bertoldi, **Matheus C. Fernandes**, James C. Weaver (2020). *Structural design principles for diagonal bracings in truss and beam support systems*. International Patents Application - PCT# WO2020113133A1 (US Priority to US201862772174P and US62/772,174), Status: Pending. [[Google Patents](#)]